

**Kinetics of Protein Phase Separation modulated by pulsed  
Electric Fields and the Role of mesoscopic Clusters in  
Crystallization and Fibrillation**

**DISSERTATION**

zur Erlangung des Doktorgrades der Naturwissenschaften (*Dr. rer. nat.*) an der Fakultät für  
Mathematik, Informatik und Naturwissenschaften der Universität Hamburg, Fachbereich  
Chemie

vorgelegt von

**Mengying Wang**

Hamburg, 2023





Die vorliegende Arbeit wurde im Zeitraum von März 2019 bis März 2023 in der Arbeitsgruppe von Prof. Dr. C. Betzel im Laboratorium für Strukturbiologie von Infektion und Entzündung am Institut für Biochemie und Molekularbiologie des Fachbereichs Chemie der Universität Hamburg durchgeführt.

Gutachter: Prof. Christian Betzel

Gutachter: Prof. Andrew Torda

Date of oral disputation: 14.04.2023



# List of publications

## Publications from this project:

- **Wang, M.**, Falke, S., Schubert, R., Lorenzen, K., Exner, C., Brognaro, H., Mudogo, C., and Betzel, C. (2020). Pulsed electric fields induce modulation of protein liquid–liquid phase separation. *Soft Matter*, 16(37), 8547-8553.
- **Wang, M.**, Barra, A. L. C., Brognaro, H., & Betzel, C. (2022). Exploring Nucleation Pathways in Distinct Physicochemical Environments Unveiling Novel Options to Modulate and Optimize Protein Crystallization. *Crystals*, 12(3), 437.
- **Wang, M.**, Thuenauer, R., Schubert, R., Gevorgyan, S., Lorenzen, K., Brognaro, H., & Betzel, C. (2023). Formation kinetics and physicochemical properties of mesoscopic Alpha-Synuclein assemblies modulated by sodium chloride and a distinct pulsed electric field. *Soft Matter*.

## Other publications:

- Zhang, T. D., Deng, X., **Wang, M. Y.**, Chen, L. L., Wang, X. T., Li, C. Y., ... & Yin, D. C. (2021). Formation of  $\beta$ -Lactoglobulin Self-Assemblies via Liquid–Liquid Phase Separation for Applications beyond the Biological Functions. *ACS Applied Materials & Interfaces*, 13(39), 46391-46405.
- Srinivasan, V., Brognaro, H., Prabhu, P. R., de Souza, E. E., Günther, S., Reinke, P. Y., Lane, T. J., Ginn, H., Han, H., Ewert, W., Sprenger, J., Koua, F. H., Falke, S., Wener, N., Andaleeb, H., Ullah, N., Franca, B., **Wang, M.**, ... & Betzel, C. (2022). Antiviral activity of natural phenolic compounds in complex at an allosteric site of SARS-CoV-2 papain-like protease. *Communications Biology*, 5(1), 805.



# Table of Contents

<i>List of publications</i> .....	<i>I</i>
<i>Table of Contents</i> .....	<i>III</i>
<i>List of Abbreviations</i> .....	<i>V</i>
<i>1 Zusammenfassung</i> .....	<i>1</i>
<i>2 Summary</i> .....	<i>5</i>
<i>3 Introduction</i> .....	<i>7</i>
3.1 Discovery and history of liquid-liquid phase separation (LLPS) .....	<i>7</i>
3.2 Role of LLPS in the process of biomacromolecule crystallization and assembly .....	<i>8</i>
3.3 Discovery and role of LLPS in intracellular biological activities.....	<i>10</i>
3.3.1 LLPS involves in the formation of membraneless organelles .....	<i>10</i>
3.3.2 LLPS in physiological function activities.....	<i>12</i>
3.3.3 Mechanism of LLPS in the process of cellular activities .....	<i>14</i>
3.4 LLPS involved in pathological activities.....	<i>15</i>
3.4.1 Diseases caused by phase separation .....	<i>15</i>
3.4.2 Diseases caused by the disruption of phase separation process.....	<i>17</i>
3.5 Biological significance and value of LLPS .....	<i>18</i>
3.5.1 Theoretical value.....	<i>18</i>
3.5.2 Application value .....	<i>19</i>
3.6 Questions remain to be addressed.....	<i>19</i>
<i>4 Aims and Outline</i> .....	<i>21</i>
<i>5 Results</i> .....	<i>23</i>
5.1 Pulsed electric fields induce modulation of protein liquid-liquid phase separation (LLPS).....	<i>24</i>
Summary .....	<i>24</i>
5.2 Exploring nucleation pathways in distinct physicochemical environments unveiling novel options to modulate and optimize protein crystallization .....	<i>33</i>
Summary .....	<i>33</i>
5.3 Formation kinetics and physicochemical properties of mesoscopic $\alpha$ -synuclein (ASN) assemblies modulated by sodium chloride and a distinct pulsed electric field.....	<i>57</i>
Summary .....	<i>57</i>
<i>6 Discussion and Conclusion</i> .....	<i>69</i>
6.1 Effect of EFs on well-folded proteins: Conformational transition, phase separation, nucleation, and crystallization .....	<i>69</i>
6.1.1 EFs influence the conformation of well-folded proteins .....	<i>69</i>

6.1.2 EFs modulate the morphologies of protein DLCs/aggregates formed via phase separation .....	69
6.1.3 Assembling and 3D-ordering kinetics of well-folded proteins can be accelerated by applying a pEF .....	70
6.1.4 Role of mesoscopic clusters in protein crystallization and the advantages of applying MOCs to optimize protein crystallization.....	70
6.2 Effect of EFs on intrinsically disordered proteins: Conformational transition, phase separation, and fibrillation .....	74
6.3 Conclusions and Prospects.....	76
<i>7 Bibliography</i> .....	<i>77</i>
<i>8 Appendix</i> .....	<i>85</i>
8.1 Amino acid sequence of full-length $\alpha$ -synuclein.....	85
8.2 Protein List.....	86
8.3 Instrumentations List .....	87
8.4 Chemical List .....	88
8.5 Supplementary Information-Pulsed electric fields induce modulation of protein liquid-liquid phase separation (LLPS).....	90
8.6 Supplementary Information-Formation kinetics and physicochemical properties of mesoscopic $\alpha$ -synuclein (ASN) assemblies modulated by sodium chloride and a distinct pulsed electric field .....	97
<i>9 Acknowledgement</i> .....	<i>109</i>
<i>10 Declaration on oath</i> .....	<i>111</i>

## List of Abbreviations

$\alpha$ : Alpha  
aa: Amino acid  
ACF: Autocorrelation function  
ASN: Alpha-synuclein  
 $\beta$ : Beta  
BPTI: Bovine pancreatic trypsin inhibitor  
CD: Circular dichroism  
cm: Centimetre  
CNT: Classical nucleation theory  
CLSM: Confocal laser scanning microscopy  
D: Dipole moment  
Da: Dalton  
 $D_t$ : Translational diffusion coefficient  
 $D_r$ : Rotational diffusion coefficient  
DLCs: Dense liquid clusters  
DLS: Dynamic light scattering  
DDLS: Depolarized dynamic light scattering  
DTT: dithiothreitol  
EDTA: Ethylenediaminetetraacetic acid  
EFs: Electric fields  
GI: Glucose isomerase  
g: Gravitational constant  
h: Hour  
Hz: Hertz  
IDP/IDPR: Intrinsically disordered protein/protein region  
IPTG: Isopropyl  $\beta$ -d-1-thiogalactopyranoside  
ITO: indium tin oxide  
 $K_D$ : Diffusion interaction parameter  
kDa: Kilodalton  
kHz: Kilohertz  
LDCs: Liquid dense clusters  
LLPS: Liquid-liquid phase separation  
M: Mole  
m: metre  
 $\mu$ : Micro  
 $\mu$ L: Microlitre  
 $\mu$ m: Micrometre  
 $\mu$ M: Micromole  
mg: Milligram

mm: Millimetre  
mM: Millimole  
mL: Millilitre  
ms: Millisecond  
mV: Millivolt  
mW: Milliwatt  
MES: 2-(N-morpholino) ethane sulfonic acid  
MOCs: Mesoscopic ordered clusters  
min: Minute  
NCNT: Non-classical nucleation theory  
nm: Nanometre  
 $\Omega$ : Omega  
PBS: Phosphate-buffered saline  
PCG: Parallel conductive glass  
PDB: Protein data bank  
Pdx: Pyridoxal 5-phosphate (vitamin B6) synthase  
pEF: Pulsed electric field  
PEG: Polyethylene glycol  
pI: Isoelectric point  
Pt: Platinum  
R: Radius  
 $R_h$ : Hydrodynamic radius  
s: Second  
TEM: Transmission electron microscopy  
TEMED: Tetramethyl ethylenediamine  
ThT: Thioflavin T  
2D: Two-dimensional  
3D: Three-dimensional  
UV: Ultraviolet  
V: Volt  
W: Watt



# 1 Zusammenfassung

In letzter Zeit hat die Protein-Flüssig-Flüssig-Phasentrennung (LLPS) grundlegende Aufmerksamkeit auf sich gezogen. Es wurde festgestellt, dass es eine entscheidende Rolle bei physiologischen Aktivitäten und der Bildung einer Reihe von intrazellulären membranlosen Organellen spielt. Andererseits wachsen auch viele feste Fibrillen oder Aggregate, die neurodegenerative Erkrankungen verursachen, durch LLPS und einen Flüssig-zu-Fest-Übergangsprozess. Früher wurden über LLPS gebildete intermediäre proteindichte Flüssigkeitscluster (DLCs) in den Materialwissenschaften im Zusammenhang mit der Erforschung des Keimbildungsmechanismus ausführlicher untersucht. Studien zu den kinetischen und physikochemischen Parametern, die LLPS dominieren, und den Eigenschaften von DLCs müssen jedoch noch durchgeführt werden, um eine theoretische Grundlage für die intervenierende intrazelluläre LLPS zu schaffen und den Engpass der Proteinkristallisation anzugehen. DLCs sind metastabile Zwischenprodukte, deren dynamische Entwicklung schwierig in Lösung im Nanomaßstab und in situ einzufangen ist, ohne den Bildungsprozess zu unterbrechen. Zur Messung der Kinetik der Proteinphasentrennung wurde eine nicht-invasive Technik der polarisierten und depolarisierten dynamischen Lichtstreuung (DLS/DDLS) eingesetzt. Das DLS/DDLS-Verfahren kann gleichzeitig die Dimensionsentwicklung und die geometrische Anordnung von Partikeln in der Suspension überwachen. Zwei klassische Phasenübergangsmodelle, Proteinkristallisation und Fibrillation, wurden angewendet, um die Wirkung physikalisch-chemischer Parameter auf die Kinetik der Proteinphasentrennung, die Eigenschaften von Protein-DLCs und die nachfolgenden Prozesse gründlich zu untersuchen.

Ein gut untersuchtes Modellprotein, Glukoseisomerase (GI, 43,23 kDa) aus *Streptomyces Rubiginosus*, wurde zunächst mittels DLS/DDLS, optischer Mikroskopie und Transmissionselektronenmikroskopie (TEM)-Methoden erforscht, um die Wirkung gepulster elektrischer Felder (pEFs) auf zu untersuchen die Pränukleationsassemblierung und 3D-Ordnung des Proteins. Der Diffusionswechselwirkungsparameter (KD) von GI bei verschiedenen Ionenstärken wurde gemessen, um zu untersuchen, wie die spezifischen und unspezifischen Protein-Protein-Wechselwirkungen LLPS und Keimbildungsprozesse beeinflussen. Darüber hinaus wurde die Rolle von mesoskopisch geordneten Clustern (MOCs) bei der Proteinkristallisation zum ersten Mal untersucht, indem durch pEFs induzierte homogene MOCs zu frischen Kristallisationströpfchen hinzugefügt wurden. Ein

rekombinanter Pyridoxal-5-phosphat (Vitamin B6)-Synthase (Pdx)-Komplex aus *Staphylococcus aureus*, zusammengesetzt aus zwölf Pdx1- und zwölf Pdx2-Proteinmonomeren, wurde verwendet, um die für GI beobachteten Phänomene zu validieren. Es wurde festgestellt, dass gepulste pEFs die Wachstumskinetik, Abmessungen und Morphologien von Protein-DLCs und Mikrokristallen signifikant beeinflussten. Die pEF-induzierten MOCs erwiesen sich als hocheffizient zur Optimierung der Kristallisationsgeschwindigkeit und -qualität. Noch wichtiger ist, dass durch DLS/DDLS mehrere Nukleationswege entdeckt wurden, bei denen die geometrische Proteinordnung nach oder gleichzeitig mit dem Proteinclusterprozess erfolgen kann, abhängig von der Ionenstärke, der Konzentration des Crowding-Mittels und den pEF-Bedingungen. Experimentelle Ergebnisse der Circular dichroismus (CD)-Spektroskopie lieferten Hinweise darauf, dass pEF Konformationsänderungen von gut gefaltetem GI auslöste, die folglich Protein-Protein-Wechselwirkungen modulieren könnten, was zur Bildung von DLCs mit unterschiedlichen Morphologien, Abmessungen und inneren Ordnungen führt.

Anschließend wurde ein intrinsisch ungeordnetes Protein (IDP) Alpha-Synuclein (ASN) untersucht, das über LLPS amyloidreiche Hydrogelcluster bilden und die Parkinson-Krankheit verursachen kann. Dieses Experiment zielte darauf ab, die Rolle von LLPS im Fibrillationsweg und die Wirkung von pEFs auf die physikalisch-chemischen Eigenschaften von intermediären DLCs zu verstehen. Die Assemblierungs- und 3D-Ordnungskinetik von ASN wurde mittels DLS/DDLS unter veränderten ionischen und EF-Bedingungen überwacht, gefolgt von der Charakterisierung der assemblierten ASN unter Anwendung von Thermostabilitätsassays, Fluoreszenz-/Autofluoreszenzassays und TEM. Der zugrunde liegende molekulare Mechanismus wurde basierend auf experimentellen Daten von KD- und CD-Messungen diskutiert. Die Ergebnisse zeigten, dass monomeres ASN in Gegenwart von 150–250 mM NaCl in einem Temperaturbereich von 20–70 °C hochgradig löslich ist und in überfüllten Umgebungen über LLPS lösliche DLCs bilden kann. Im Vergleich dazu kann die Ionenstärke von 50 mM NaCl Konformationsänderungen und attraktive Diffusionswechselwirkungen von ASN zur Bildung geordneter und thermostabiler ASN-Anordnungen auslösen. Durch die Beeinflussung der Konformation und Wechselwirkung von ASN können die angewendeten pEF- und NaCl-Gradienten die physikalisch-chemischen Eigenschaften mesoskopischer ASN-Anordnungen modifizieren, einschließlich optischer Anisotropie, Thermostabilität und Autofluoreszenz. Bemerkenswerterweise ist eine Art geordneter ASN-Anordnungen mit hoher Thermostabilität und einer Rotlicht-Autofluoreszenz bei ca. 700 nm wurde durch Auftragen

von 250 mM NaCl und pEF erzeugt, was intermolekulare ASN-Wechselwirkungen unter Bildung von  $\beta$ -Faltblattstrukturen und Wasserstoffbrückennetzwerken leitete.

Die Unterschiede zwischen der Wirkung von pEF auf das gut gefaltete Protein GI und die IDP ASN werden am Ende der Arbeit diskutiert. Zusammenfassend enthüllen die erhaltenen Daten und Ergebnisse: 1) Optionen zur Modulation der Wachstumskinetik, Morphologien und physikalisch-chemischen Eigenschaften von biomakromolekularen DLCs, Anordnungen und Kristallkeimen; 2) physikalisch-chemische Werkzeuge zur Anpassung der Nukleationswege durch Änderung der Ionenstärke, des Crowding-Agents oder der Verwendung eines externen EF; 3) eine neuartige und reproduzierbare experimentelle Strategie zur Erleichterung und Optimierung des Kristallisationsprozesses durch die Verwendung von MOCs; 4) die Wachstumskinetik und physikalisch-chemischen Eigenschaften mesoskopischer ASN-Anordnungen unter verschiedenen NaCl- und EF-Bedingungen und der entsprechende Fibrillierungsprozess.



## 2 Summary

Recently, protein liquid-liquid phase separation (LLPS) has attracted fundamental attention. As it was found to play a vital role in physiological activities and the formation of a series of intracellular membraneless organelles. On the other hand, many solid fibrils or aggregates causing neurodegenerative diseases also grow through LLPS and a liquid-to-solid transition process. Earlier, intermediate protein dense liquid clusters (DLCs) formed via LLPS were studied more extensively in material sciences in the context of exploring the nucleation mechanism. However, studies on the kinetics and physicochemical parameters dominating LLPS and the properties of DLCs remain to be carried out, to provide a theoretical basis for intervening intracellular LLPS and addressing the bottleneck of protein crystallization. DLCs are metastable intermediates, which dynamic evolution is challenging to be captured in solution at the nanoscale and *in situ* without interrupting the formation process. For measuring the kinetics of protein phase separation, a non-invasive technique of polarized and depolarized dynamic light scattering (DLS/DDLS) was employed. DLS/DDLS method can simultaneously monitor the dimensional evolution and geometrical ordering of particles in the suspension. Two classical phase transition models, protein crystallization and fibrillation, were applied to investigate thoroughly the effect of physicochemical parameters on the kinetics of protein phase separation, the properties of protein DLCs, and the subsequent processes.

A well-studied model protein, glucose isomerase (GI, 43.23 kDa) from *Streptomyces Rubiginosus*, was researched first via DLS/DDLS, optical microscopy, and transmission electron microscopy (TEM) methods to explore the effect of pulsed electric fields (pEFs) on the prenucleation assembling and 3D-ordering of the protein. The diffusion interaction parameter ( $K_D$ ) of GI under various ionic strengths was measured to study how the specific and non-specific protein-protein interactions affect LLPS and nucleation processes. Further, the role of mesoscopic ordered clusters (MOCs) in protein crystallization was investigated for the first time by adding homogeneous MOCs induced by pEFs to fresh crystallization droplets. A recombinant pyridoxal 5-phosphate (vitamin B6) synthase (Pdx) complex from *Staphylococcus aureus*, assembled from twelve Pdx1 and twelve Pdx2 protein monomers, was utilized to validate the phenomena observed for GI. It was found that pulsed pEFs significantly affected the growth kinetics, dimensions, and morphologies of protein DLCs and microcrystals. The pEF-induced MOCs were proved to be high-efficiency for optimizing the crystallization rate and quality. More importantly, multiple nucleation pathways were detected by DLS/DDLS that protein geometrical ordering can happen after or simultaneously with the protein clustering

process depending on the ionic strength, crowding agent concentration, and pEF conditions. Experimental results of circular dichroism (CD) spectroscopy provided evidence that pEF triggered conformational changes of well-folded GI, which may consequently modulate protein-protein interactions leading to the formation of DLCs with different morphologies, dimensions, and internal orders.

An intrinsically disordered protein (IDP) alpha-synuclein (ASN), which can form amyloid-rich hydrogel clusters via LLPS and cause Parkinson's disease, was investigated subsequently. This experiment aimed to understand the role of LLPS in the fibrillation pathway and the effect of pEFs on the physicochemical properties of intermediate DLCs. The assembling and 3D-ordering kinetics of ASN was monitored via DLS/DDLS under altered ionic and EF conditions, followed by the characterization of the assembled ASN applying thermostability assays, fluorescence/autofluorescence assays, and TEM. The underlying molecular mechanism was discussed based on experimental data of  $K_D$  and CD measurements. Results showed that in the presence of 150-250 mM NaCl, monomeric ASN is highly soluble in a temperature range of 20-70 °C and can form dissoluble DLCs via LLPS in crowded environments. In comparison, the ionic strength of 50 mM NaCl can trigger conformational changes and attractive diffusion interactions of ASN towards the formation of ordered and thermostable ASN assemblies. Thus, by influencing the conformation and interaction of ASN the applied pEF and NaCl gradients can modify the physicochemical properties of mesoscopic ASN assemblies, including optical anisotropy, thermostability, and autofluorescence. Remarkably, a species of ordered ASN assemblies with a high thermostability and a red-light autofluorescence at approx. 700 nm was produced by applying 250 mM NaCl and the pEF, which guided ASN intermolecular interactions forming  $\beta$ -sheet structures and hydrogen-bond networks.

The differences between the effect of pEF on the well-folded protein GI and the IDP ASN are discussed at the end of the work. In summary, data and results obtained unveil: 1) options to modulate the growth kinetics, morphologies, and physicochemical properties of bio-macromolecular DLCs, assemblies, and the crystal nuclei; 2) physicochemical tools to adjust nucleation pathways by changing ionic strength, crowding agent, or utilizing an external EF; 3) a novel and reproducible experimental strategy to facilitate and optimize the crystallization process by using MOCs; 4) the growth kinetics and physicochemical properties of mesoscopic ASN assemblies under different NaCl and EF conditions and the corresponding fibrillation process.

## 3 Introduction

### 3.1 Discovery and history of liquid-liquid phase separation (LLPS)

Lately, investigations about liquid-liquid phase separation (LLPS) have entered the "explosive growth" stage. These studies reported that LLPS performs a series of essential functions in biological systems and can be associated with many human diseases, especially neurodegenerative diseases.<sup>1,2,3,4,5,6,7,8</sup> Before these discoveries, LLPS received more attention as a natural phenomenon in the field of physical sciences, involving inorganic and organic materials such as water<sup>9</sup>, silica<sup>10</sup>, metal alloy<sup>11</sup>, and biological macromolecules<sup>12-15</sup>.

Phase transitions generally describe the transition between solid, liquid, and gaseous states of a substance and, in rare cases, plasma. The earliest research on phase transition can be dated back to the description of temperature, pressure, and volume of alcohol transition process between its liquid and gas states by Charles Caignardde la Tour in 1822.<sup>16</sup> In 1869, Thomas Andrews reported that a large number of liquid and gas phases can continuously convert into each other at the critical point of the phase transition.<sup>17</sup> After that, Josiah Willard Gibbs introduced Phase Diagram-Thermodynamic Variogram (such as temperature and pressure) in 1873, which is widely used in phase transition system.<sup>18,19</sup> LLPS is an equilibrium process in which the homogeneous solution spontaneously separates into two or more distinct phases suspended in the bulk solution. The solutes can be flexible polymers as well as biomacromolecules with a stable tertiary structure.<sup>20</sup> LLPS is widely observed in the material world and natural sciences, from small molecules to macromolecules, inorganics to organics and metals to non-metals. Nonetheless, all of them follow the same pathways to undergo LLPS, which proceeds the formation of aggregation, gelation, and nucleation. Thus, LLPS is widely applied and observed in fields such as protein crystallography, protein separation, production of drugs and other materials.<sup>10,11,29,30,21-28</sup>

The earliest discovery of the LLPS phenomenon in biological sciences was in the lens of cataract mammals in 1977.<sup>31</sup> However, people rarely knew at that time that it was just the tip of the iceberg of biological activities in which LLPS participated. In fact, there are a number of membraneless organelles in cells, but it is still a mystery to explain how they formed. Until 2009, Brangwynne et al. published a paper in *Science* revealing the liquid-like droplet properties of P granule in *C. elegan's* embryonic cells, including fusion, dripping and wetting ability, round and permeable surface, as well as dynamic internal composition. They then proposed that the P granule is assembled via LLPS to participate in the asymmetric separation

of the reproductive system.<sup>32</sup> This discovery inspired the study of the assembling mechanism of membraneless organelles. Since then, more membraneless organelles (such as nucleoli, centrosomes, stress granules, etc.) in cells were demonstrated to be highly dynamic liquid-like droplet structures and assembled through LLPS. At the same time, LLPS is widely found in physiological processes of living organisms (such as transcriptional gene regulation, natural immune response, stress response, protein classification, biochemical reaction control, etc.)<sup>3,5,7,8,33–38</sup> and pathological processes (such as neurodegenerative diseases, cancer, cataracts, etc.)<sup>39–43</sup>. Studies on LLPS also shed light on understanding the functioning mechanism of intrinsically disordered proteins (IDPs) and nucleic acids without stable structures *in vivo*, which can hardly be explained by the traditional theories of structural biology. As a result, a series of LLPS-related studies were initiated in biological sciences, which can be classified into two categories:

1) From the viewpoint of biophysical sciences, mainly at the macromolecular level, to study the role of LLPS in the processes of crystallization and self-assembly of macromolecules.

2) From the viewpoint of biochemistry and cell biology sciences, mostly at the scale of cellular and organism levels, to identify LLPS-relevant macromolecules involved in normal and abnormal physiological processes.

### **3.2 Role of LLPS in the process of biomacromolecule crystallization and assembly**

Crystallization is the primary way for biophysicists to analyse tertiary protein structures and understand the relationship between protein structures and functions. Despite the development of electron microscopy techniques, nearly 86% of the protein structures deposited in the protein data bank were obtained by single crystal X-ray diffraction till the end of 2022, demonstrating that protein crystallization is still essential in structural biology. Moreover, protein crystallization was also used as a method in obtaining high-purity and high-activity proteins,<sup>44</sup> which is very useful for the industrial production of biochemical reagents and protein materials. The slower dissolution rate of protein crystals can help achieve controlled drug release.<sup>26,30</sup> Therefore, protein crystallization can be applied to prepare sustained-release drugs.

However, crystal nucleation is a significant obstacle step during the crystallization process. Controlling and promoting the nucleation step is crucial for increasing the crystallization rate and optimizing the crystals' number, dimension, and morphology.<sup>14</sup> Therefore, the thermodynamic and molecular mechanisms of crystal nucleation have always been the focus



of crystallography. At present, the classical and non-classical nucleation theories are used to explain the mechanism study of crystal nucleation.

The classical nucleation theory postulates that the formation of crystals is a first-order phase transition, in which the first step of forming a new phase is called nucleation.<sup>45,46</sup> In this process, the total free energy of the system consists of volume-free energy and interface-free energy. Among them, the former is energy favourable, while the latter is unfavourable. The competition between them forms an energy barrier for nucleation.<sup>47</sup> When the thermodynamic fluctuation causes structural and density fluctuations in the solution, small particles having similar order and density with crystals form and dissolve constantly until they are larger than a specific size (critical size) to overcome the free energy barrier. Therefore, these stable and ordered small particles are called critical nuclei and will continue to grow up to crystals (See Fig. 3-1).<sup>48</sup> The classical nucleation theory is valuable and has played a crucial role in explaining nucleation for a long time. However, it showed limitations in explaining several crystallization kinetic curve characteristics. For example,

- 1) In the crystallization experiment of lysozyme protein, the nucleation rate is about ten orders of magnitude lower than the rate predicted by the classical theory.<sup>49</sup>
- 2) The dependence of nucleation rate on temperature is more complicated than that proposed by classical nucleation theory.<sup>49</sup>
- 3) And it cannot explain the role of metastable dense phases that appeared in the nucleation process.<sup>49</sup>

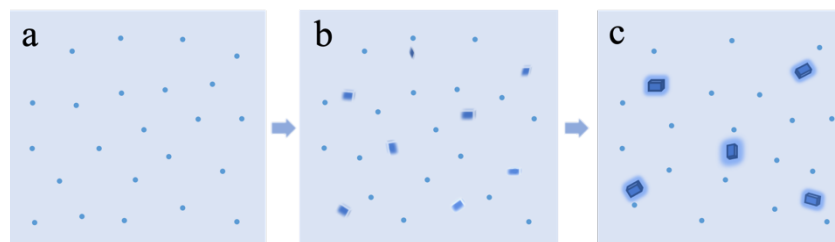


**Figure 3-1.** Schematic diagram of the classical one-step nucleation theory. a) Homogeneous protein solution, b) prenucleus clusters, c) partial prenucleus clusters overcome energy barriers and continue growing into crystal nuclei.

To complement the limits of the classic nucleation theory, Wolde and Frenkel proposed a two-step nucleation theory in 1997 via numerical simulation and thermodynamic model prediction.<sup>50</sup> According to the two-step mechanism, the homogeneous solution undergoes LLPS firstly to form metastable dense liquid clusters (DLCs), having dimensions of approx. several hundred nanometres, which are separated from and suspended in the bulk solution. The

second step is the formation of ordered nuclei within DLCs, as shown in Figure 3-2. Thus, DLCs are considered as precursors of crystal nuclei.<sup>51</sup> This mechanism was later validated by the thermodynamic data of nucleation obtained from a large number of protein crystallization experiments. Alber et al. observed directly the occurrence of LLPS during crystal nucleation and the growth of the nuclei.<sup>52–54</sup> Afterwards, an increased number of experiments proved that the two-step theory is also applicable to small molecule systems, including organic material,<sup>55</sup> colloid,<sup>56</sup> polymers,<sup>57</sup> and biomineral.<sup>58</sup>

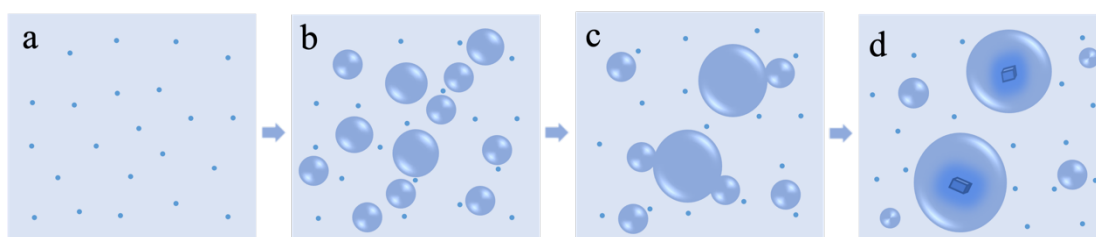


**Figure 3-2.** Schematic diagram of the two-step nucleation theory. a) Homogeneous protein solution, b) LLPS, c) fusion of DLCs, d) formation of crystal nucleus within DLCs.

Based on the development of the two-step nucleation theory, it is thus known that LLPS is widely present in the assembly and crystallization process of inorganic molecules and biomacromolecules. The discovery of LLPS participating in crystal nucleation has profoundly extended the nucleation theory and provided new insights for solving the bottleneck problems in structural biology and material sciences.

### 3.3 Discovery and role of LLPS in intracellular biological activities

It was only recent decades, LLPS was discovered to participate in intracellular physiological and pathological activities, although it has been studied for a long time in structural biology. Compared to the extracellular system, the substances involved in LLPS are more complex and dynamic in crowded intracellular environments.

#### 3.3.1 LLPS involves in the formation of membraneless organelles

The formation of membraneless organelles is a primary phase separation phenomenon observed in cells. Intracellular chaotic liquid substances are transformed through LLPS into various functional cell compartments, including nuclear bodies (nucleoli, nuclear pore, Cajal bodies, histone locus bodies (HLB), Promyelocytic leukaemia (PML) bodies, heterochromatin, paraspeckles, and speckles)<sup>59–65</sup> and membraneless organelles in the cytoplasm (P granules, germ granules, P bodies, stress granules, centrosome, etc.)<sup>66–69</sup>. Nuclear bodies are generally

rich in RNA and proteins vital for gene regulation.<sup>70</sup> The largest and most well-known nuclear body is the nucleolus, which was first described in 1835 and functions in ribosomal biogenesis and is key for cell growth and homeostasis.<sup>71</sup>

In 1983, Wolf and Strome & Wood et al. published the first membraneless organelle P granules, which participate in the asymmetric division of the germ line of *C. elegans* embryo cells.<sup>72</sup> However, the mystery of how this kind of membraneless organelles form was not elucidated until 2009, Brangwynne et al. revealed that a P granule is a liquid-like droplet.<sup>32</sup> P granule proteins combine with each other by low-affinity interactions and separate from the large number of cytoplasmic solutes, undergoing a classical phase transition process.<sup>73,74,32</sup> This discovery inspired the explanation of the formation mechanism of other membraneless organelles with highly dynamic liquid-like properties. Membraneless organelles formed by LLPS have a common feature, consisting of intrinsically disordered protein regions (IDPRs) or IDPs, which lack a stable folded structure. The compositions of membraneless organelles are similar to that of the surrounding solutes but more dense, and can exchange with the surrounding solutes to adapt to environmental stimulation rapidly.<sup>75,76,77</sup>

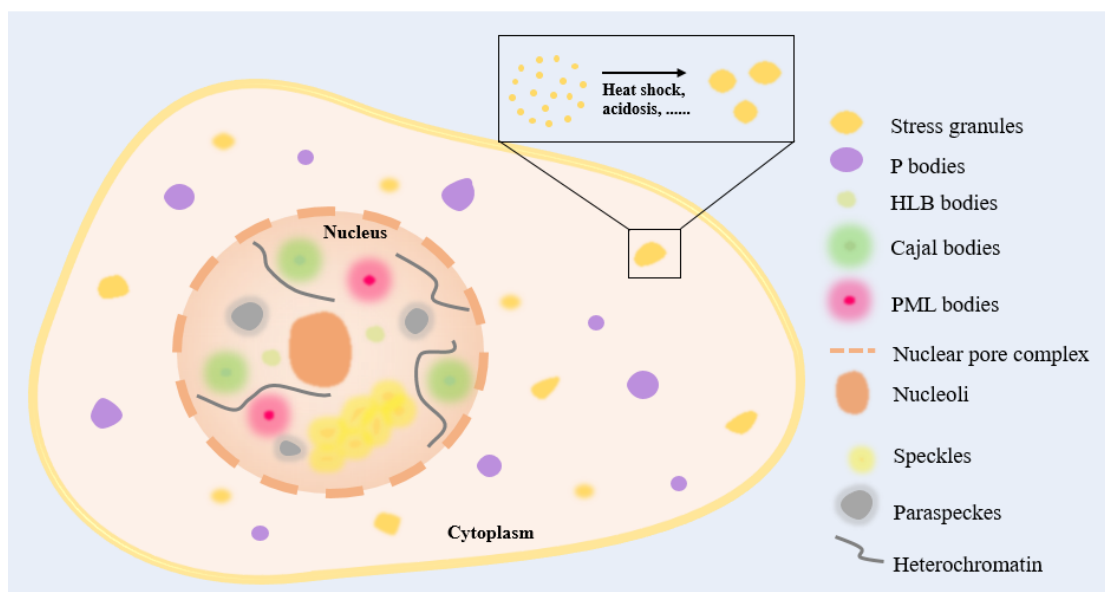


**Figure 3-3.** A schematic diagram of intracellular membraneless organelles formed by LLPS.

Besides participating in the assembly process of membraneless organelles, phase separation also takes part in the formation of membrane lipid rafts and cytoskeleton, as well as in cell sorting of biological tissues.<sup>78</sup> For example, the signal centre formed by transmembrane receptors,<sup>79</sup> assembly of membrane-binding proteins that initiates endocytosis,<sup>79</sup> and the osmotic barrier inside semi-nuclear pore complex (NPC),<sup>80</sup> the extracellular matrix protein

network,<sup>81</sup> the mitotic structure,<sup>82</sup> heterochromatin,<sup>83</sup> and the active gene transcriptional centre<sup>84</sup>. In conclusion, phase separation is playing a crucial role in the formation of different types of compartmentalization and the regulation of biomacromolecular reactions in cells. These discoveries have revolutionized our knowledge of cell structure and biochemistry.

### 3.3.2 LLPS in physiological function activities

The dense phases or aggregates formed by phase separation are the material basis of a number of stress sensors and nucleic acid sensors in the cell,<sup>38</sup> which enhance the adaptability of cells to external stress conditions<sup>2,7,8</sup> and promote the natural immune response of cells<sup>35</sup>, respectively. Riback et al. reported that yeast poly A binding protein 1 (Pab1) can be separated into a gel-like structure from a hypersensitive phase in solution under cellular stress conditions (for example, proteasome inhibition, acidosis, heat shock, hypoxia, DNA damage)<sup>85</sup>, acting as a physiological stress sensor to enhance the biocompatibility of cell.<sup>8</sup>

In addition to resisting stress, there are diverse nucleic acid sensors in cells to monitor viral invasion and simultaneously activate downstream immune pathways to resist viral infection. But how nucleic acid sensors activate the downstream signalling pathway in time by recognizing external viral nucleic acids efficiently in the cell? Zhijian J. Chen revealed the mechanism that long-chain dsDNA in cells activates the cGAS-cGAMP-STING immune signalling pathway by inducing phase separation of the nucleic acid sensor cGAS.<sup>35</sup> At the cellular level, long-chain dsDNA binds to the N-terminal of cGAS, which is disordered and positively charged, causing cGAS to nucleate and further concentrate to form liquid droplets by phase separation. Then, these droplets fuse with each other to produce larger spheres to activate cGAS and thus the cGAS-cGAMP-STING pathway. As a result, the synthesis of cGAMP depends on the degree of phase separation. It was found that free zinc ions can promote phase separation of dsDNA-cGAS and increase the activity of cGAS. Therefore, it is supposed that the chemical environment *in vivo*, such as charge density, may affect phase separation.<sup>26</sup> By comparing the phase behaviour of single-stranded DNA and double-stranded DNA with different lengths, Anisha found that local flexibility of DNA is another determinant of LLPS, not only charge patterns. And in the presence of double-stranded DNA, the second phase separation occurs, producing sub-molecules--liquid crystal dsDNA within the droplets.<sup>86</sup>

Gene transcription regulation is a basic activity in human life. Transcription factors generally consist of DNA binding domain and activation domain. Since the activation domain of most transcription factors contains low complexity amino acid sequences, i.e., IDPRs, which

are difficult to crystallize. Therefore, its molecular mechanism was not elucidated for a long time. Interestingly, the activation domains of different transcription factors have very low sequence similarity but are functionally interchangeable and can interact with the same coactivator complex.<sup>3,33,87,88</sup> Richard A. Young team discovered the phase separation ability of the activation domain of transcription factors, which depends on the IDPRs of the activation domain. The acidic amino acids of IDPRs provide electrostatic interaction of IDPRs-IDPRs between transcription factors and coactivators, promoting the phase separation and formation of condensates which involves in gene activation.<sup>3</sup> The model in which the activation domain of transcription factor functioning by a condensate formed with coactivator factor through LLPS explains how hundreds of transcription factors with low sequence similarity interact with the coactivators (Shown in Fig. 3-4b), which cannot be explained by the classic Lock-and-Key model (Shown in Fig. 3-4a).

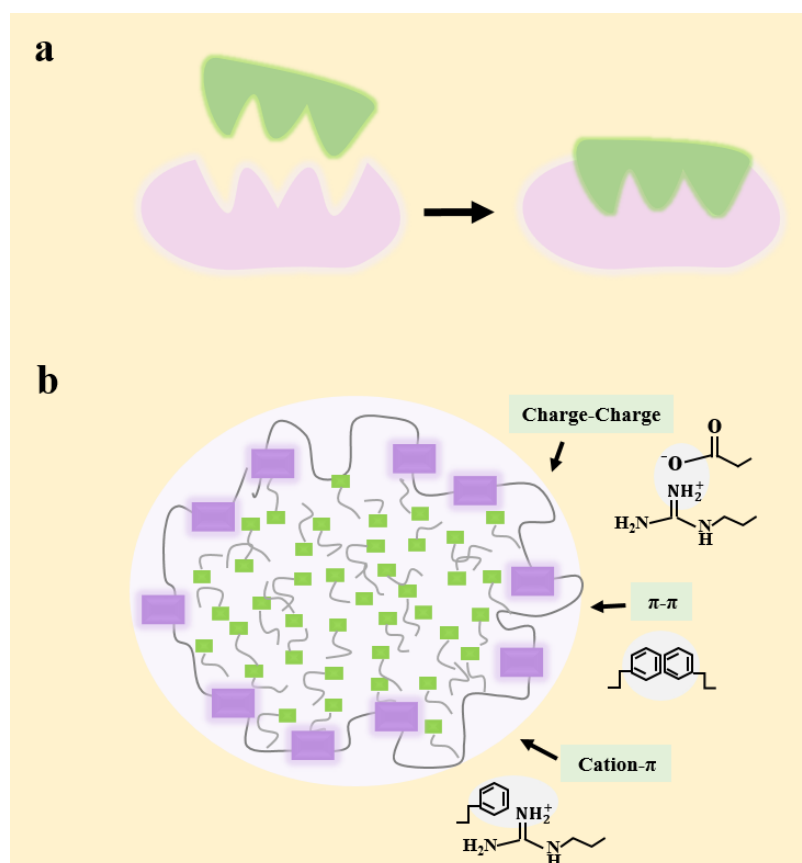


**Figure 3-4.** Comparison of two different interaction mechanisms of biomacromolecules *in vivo*. **(a)** Lock-and-key model by which proteins with defined tertiary structure binding with substrates and function. **(b)** LLPS processes by which biomacromolecules bind with their substrates and function.

In addition, recent high-resolution studies on the chromatin 3D organization of mammalian single cells have revealed that LLPS participates in regulating chromatin organization and gene expression. LLPS can also be used as a model to describe how individual gene loci respond to activation stimuli and how multiple chromatin loci achieve synergistic behavior.<sup>89</sup>

### 3.3.3 Mechanism of LLPS in the process of cellular activities

The lack of stable structures of distinct protein components appears to be critical for the phase separation and formation of various membraneless organelles in cells.<sup>75</sup> X. Fang et al. identified the functional requirements of FLL2 (a coiled-coil protein) in the formation of nuclear body of *Arabidopsis thaliana* FLA, demonstrating that coiled-coil protein can promote liquid-liquid phase separation.<sup>90</sup> Coiled-coils are alpha-helical super secondary structures that mediate protein-protein interactions and oligomerization.<sup>91</sup> The Arabidopsis RNA-binding protein FCA contains a prion-like domain that can phase separate *in vitro* and exhibits behaviour consistent with phase separation *in vivo*.

Phase separation at the cellular level is primarily driven by intermolecular interactions and shows protein/nucleic acid concentration dependence, multivalent dependence, IDPs/IDPRs dependence, and more. The ability of IDPs/IDPRs based on their homotypically or heterotypically dynamic association is essential to LLPS.<sup>89</sup> IDPs/IDPRs constitute agglomerates in many cells. These IDPs have low sequence complexity and flexible conformation, lack of hydrophobicity, and are rich in charged and polar amino acids, including glycine, serine, glutamine, proline, glutamic acid, lysine, and arginine. The polypeptide backbone composed of these residues can achieve charge-charge, cation- $\pi$  interaction, and  $\pi$ - $\pi$  stack interactions, enabling their multivalent interactions with DNA or RNA.<sup>92</sup> The lack of folded structures in IDPs/IDPRs is normally governed by the strong electrostatic repulsion between many similarly charged residues and the weak hydrophobic attraction between a few hydrophobic residues.<sup>93-95</sup> Charge patterns of IDPs/IDPRs are therefore critical for phase separation.

Although intrinsic protein disorders are essential in the intracellular LLPS activities, LLPS can also be triggered by interactions of well-folded proteins associated with phase transition. Phase separation can occur when the interacting macromolecule reaches a critical concentration and is assisted by multivalent interaction.<sup>96</sup> For example, the Nck-SH3 domain induces phase separation by multivalent interaction. The phase separation of Nck and N-WASP depends on the number of SH3 domains, one SH3 domain is not sufficient to induce phase

separation.<sup>97</sup> In contrast, Joshua indicated that a single Fyn-SH3 domain, which can be a multivalent binding platform itself for hnRNPA2 LC, is sufficient to induce phase separation of hnRNPA2 LC.<sup>98</sup>

Overexpression of key protein components is also sufficient to drive stress granules to assemble without any stimuli of stress.<sup>99</sup> Several membraneless organelles, including nucleoli and stress granule, assemble only when the components are denser than the concentration threshold.<sup>100,101</sup> Studies on the phase transition theory of polymer systems (including proteins, DNA, and RNA) have shown that polymer solutions are more susceptible to phase separation because the configuration entropy of a single chain effectively reduces the energy contribution of the mixed entropy. The system tends to reach the lowest energy state in terms of the phase transition thermodynamics, which is determined by the combination of entropy and enthalpy.<sup>92</sup> Multivalent interactions of protein-protein or protein-DNA/RNA are principal drivers of phase separation of complexes associated with an intracellular signalling pathway. These proteins generally have an SH3 repeat domain that can bind proline-rich motifs.<sup>98,102,103</sup>

The knowledge about molecular mechanisms controlling intracellular phase separation is constantly being enriched, but it still needs to be further investigated. In the future, more research is required to construct a more comprehensive mechanism network, so that scientists can better understand and influence the formation process of LLPS to develop treatments for related diseases.

### **3.4 LLPS involved in pathological activities**

#### **3.4.1 Diseases caused by phase separation**

Liquid-like condensate is not the only result of LLPS. The metastable dense liquid formed by phase separation is the precursor of a solid-state protein. The concentrated protein solution will further aggregate to form a solid phase such as precipitate, crystal, or amyloid fibre. These solid-phase aggregates can be the molecular basis of various human diseases.

These solid phases may be formed by ordered proteins with a stable 3D structure, such as nucleolar aggregates found in human breast and prostate cancer tissue,<sup>104,105</sup> lens proteins that cause cataract and haemoglobin in sickle cell anaemia disease, respectively.<sup>106,107,108,109,31</sup> Toyochi Tanaka measured the protein diffusion coefficient in the lens of cataract humans, revealing the presence of a large number of protein aggregates, which is the result of phase separation of lens protein-aqueous solution.<sup>110</sup>

On the other hand, the natural unfolded IDPs participate in most of the neurodegenerative diseases, such as Alzheimer's disease (AD), Parkinson's disease (PD), amyotrophic lateral

sclerosis (ALS), frontotemporal dementia (FTD), and traumatic brain injury (Protein molecules of TBI), Huntington's disease.<sup>111–116</sup> The major neurodegenerative diseases caused by phase separation of related proteins are summarized in Table 3-1. Neurodegenerative diseases are protein deposition diseases characterized by the formation and accumulation of extracellular amyloid fibrils or intracellular inclusion bodies with amyloid-like characteristics.<sup>117</sup> Among them, prion diseases can induce diseases by spreading protein-infected factors that misfold and aggregate proteins, and thus such proteins are called prions. The prion-like domain has low-complexity and exists in approx. 240 human proteins. Proteins with prion-like domains are inherently easy to aggregate and carry on LLPS causing neurodegenerative diseases.<sup>118</sup> Abhisek reviewed the molecular mechanism of prion-like transmission of protein aggregates.<sup>119</sup>

The concentration of intracellular RNA can regulate the phase separation behaviour of prion-like RNA-binding proteins (RBPs). Changes in RNA or the RNA-binding ability of RBPs can cause abnormal phase transitions. For example, high RNA/protein ratios in the nucleus can prevent the phase separation and aggregation of RBPs, while a low RNA/protein ratio in the cytoplasm promotes the phase separation of RBPs and the formation of solid pathological aggregates.<sup>120</sup> Even so, the current molecular mechanisms for regulating the phase separation behaviour of intracellular IDPs/IDPRs and the factors involved in it are limited, more relevant research is needed to improve this knowledge system in the future.

**Table 3-1. Neurodegenerative diseases caused by protein phase separation**

Neurodegenerative Diseases		Proteins
Synucleinopathies	Parkinson's disease (PD)	$\alpha$ -synuclein
	Dementia with Lewy bodies	$\alpha$ -synuclein
	Multiple system atrophy (MSA)	$\alpha$ -synuclein
	Hallervorden–Spatz disease	$\alpha$ -synuclein
Taupathies	Alzheimer's disease (AD)	Tau, Amyloid- $\beta$ (A $\beta$ ), $\alpha$ -synuclein fragment
	Traumatic brain injury (TBI)	Tau
	Motor neuron disease with neurofibrillary tangles	Tau
	Progressive supranuclear palsy	Tau
	Corticobasal degeneration	Tau
	Niemann–Pick disease type C	Tau
	Subacute sclerosing panencephalitis	Tau
	Myotonic dystrophy	Tau
	Argyrophilic grain disease	Tau
Other types	Amyotrophic lateral sclerosis (ALS)	FUS, superoxide dismutase (SOD1), TDP-43, hnRNAP1, chromosome 9 ORF



		72 (C9ORF72), angiogenin (ANG), survival motor neurons (SMN1) protein
	Frontotemporal dementia (FTD)	FUS, TDP-43, hnRNAP1, chromosome 9 ORF 72 (C9ORF72)
	Down's syndrome	Nonfilamentous amyloid- $\beta$
PolyQ repeat diseases	Huntington's disease	Huntingtin protein with polyQ expansion
	Spinocerebellar ataxias	Ataxins with polyQ expansion
	Spinocerebellar ataxia type 2 (SCA2)	Ataxin-2
	Machado–Joseph disease (MJD/SCA3)	Ataxin-3
	Spinocerebellar ataxia type 2 (SCA6)	P/Q-type calcium channel $\alpha$ 1A subunit
	Spinocerebellar ataxia type 2 (SCA7)	Ataxin-7
	Spinocerebellar ataxia type 17 (SCA17)	TATA box-binding protein with polyQ expansion
	Spinal and bulbar muscular atrophy	Androgen receptor with polyQ expansion
	Dentatorubral–pallidoluyisian atrophy (DRPLA)	Atrophin-1
Prion diseases/ Transmissible spongiform encephalopathies	Creutzfeldt–Jakob disease (CJD)	Prion proteins or fragments
	Gerstmann–Sträussler–Scheinker (GSS) disease	
	Fatal familial insomnia (FFI)	
	Scrapie in sheep	
	Bovine spongiform encephalopathy (BSE)	
	Chronic wasting disease (CWD) in mule deer and elk	
Familial dementias	Familial British dementia	ABri
	Familial Danish dementia	ADan

### 3.4.2 Diseases caused by the disruption of phase separation process

Since LLPS fulfil numerous physiological function activities. It is obvious that the abnormal phase separation triggered by protein mutation or environmental stress may cause severe disorders of related physiological functions and lead to diseases. A typical case is SPOP (Speckle-type POZ protein), a tumour suppressor, which is an E3 ubiquitin ligase receptor protein, usually mutated in prostate cancer and other solid tumours. Bouchard et al. found that substrate binding is required for the accumulation of SPOP complexes in membraneless organelles formed by phase separation. Mutations of cancer-associated SPOP disrupt the colocalization and phase separation of SPOP-substrate. Thereby, reducing ubiquitination and

degradation of substrates results in the accumulation of proto-oncogene proteins and the formation of cancer.<sup>121</sup>

Due to the richness of IDPs/IDPRs *in vivo* and the key role of LLPS in many signalling pathways, their dysfunction is highly associated with the pathogenesis of various human diseases.<sup>39–42,119,122–124</sup> In addition, it was reported that a large number of sites of post-translational modifications (such as acetylation, hydroxylation, ubiquitination, methylation, phosphorylation, etc.) are often located within IDPRs, or in the vicinity of its sequence. This makes the phase separation of related IDPRs more likely to be affected, resulting in loss or abnormality of related physiological functions, leading to disease occurrence.<sup>125–128</sup>

## **3.5 Biological significance and value of LLPS**

### **3.5.1 Theoretical value**

The study of liquid-liquid phase separations has been highly concerned, as the basis for studying dynamic order/disorder phenomena. So far, the main research targets of structural biology are mostly structurally stable biomacromolecules and their complexes. These biomacromolecules and their complexes often have relatively defined spatial structures, which can be studied by existing structural analysis methods. However, many bioactive proteins do not form a relatively low-energy, single folded structure, such as intrinsically disordered proteins (IDPs), which lack stable tertiary and/or secondary structures under *in vitro* physiological conditions. IDPs complement the function of folded proteins and are material basis of many physiological activities as well as pathological activities that cannot be ignored. Obviously, such biomacromolecules are difficult to be analysed by traditional structure analysis methods, such as X-ray diffraction crystallography, due to the lack of a stable conformation. It is also challenging to explain their biological functions using the classical Lock-and-Key model as shown in Fig. 3-4. Therefore, how these biomacromolecules function in cells has been a mystery for structural biologists before the discovery of LLPS. In recent years, the research of LLPS has inspired the study of large structural motions and fluctuations, also shed light to reveal the function of such biological macromolecules, supporting to understand the rules of life more completely.

Further, it is worth noting that in addition to IDPs/IDRs, other proteins with defined structures also can undergo a LLPS process, meaning that the structurally defined proteins may also function through the LLPS way. Therefore, LLPS provides a new approach to interpret biomacromolecules functioning mechanisms, which is different from the traditional Lock-and-Key mechanism, which is of great significance.

### 3.5.2 Application value

The use of polymer blends improves the adjustability of the drug-loaded fibres, and an understanding of the phase behaviour of polymer blends facilitates the development of sustained-release drugs.<sup>27,30,129</sup> The hollow fibres formed by phase separation have higher performance in drug loading and release kinetics.<sup>28,130</sup> Secondly, nanostructures of core-shell and uniformly dispersed microstructures can be obtained by controlling phase separation processes. Bromberg et al. used light scattering to study the kinetics of the formation of human insulin particles in an insulin-PEG-water ternary system under rapid cooling, by which the relatively monodispersed and uniform spherical insulin particles were formed.<sup>131</sup> The thermally induced phase separation technology is used to rapidly prepare monodisperse porous microspheres. This technology supports the uniform encapsulation of granular fillers and drugs, and can improve the efficiency of drug encapsulation.<sup>129</sup> By analysing and controlling the kinetic parameters that affect the phase separation behaviour, the drug release rate also can be optimized.<sup>29,26</sup> Drug-enriched phase formed by LLPS provides a solution for the transmembrane transport of drugs with low water solubility.<sup>27</sup> Ming Tan et al. reported that Norovirus P particles, a protein aggregate formed by LLPS, can be used as an excellent carrier for enhancing the immunogenicity of external antigens.<sup>132</sup> It has broad application advantages in vaccine development and antibody production.<sup>133,134</sup>

On the other hand, the presence of LLPS in the preparation of drugs causes physical instability of the formulation, such as LLPS in the preparation of monoclonal antibodies.<sup>23,135</sup> Therefore, control of the LLPS process can provide solutions for pharmaceutical engineering and new insights for protein dynamics and drug designment.

### 3.6 Questions remain to be addressed

As described before, LLPS behaves like a double-edged sword in a biological system. A comprehensive and in-depth understanding of the general physicochemical rule of the phase separation process is necessary for providing a theoretical basis to control LLPS towards crystallization or to prevent pathological LLPS. For example, the following specific questions and the possible solutions:

- 1) Kinetics of the LLPS process and its role in the subsequent processes from the aspect of biophysical sciences. As a classical phase transition phenomenon, protein crystallization is an ideal model for studying the LLPS process and its subsequent results, such as crystal distribution, size, quantity, quality, etc.

2) The effective and universal methods for modulating the LLPS process. Based on the obtained knowledge, LLPS takes place *in vivo* mainly through weak interactions (charge-charge,  $\pi$ - $\pi$ , cation- $\pi$ ) of proteins and nucleic acids. These interactions can be influenced by biochemical methods (mutations in amino acid sequences), chemical methods (varied pH and salt), or physical methods (application of external fields). Studies have shown that electric and magnetic fields can affect protein crystallization,<sup>136</sup> which indicates that electric and magnetic fields could also have effects on the LLPS process.<sup>137-141</sup>

Considering the wide application of electric fields in crystallography and healthcare fields and its existence in physiological cell activities, this work investigated the effect of physicochemical parameters of ionic strength and electric fields on the kinetics of protein phase separation, the subsequent phase transition, and the underlying mechanism.

## 4 Aims and Outline

Several model proteins especially glucose isomerase (GI), which has been extensively studied to understand the crystal nucleation theories, were selected and investigated firstly to address the mentioned questions. In this project, those selected model proteins were utilized to establish a methodology for investigating the effect of ionic strength and electric fields (EFs) on the protein LLPS/aggregation kinetics, the subsequent phase transition, and the corresponding underlying mechanism.

Both crystals and fibrils can be the final resultant products of the liquid-to-solid phase transition of protein intermediates, the former is the critical point to obtain protein spatial structures via X-ray diffraction and the latter is the pathogenesis of many neurodegenerative diseases. However, the formation of both products at early stages may share a similar mechanism of LLPS. Therefore, this work investigated protein LLPS in both pathways leading to crystallization and fibrillation, to better understand the role of LLPS in the formation of polymorphic protein aggregates and the effect of physicochemical parameters on this process.

For this aim, experiments have been designed and performed systematically as described below to elucidate the general physicochemical laws of protein LLPS, to analyse the influences of EFs and ionic strengths on the protein LLPS that appeared in different pathways, and to explore physicochemical means to effectively intervene the LLPS process.

### 1) Preliminary study of the effect of pulsed EFs on protein LLPS *in vitro* (Publication 1)

- Designing the setups to apply pulsed EFs to protein solutions which can be observed by optical microscopes.
- Observing protein LLPS via optical microscopy and the influence of pulsed EFs with different layouts and waveforms applying different proteins (GI, ovalbumin, BPTI,  $\beta$ -lactoglobulin, haemoglobin).
- Analysing the dependence of protein's response to EFs considering the net charge and dipole moment of the corresponding proteins.
- Preliminary comparison of protein phase transition, spatial distribution, and morphologies of protein DLCs/nuclei, and analysing the protein secondary structure under different EF conditions.

### 2) Kinetics studies of protein LLPS in the pathway of crystallization and the modulation effect of ionic strength and pEFs (Publication 2)

- Effect of varied ionic strengths on electrostatic interactions, early-stage condensing, and prenucleation 3D-ordering of GI.
- Effect of crowding agents on condensing and prenucleation ordering of GI.
- Effect of a pEF on the prenucleation condensing and 3D-ordering of GI under different ionic and crowding conditions.
- Effect of mesoscopic ordered clusters (MOCs) induced by a pEF on GI crystallization.
- Validating the effect of the pEF on the prenucleation condensing and 3D-ordering of protein and the effect of MOCs on protein crystallization applying the Pdx complex of *S. aureus*.

**3) Modulating the kinetics of protein phase separation and the properties of mesoscopic protein assemblies during fibrillation applying a NaCl gradient and a distinct pEF (Publication 3)**

- Phase diagram of  $\alpha$ -synuclein (ASN) in solution.
- Monitoring the dynamic assembling and 3D-ordering of ASN in a NaCl gradient exposed to a pEF.
- Characterizing the morphologies,  $\beta$ -sheet structures, and autofluorescence effect of assembled ASN.
- Characterizing the thermostability of monomeric and assembled ASN.
- Analysing the diffusion interaction parameter ( $K_D$ ) and the secondary structure of monomeric ASN under different ionic and EF conditions.

## 5 Results

### Summary of the publications presented in this section

Briefly, a novel method was established to apply the protein crystallization/fibrillation process as a model to investigate protein phase separation and the effect of electric fields on this process. The data obtained enriched the understanding of the physicochemical mechanism of protein phase separation and the role of mesoscopic protein clusters in crystallization/fibrillation. The results of this project also provided the theoretical basis for influencing protein phase separation by physicochemical means. The results shown in this section followed the structure as described in the outline of the work:

- 1) Preliminary study of the effect of pulsed EFs on protein LLPS *in vitro* applying GI and four other model proteins.
- 2) Kinetics studies of protein LLPS in the pathway of crystallization and the modulation effect of ionic strength and a distinct pEF.
- 3) Modulating the kinetics of protein phase separation and the properties of mesoscopic protein assemblies during the fibrillation pathway of Alpha-synuclein applying a NaCl gradient and a distinct pEF.

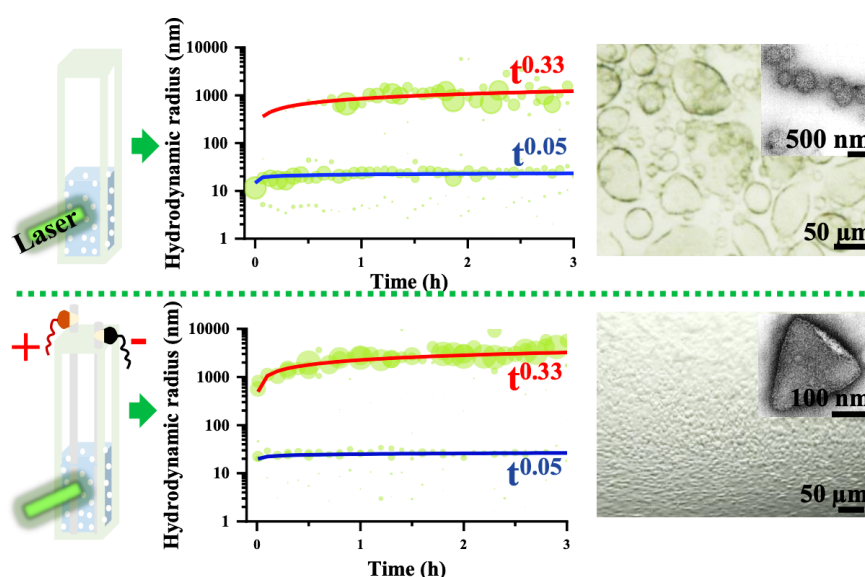
### Summary of contributions

For the three first-authorship publications presented below, I designed and executed the experiments, evaluated and interpreted the data, and wrote the original manuscripts. For the publication in the *Crystals* journal, I shared the first authorship with A. Barra considering the value of the results obtained from the Pdx protein provided by Barra. I contributed to the major of the work, including designing and performing all experiments, evaluating and interpreting data, and writing the manuscript.

## 5.1 Pulsed electric fields induce modulation of protein liquid-liquid phase separation (LLPS)

### Summary

This article describes the screening investigations and corresponding results of protein LLPS exposed to pulsed electric fields (pEFs), generated by five different waveforms and two electrodes' configurations. Five proteins including glucose isomerase (GI), selected according to their distinct chemical and biophysical parameters, were used to study how the dipole moment and net charge of a protein can affect the response to pEFs. Morphologies and phase transitions of GI dense liquid clusters (DLCs) formed via LLPS under pEFs were analysed further and compared via optical microscopy and transmission electron microscopy. The effect of pEFs on the kinetics of protein LLPS and the secondary structures of monomeric proteins were also investigated and discussed. And the results obtained clearly indicate that proteins having higher dipole moments are more influenced by pEFs. pEFs can effectively drive protein LLPS in terms of kinetics, spatial distributions, and morphologies of DLCs. Among the five waveforms and two configurations tested, a pEF generated by waveform 4 and platinum wire electrodes induced the formation of homogeneous DLCs which transitioned subsequently to homogeneous crystal nuclei.



**Graphic abstract.** Comparison of the growth kinetics and morphologies of GI DLCs without and with the application of a pEF.<sup>142</sup> The upper and lower panels show the scheme of protein solution in the DLS cuvette without and with the application of a pEF, respectively, and the representative results of DLS radius plots, optical microscopy image, and TEM image of GI DLCs/nuclei.





Cite this: DOI: 10.1039/d0sm01478h

 Received 13th August 2020,  
Accepted 3rd September 2020

DOI: 10.1039/d0sm01478h

rsc.li/soft-matter-journal

## Pulsed electric fields induce modulation of protein liquid–liquid phase separation†

 Mengying Wang,<sup>a</sup> Sven Falke,<sup>a</sup> Robin Schubert,<sup>b</sup> Kristina Lorenzen,<sup>b</sup> Qing-di Cheng,<sup>a</sup> Christian Exner,<sup>a</sup> Hévila Brognaro,<sup>a</sup> Célestin Nzanzu Mudogo<sup>c</sup> and Christian Betzel<sup>\*a</sup>

The time-resolved dynamic assembly and the structures of protein liquid dense clusters (LDCs) were analyzed under pulsed electric fields (EFs) applying complementary polarized and depolarized dynamic light scattering (DLS/DDLS), optical microscopy, and transmission electron microscopy (TEM). We discovered that pulsed EFs substantially affected overall morphologies and spatial distributions of protein LDCs and microcrystals, and affected the phase diagrams of LDC formation, including enabling protein solutions to overcome the diffusive flux energy barrier to phase separate. Data obtained from DLS/DDLS and TEM showed that LDCs appeared as precursors of protein crystal nuclei, followed by the formation of ordered structures within LDCs applying a pulsed EF. Experimental results of circular dichroism spectroscopy provided evidence that the protein secondary structure content is changing under EFs, which may consequently modulate protein–protein interactions, and the morphology, dimensions, and internal structure of LDCs. Data and results obtained unveil options to modulate the phase diagram of crystallization, and physical morphologies of protein LDCs and microcrystals by irradiating sample suspensions with pulsed EFs.

### Introduction

Today it is widely established that liquid–liquid phase separation (LLPS) is involved in biomineralization,<sup>1</sup> nucleation of ice crystals,<sup>2</sup> the origin of life,<sup>3</sup> and protein crystal nuclei formation.<sup>4</sup> However, LLPS of proteins and particularly RNAs in cells gained substantial attention in recent years, as it was found that LLPS is the driving mechanism for the formation of

membrane-less organelles, such as nucleoli, centrosomes, stress granules, Cajal bodies, P bodies and others.<sup>5,6</sup> Further, LLPS is seen as the fundamental process within the formation of *in vivo* grown crystals and amyloid formation,<sup>7</sup> the pathological basis for several diseases. Examples are cytoplasmic phase separation in the formation of cataract, Charcot–Leyden crystals in allergic diseases, crystallization of hemoglobin C in hemolytic anemia, ragged-red fibers in mitochondrial myopathies and hematin crystals in malaria.<sup>8–14</sup>

Macromolecules forming LDCs in biological systems are proteins and nucleic acids, which are heterogeneously charged, with highly individual electrostatic surface potential distributions, distinct dipole moments and three-dimensional structures.<sup>15</sup> RNA, DNA molecules and the polypeptide chains of proteins are at least partly polar, thereby form ionic, ion– $\pi$  and  $\pi$ – $\pi$  interactions, which stabilize their 2D and 3D structures and facilitate intermolecular interactions, supporting the formation of stable liquid dense clusters (LDCs).<sup>16</sup> Research efforts to understand the LLPS in biological systems have mainly focussed on identifying the role of LLPS in stress-related and pathologically relevant processes.<sup>17,18</sup> Biophysical investigations focussed on exploring the determining factors of protein LLPS, such as specific amino acid sequences, distinct protein secondary structures, pH, temperature and external forces.<sup>17,19–24</sup> However, due to the individual structural complexity of biomacromolecules, knowledge about (I) physicochemical parameters that influence LLPS, and (II) methods to modify biomacromolecular LDCs *via* external forces, *e.g.* magnetic fields and electric fields,<sup>25–28</sup> is still rather incomplete. Conversely, for homopolymers and nanocomposites the mechanisms of LLPS formation have already been well investigated.<sup>29–36</sup> In this context, external force fields, especially electric fields (EFs), controlling motion and phase separation of nanoparticles were applied to obtain and prepare nanomaterials with specific structures and functions, *e.g.* carbon nanotubes, nanowires and conducting polymers.<sup>37,38</sup>

Experiments analyzing the effect of EFs on biological systems and biomolecular suspensions focused till now predominantly on

<sup>a</sup> Institute of Biochemistry and Molecular Biology, Laboratory for Structural Biology of Infection and Inflammation, c/o DESY, Build. 22a, Notkestr. 85, 22607, Hamburg, Germany. E-mail: Christian.Betzel@uni-hamburg.de

<sup>b</sup> European XFEL GmbH, Holzkoppel 4, 22869 Schenefeld, Germany

<sup>c</sup> Department of Basic Sciences, School of Medicine, University of Kinshasa, Kinshasa, Democratic Republic of Congo

† Electronic supplementary information (ESI) available. See DOI: 10.1039/d0sm01478h



investigating the impact of EFs on protein crystallization,<sup>25,26,39,40</sup> protein dynamics,<sup>41</sup> protein conformation/structure,<sup>42–47</sup> and cellular morphologies.<sup>48</sup> Experimental efforts to understand the influence of EFs on the formation of protein LDCs have only rarely been performed. Hence, applying EFs during protein LDCs formation will provide insights into opportunities to modulate protein LDCs by EFs. Therefore, we applied polarized and depolarized dynamic light scattering, optical and transmission electron microscopy and circular dichroism spectroscopy to analyze the dynamics of the LDCs assembling process, the internal structure and order of protein LDCs, as well as the secondary structure content of proteins exposed to EFs.

## Results and discussion

### Monitoring protein LLPS applying optical microscopy

To investigate the influence of EFs on protein LLPS, a platinum wire (Pt) and a parallel conductive glass (PCG) EF experimental setup were used to expose suspensions of glucose isomerase (GI), ovalbumin, bovine pancreatic trypsin inhibitor (BPTI), and  $\beta$ -lactoglobulin solutions to five different pulsed waveforms (ESI,† Fig. S1), which were applied for the first time by A. Rodríguez-Romero *et al.*<sup>40</sup> to investigate effects of alternating electric fields on crystal growth. The proteins were selected according to their distinct chemical and biophysical parameters summarized in ESI,† Table S1. Experimental materials, procedures and methods applied are also summarized in the ESI.†

In Fig. 1 GI LDCs and microcrystals obtained after 5 hours applying the Pt EF setup (Fig. 1a and b), PCG EF setup

(Fig. 1c and d) and no EF (control), respectively. Overall negatively charged GI at pH 6.5 formed LDCs with dimensions of 1–5  $\mu\text{m}$  around the anode when Pt EF waveforms 1–3 were applied (wave 1–3 of Fig. 1a and b). Rectangular crystals were observed at the boundary of LDCs (wave 3 in Fig. 1b). Pt EF waveforms 4 and 5 induced the formation of LDCs with a uniform diameter of approx. 2  $\mu\text{m}$  equally distributed in the entire droplet (wave 4–5 in Fig. 1a and b). In Fig. 1c and d, PCG EFs between two parallel conductive glasses guided GI to form homogeneously shaped LDCs with approx. dimensions of 25  $\mu\text{m}$  under each pulsed waveform. Microcrystals occurred after a phase transition of LDCs applying waveforms 1–5 (waves 1–4 as shown in Fig. 1c and waves 2 and 5 as shown in Fig. 1d). A representative evolving process of GI LDCs formed under different EF conditions is shown in Fig. 2. In the control group (Fig. 2a1–a3), GI LDCs evidently showed Ostwald ripening<sup>49</sup> and resulting clusters have different dimensions and shapes. Interestingly, GI LDCs formed within the PCG EF setup (Fig. 2b1–b3) and Pt EF setup (Fig. 2c1–c3) did not coalesce with neighboring LDCs, probably due to electrostatic repulsion between LDCs under an EF. Instead, a transition from LDCs with high protein concentration to microcrystals with geometrically ordered structure in both EF setups was observed, respectively. Based on these results, it is concluded that GI LDCs and microcrystals formed with the PCG EF setup had larger dimensions and uniform spatial orientation, which may attribute to the parallel EF lines between two parallel conductive glass plates (ESI,† Fig. S1b–EF lines). Nevertheless, the Pt EF setup, particularly when applying waveforms 4 and 5, demonstrated advantages to facilitate the formation of GI LDCs and microcrystals with similar dimensions and similar morphology.

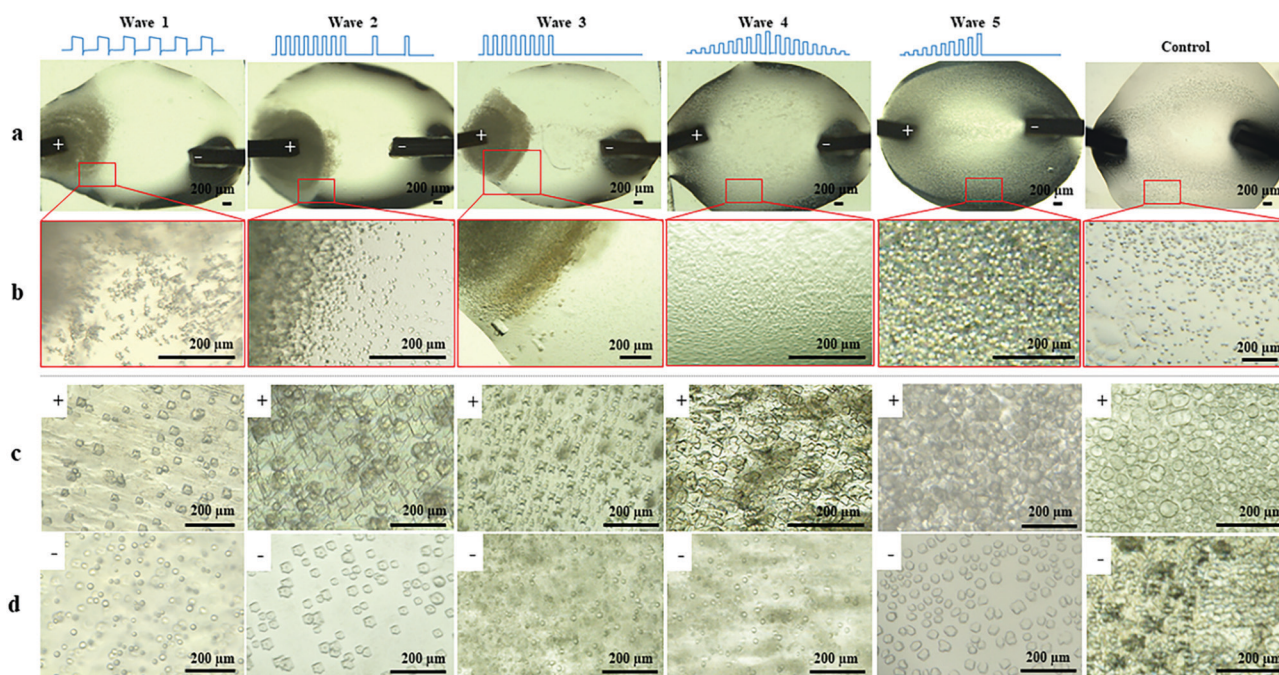


**Fig. 1** GI LDCs and microcrystals formed with EFs and without EFs (control), respectively. (a) GI droplets under different Pt EF waveforms. (b) Magnified views of corresponding droplet areas indicated in Fig. 1a by red squares. GI LDCs and microcrystals formed (c) at the anode side and (d) at the cathode side in the PCG EF setup with different waveforms.





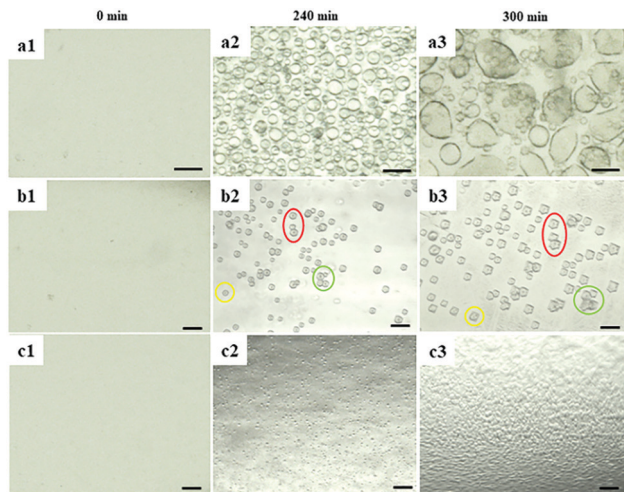


Fig. 2 Pictures showing the evolution processes over 5 hours of GI phase transition (a1–a3) without application of EFs (b1–b3), with an EF applying the PCG EF setup (c1–c3), with an EF applying the Pt EF setup. Red, yellow, and green circles in images (b2) and (b3) show the same GI LDCs after different evolving time. Scale bar: 50  $\mu\text{m}$ .

Images showing effects of pulsed EFs on the LDCs formation for the other three proteins (BPTI, ovalbumin, and  $\beta$ -lactoglobulin) were also recorded (ESI,† Fig. S3–S5). Different to GI, no quasi-crystals or microcrystals, only morphological changes of LDCs were observed for the other three proteins under EFs. The LDCs formation of BPTI under the selected condition is temperature dependent.<sup>50</sup> No supersaturation or LLPS was observed after mixing BPTI with KSCN at 20 °C when an EF was absent. However, BPTI LDCs appeared in the same condition after 1 hour under Pt EFs (ESI,† Fig. S4), which obviously indicated that the pulsed EF supported the formation of attractive forces in the BPTI solution and thereby supported phase transition. In contrast, it was also observed that LLPS of ovalbumin was impeded by applying pulsed EFs with waveforms 1, 2 and 4 (ESI,† Fig. S3). The inhibited LLPS process of ovalbumin was irreversible when applying the Pt EF setup with waveform 2, which was probably caused by the high frequency and amplitude of waveform 2. For  $\beta$ -lactoglobulin, LDCs nearby the cathode were smaller and more uniform than those nearby the anode due to the negative protein net charge. Compared to the results obtained by using GI, no obvious differences of LDCs morphology and geometrically ordered structures were observed with these three proteins exposed to different pulsed EFs. Hence, GI was identified to be a beneficial model protein to analyze the effects of pulsed EFs on protein phase transition in more detail and structural properties of LDCs, as described in the following sections.

### Polarized and depolarized dynamic light scattering (DLS/DDLS)

DLS/DDLS was utilized to analyze whether pulsed EFs influence the dynamic assembly and internal structure of protein LDCs at the early stage of LDCs formation. Based on the birefringence of material with lattice order exposed to laser light DDLS can distinguish ordered and amorphous material.<sup>51–53</sup> Due to a

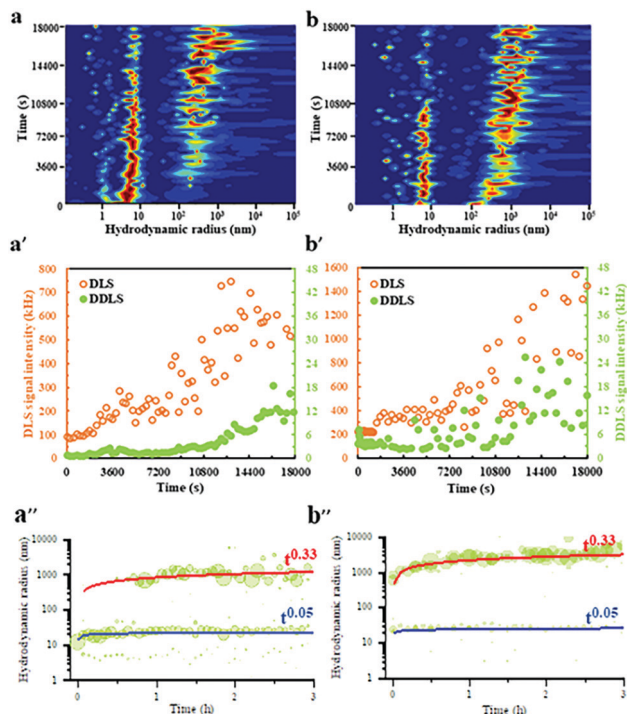


Fig. 3 Hydrodynamic radius distributions of GI (a) without and (b) with application of a pulsed EF (waveform 4,  $V_{\text{max-500}\Omega} = 20$  V) over time. (a') and (b') show the corresponding DLS/DDLS signal intensities without and with an EF, respectively. Kinetic evolution of the hydrodynamic radii (nm) for GI (a'') without and (b'') with an EF.

spatial limitation of the DDLS cuvette, Pt wire electrodes were assembled at the DDLS cuvette to produce a pulsed EF with waveform 4 ( $V_{\text{max-500}\Omega} = 20$  V) during DLS/DDLS measurements (ESI,† Fig. S2). PEG20 000 was added at the beginning of the measurement to induce supersaturation of the GI solution. In the control group, without application of a pulsed EF, a particle fraction with a large hydrodynamic radius of approx. 300 nm appeared after 3600 s measurement (Fig. 3a) accompanied by an obvious increase of DLS signal intensity (Fig. 3a'), indicating an initial formation of GI LDCs. An increase of the corresponding DDLS signal intensity was only detected after 12 600 s along with the growth of GI LDCs in size (Fig. 3a'), demonstrating the initiation of nuclei formation with lattice order. The contribution of multiple scattering to the DDLS signal intensity can be neglected when the DLS signal intensity of measurements is lower than 5000 kHz.<sup>51</sup> Hence, this result revealed a nucleation process with two steps, as proposed by P. Vekilov and others, *i.e.* the crystal nucleus occurs within an LDC.<sup>54</sup> Nevertheless, when a pulsed EF with waveform 4 was applied during the whole measurement, the fraction with hydrodynamic radii of approx. 300 nm appeared rapidly at the beginning of the measurement and grew steadily to a larger population with radii of 1–5  $\mu\text{m}$  (Fig. 3b). In parallel, a noticeable fluctuation of the DDLS signal intensity was detected after a short time increase of DLS signal intensity (Fig. 3b'), indicating an initial formation of ordered structures at the early stages of LDCs formation. The dynamic scaling law, which supposes the evolution of the droplet size



distribution over time ( $R = kt^n$ ) predicated a power law dependence on time ( $n$ ) and a prefactor ( $k$ ), supports the identification of specific growth/coarsening mechanisms involved in the cluster formation.<sup>55</sup> The kinetic evolution of hydrodynamic radii over 3 hours without (Fig. 3a'') and with application of EF (Fig. 3b'') was plotted and shows an obvious power law coefficient ( $t^{0.33}$ ), which represents the diffusion-limited growth in supersaturated solutions.<sup>56</sup> Thereby, we assume that (I) pulsed EFs can support protein solutions overcoming the diffusion limitation to form LDCs, and (II) pulsed EFs can accelerate the transition process from a liquid dense phase to an ordered phase.

### Transmission electron microscopy (TEM)

TEM was applied to visualize and compare GI LDCs obtained with and without a pulsed EF at the nanoscale. A pulsed EF with waveform 4 ( $V_{\max-500\Omega} = 20$  V) was applied to GI solution during the whole process of sample preparation for a total of 5 hours. Images in Fig. 4a–c show GI LDCs formed in the presence of the pulsed EF, with a uniformly triangular shape and size around 300–400 nm. Two kinds of nuclei according to the appearance were identified. However, one of them showed relatively gentle corners and curved edges surrounded by amorphous protein molecules (Fig. 4d), indicating a primary stage of nucleation.

Another nucleus, presumably in an advanced nucleation stage with sharp faceted corners and straight edges, forming a perfect rigid and rather triangular structure is shown in Fig. 4e. Furthermore, an obvious electron diffraction pattern was observed (inset of Fig. 4e), confirming the initial 3D structure of a matured nucleus. LDCs in the control group (Fig. 4f), without application of an EF show amorphous shape and random size distribution. Additionally, no nucleus or nucleus-like shape was observed in the control group. It is notable that only LDCs or nuclei with size under 500 nm were fixed on the grids and observed by TEM. According to results of the DDLs signal intensity (kHz), ordered structures occurred only after LDCs grew to a micro meter size in the absence of an EF, however, birefringence was detected at the early stages of LDCs formation under EFs. This may explain why no nuclei or ordered phases were observed by TEM in the control group. Thereby, results of TEM experiments are in good agreement with the DDLs results obtained.

### The role of net charge and dipole moment during the influence of EFs on protein LLPS

According to the results summarized before, questions of why different proteins showed different responses to pulsed EFs and why different pulsed waveforms induced different protein phase behaviors were investigated considering three factors: dipole moment, surface net charge and secondary structure composition of the proteins.

As shown in ESI,† Fig. S6, it is known that molecules with an overall net charge in solution move to the oppositely charged electrode when exposed to an EF. However, proteins also possess an intrinsic electric dipole moment based on the spatial position and orientation of charged amino acids, and the orientation of secondary structure elements, particularly of  $\alpha$ -helices. It was reported that EFs show more influences on proteins with higher dipole moments than on proteins with lower dipole moments.<sup>42</sup> The resulting dipole moment is defined as:

$$\vec{q} = \sum_{i=1}^n q_i(i)\vec{r}_i$$

where  $n$  is the total number of protein atoms,  $q_i$  is the charge of the atom  $i$ ,  $r_i$  is the directional vector of each atom.<sup>45</sup>

Based on this correlation, we investigated the influence of EFs on the phase behaviors of proteins with different electric dipole moments. Results obtained are shown in ESI,† Fig. S7. During the experiments, negatively charged GI particles, with a dipole moment of 1082 D ( $1 \text{ D} = 1 \times 10^{-18} \text{ statC cm}$ ), moved to the anode and formed LDCs within 15 minutes after applying the EF. BPTI and  $\beta$ -lactoglobulin, with relatively low dipole moment compared to GI, formed LDCs around the electrode much slower. However, hemoglobin, with the lowest dipole moment of 201 D, indicated no mobility within the droplet exposed to an EF (ESI,† Fig. S7d). These results indicated a critical role of the protein dipole moment in the individual response of proteins towards EFs. In this context the dipole

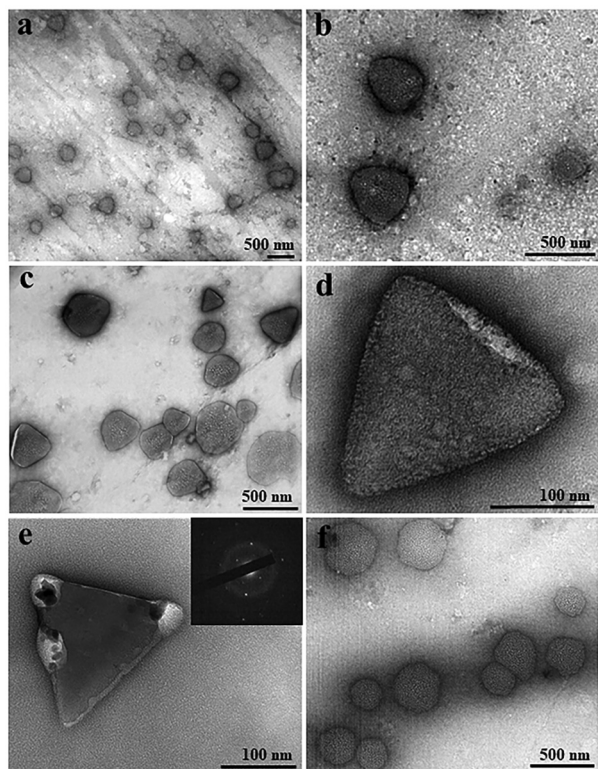


Fig. 4 Observation of LDCs of Glucose isomerase by TEM. (a–c) Triangular LDCs with round corners, (d) nucleus-like shape, and (e) crystal nucleus of GI formed under a pulsed EF with waveform 4 ( $V_{\max-500\Omega} = 20$  V) for 5 hours. The inset image in figure (e) is the corresponding electron diffraction pattern of the nucleus. (f) GI LDCs of round shape formed without treatment of EFs.





moment can be considered to be a key parameter to estimate whether EFs may influence the phase behavior of a distinct protein.

### Secondary structure analysis

Circular dichroism spectroscopy was applied to analyze the effect of EFs on the secondary structure of GI. CD spectra in the far UV region, specifically 190–260 nm, probe the secondary structure composition of proteins. Fig. 5a shows the far UV CD spectra of GI treated with different pulsed waveforms with the Pt EF setup. The negative ellipticities at 222 nm and 208 nm correspond to  $\alpha$ -helical structure and negative ellipticity at 216 nm is indicative for  $\beta$ -sheet structure. Compared to the GI spectra in the control group, without application of an EF, the decreased content of  $\alpha$ -helices and  $\beta$ -sheets was mainly promoted by waveforms 1, 2, and 4 (Fig. 5b), while waveforms 3 and 5 introduced less changes in the spectra and the secondary

structure of GI (Fig. 5a). This was probably caused by the high frequencies of waveforms 1, 2 and 4. Moreover, they contain pulses in the second half period of the waves, which were not present in waveforms 3 and 5 (ESI,† Fig. S1c). The CD spectroscopy assays supported to understand results obtained by optical microscopy showing that EFs with different waveforms can induce morphologically different GI LDCs. It also assisted to explain a behavior observed for ovalbumin that indeed did not form LDCs when applying waveforms 2, 4, and 1 using the Pt wire setup (ESI,† Fig. S3a). Further, CD spectroscopy results indicated that minor changes of the secondary structure composition are closely related to phase behavior and LDCs formation of protein.

### Perspectives

Future experiments analyzing time resolved processes of LLPS and LDCs under EFs applying particular time-resolved small angle X-ray scattering (SAXS) are planned to obtain time-resolved structural information and further insights about the process.

### Conclusions

Applying complementary optical microscopy, TEM, DLS/DDLS and CD spectroscopy, our investigations revealed distinct and innovative ways to modulate the morphology of protein LDCs and microcrystal growth by tuning or selecting distinct pulsed EFs. Five proteins were selected and different pulsed EF waveforms were applied for the experiments described. In summary, (I) pulsed EFs can change the dynamic process of protein phase separation. For example, the phase separation experiments with BPTI strongly indicate that EFs modulate the phase diagram and support BPTI to overcome the energy barrier to undergo phase separation. (II) Diverse morphological properties, *i.e.* shape, size and spatial distribution of protein LDCs and microcrystals can be obtained by tuning the frequency and amplitude of pulsed EFs. Phase-separated condensates in biological systems very often have crucial and distinct functions, as known for example for membrane-less organelles and more solid protein aggregates in neurodegenerative diseases. In this context the formation of LLPS or prevention of LLPS formation can be influenced by EFs, opening opportunities for applications of EFs in material sciences and treatment of LLPS related diseases. Particularly waveform 4 produced with the Pt EF setup supports the emergence and formation of homogeneous microcrystal suspensions, which are required for serial femtosecond X-ray crystallography diffraction data collection approaches. Waveforms 1–3 with the Pt EF setup induces a protein concentration gradient which can be used to control the crystal nucleation rate and thereby the number and dimensions of crystals to be obtained. Further, results achieved from DLS/DDLS and TEM experiments confirm a two-step crystal nucleation mechanism and demonstrate that pulsed EFs can introduce or accelerate the formation of ordered structures within LDCs. Finally, CD spectroscopy results provided evidence that the overall

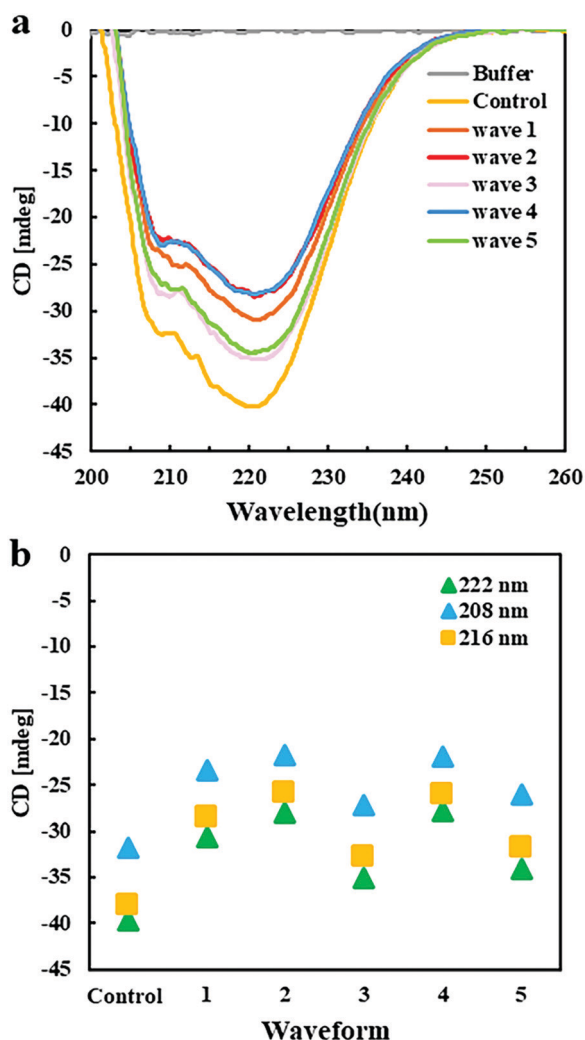


Fig. 5 (a) Far UV-CD spectra of GI after exposure to different EF waveforms ( $V_{\max-500\Omega} = 20$  V). (b) The ellipticity of GI at 208 nm (blue), 216 nm (yellow) and 222 nm (green) without EF (control), and with different EF waveforms. The negative ellipticity at 222 nm and 208 nm is indicative for  $\alpha$ -helical structure, at 216 nm represents  $\beta$ -sheet structure.



secondary structure content of proteins changes under pulsed EFs, which may in consequence affect protein–protein interactions and therefore the morphology and internal structure and order of LDCs.

## Conflicts of interest

There are no conflicts to declare.

## Acknowledgements

The authors acknowledge financial support by the Cluster of Excellence ‘Advanced Imaging of Matter’ of the Deutsche Forschungsgemeinschaft (DFG) – EXC 2056 – project ID 390715994, by the Helmholtz Excellence Network ‘Structure, Dynamics and Control on the Atomic Scale’, BMBF *via* projects 50WB1422 and 05K16GUA, by the Joachim-Herz-Stiftung Hamburg *via* the project Infecto-Physics, by the DFG – project ID BE1443/29-1, and by the China Scholarship Council – project ID [2020]71. Further, the authors acknowledge the use of the XBI biological sample preparation laboratory at European XFEL GmbH, enabled by the XBI User Consortium and would like to thank Cornelia Cazey (CSSB, Hamburg) for support in negative staining assay.

## Notes and references

- J. T. Avaro, S. L. P. Wolf, K. Hauser and D. Gebauer, *Angew. Chem., Int. Ed.*, 2020, **59**, 6155–6159.
- T. F. Whale, M. A. Holden, A. N. Kulak, Y. Y. Kim, F. C. Meldrum, H. K. Christenson and B. J. Murray, *Phys. Chem. Chem. Phys.*, 2017, **19**, 31186–31193.
- R. R. Poudyal, F. Pir Cakmak, C. D. Keating and P. C. Bevilacqua, *Biochemistry*, 2018, **57**, 2509–2519.
- M. Tena-Solsona, C. Wanzke, B. Riess, A. R. Bausch and J. Boekhoven, *Nat. Commun.*, 2018, **9**, 1–8.
- Y. Shin and C. P. Brangwynne, *Science*, 2017, **357**, 1253.
- S. Alberti, A. Gladfelter and T. Mittag, *Cell*, 2019, **176**, 419–434.
- C. N. Mudogo, S. Falke, H. Brognaro, M. Duzsenko and C. Betzel, *Traffic*, 2020, **21**, 220–230.
- L. T. Chylack, T. Tanaka and C. Ishimoto, *Science*, 1977, **197**, 1010–1012.
- V. N. Uversky, V. Davé, L. M. Iakoucheva, P. Malaney, S. J. Metallo, R. R. Pathak and A. C. Joerger, *Chem. Rev.*, 2014, **114**, 6844–6879.
- J. D. Forman-Kay, R. W. Kriwacki and G. Seydoux, *J. Mol. Biol.*, 2018, **430**, 4603–4606.
- F. Chiti and C. M. Dobson, *Annu. Rev. Biochem.*, 2006, **75**, 333–366.
- G. B. Benedek, J. I. Clark, E. N. Serrallach, C. Y. Young, L. Mengel, T. Sauke, A. Bagg and K. Benedek, *Philos. Trans. R. Soc., A*, 2006, **293**, 329–340.
- C. O. E. Ishimoto, *Proc. Natl. Acad. Sci. U. S. A.*, 1979, **76**, 4414–4416.
- S. Pagola, P. W. Stephens, D. S. Bohle, A. D. Kosar and S. K. Madsen, *Nature*, 2000, **404**, 307–310.
- E. P. Bentley, B. B. Frey and A. A. Deniz, *Chem. – Eur. J.*, 2019, **25**, 5600–5610.
- C. P. Brangwynne, P. Tompa and R. V. Pappu, *Nat. Phys.*, 2015, **11**, 899–904.
- J. Shorter, *J. Biol. Chem.*, 2019, **294**, 7113–7114.
- J. D. Forman-Kay, R. W. Kriwacki and G. Seydoux, *J. Mol. Biol.*, 2018, **430**, 4603–4606.
- M. Hofweber and D. Dormann, *J. Biol. Chem.*, 2019, **294**, 7137–7150.
- Y. H. Lin, J. D. Forman-Kay and H. S. Chan, *Biochemistry*, 2018, **57**, 2499–2508.
- H. Lu, D. Yu, A. S. Hansen, S. Ganguly, R. Liu, A. Heckert, X. Darzacq and Q. Zhou, *Nature*, 2018, **558**, 318–323.
- S. Qamar, G. Z. Wang, S. J. Randle, F. S. Ruggeri, J. A. Varela, J. Q. Lin, E. C. Phillips, A. Miyashita, D. Williams, F. Ströhl, W. Meadows, R. Ferry, V. J. Dardov, G. G. Tartaglia, L. A. Farrer, G. S. Kaminski Schierle, C. F. Kaminski, C. E. Holt, P. E. Fraser, G. Schmitt-Ulms, D. Klenerman, T. Knowles, M. Vendruscolo and P. St George-Hyslop, *Cell*, 2018, **173**, 720–734.e15.
- E. W. Martin and T. Mittag, *Biochemistry*, 2018, **57**, 2478–2487.
- J. Wang, J. M. Choi, A. S. Holehouse, H. O. Lee, X. Zhang, M. Jahnel, S. Maharana, R. Lemaitre, A. Pozniakovskiy, D. Drechsel, I. Poser, R. V. Pappu, S. Alberti and A. A. Hyman, *Cell*, 2018, **174**, 688–699.e16.
- C. Pareja-Rivera, M. Cuellar-Cruz, N. Esturau-Escofet, N. Demitri, M. Polentarutti, V. Stojanoff and A. Moreno, *Cryst. Growth Des.*, 2017, **17**, 135–145.
- G. Sasaki, A. Moreno and K. Nakajima, *J. Cryst. Growth*, 2004, **262**, 499–502.
- Z. Q. Wu, Y. M. Liu, C. Liu, J. J. Chen, L. L. Chen, T. Di Zhang, R. Bin Zhou, C. Q. Yang, P. Shang and D. C. Yin, *CrystEngComm*, 2019, **21**, 4001–4010.
- D. C. Yin, *Prog. Cryst. Growth Charact. Mater.*, 2015, **61**, 1–26.
- N. C. Das, *J. Microsc.*, 2014, **253**, 198–203.
- S. Coveney and N. Clarke, *J. Chem. Phys.*, 2012, **137**(17), 174901.
- D. J. Stewart, C. Cai, J. Nayler, T. C. Preston, J. P. Reid, U. K. Krieger, C. Marcolli and Y. H. Zhang, *J. Phys. Chem. A*, 2015, **119**, 4177–4190.
- Y. Qiu and V. Molinero, *J. Am. Chem. Soc.*, 2015, **137**, 10642–10651.
- M. M. Fard, U. K. Krieger and T. Peter, *J. Phys. Chem. A*, 2017, **121**, 9284–9296.
- D. Zhao and J. Gao, *Philos. Trans. R. Soc., A*, 2019, **377**, 20180207.
- J. C. Palmer, R. Chen and E. Lascaris, *J. Chem. Phys.*, 2017, **146**, 234503.
- W. L. Wang, Y. H. Wu, L. H. Li, W. Zhai, X. M. Zhang and B. Wei, *Sci. Rep.*, 2015, **5**, 1–10.
- M. Ganesan and M. J. Solomon, *Soft Matter*, 2017, **13**, 3768–3776.
- B. D. Smith, T. S. Mayer and C. D. Keating, *Annu. Rev. Phys. Chem.*, 2012, **63**, 241–263.



- 39 Z. Hammadi and S. Veessler, *Prog. Biophys. Mol. Biol.*, 2009, **101**, 38–44.
- 40 A. Rodríguez-Romero, N. Esturau-Escofet, C. Pareja-Rivera and A. Moreno, *Crystals*, 2017, **7**, 1–13.
- 41 D. R. Hekstra, K. I. White, M. A. Socolich, R. W. Henning, V. Šrajcar and R. Ranganathan, *Nature*, 2016, **540**, 400–405.
- 42 S. Muscat, F. Stojceski and A. Danani, *J. Mol. Graphics Modell.*, 2020, **96**, 107535.
- 43 M. Shahabi and H. Raissi, *J. Mol. Model.*, 2019, **25**, 1–8.
- 44 S. Ilieva, D. Cheshmedzhieva and T. Dudev, *Phys. Chem. Chem. Phys.*, 2019, **21**, 16198–16206.
- 45 Z. Jiang, L. You, W. Dou, T. Sun and P. Xu, *Polymers*, 2019, **11**(2), 282.
- 46 X. Wang, Y. Li, X. He, S. Chen and J. Z. H. Zhang, *J. Phys. Chem. A*, 2014, **118**, 8942–8952.
- 47 A. Singh, S. Munshi and V. Raghavan, *Proteomes*, 2013, **1**, 25–39.
- 48 M. Imani, S. Kazemi, M. Saviz, L. Farahmand, B. Sadeghi and R. Faraji, *Bioelectromagnetics*, 2019, **40**(6), 375–390.
- 49 A. Baldan, *J. Mater. Sci.*, 2002, **37**, 2171–2202.
- 50 S. Grouazel, J. Perez, J. P. Astier, F. Bonneté and S. Veessler, *Acta Crystallogr., Sect. D: Biol. Crystallogr.*, 2002, **58**, 1560–1563.
- 51 R. Schubert, A. Meyer, K. Dierks, S. Kapis, R. Reimer, H. Einspahr, M. Perbandt and C. Betzel, *J. Appl. Crystallogr.*, 2015, **48**, 1476–1484.
- 52 S. Falke and C. Betzel, *Radiation in Bioanalysis*, 2019, pp. 173–193.
- 53 H. Brognaro, S. Falke, C. N. Mudogo and C. Betzel, *Crystals*, 2019, **9**, 620.
- 54 P. G. Vekilov, *Cryst. Growth Des.*, 2004, **4**, 671–685.
- 55 J. Berry, C. P. Brangwynne and M. Haataja, *Rep. Prog. Phys.*, 2018, **81**(4), 046601.
- 56 I. M. Lifshitz and V. V. Slezov, *Sov. Phys. JETP*, 1958, **35**, 479–492.



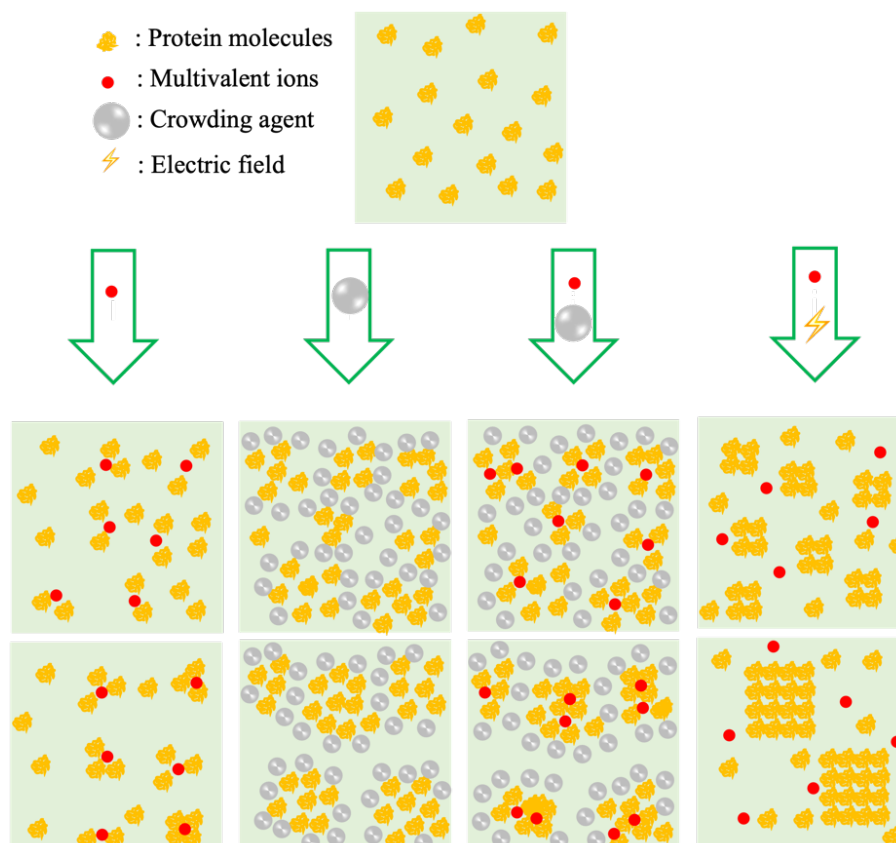




## 5.2 Exploring nucleation pathways in distinct physicochemical environments unveiling novel options to modulate and optimize protein crystallization

### Summary



Based on the screening results shown in publication 1, the modulating effect of pEFs on protein phase separation was investigated further in detail within the pathway of protein crystallization, applying distinct ionic strengths and crowding agent conditions. GI was used first to study systematically the influence of pEFs on the growth kinetics and formation mechanisms of mesoscopic protein clusters in a number of physicochemical conditions. The role of protein mesoscopic ordered clusters (MOCs) in the crystallization pathway was uncovered by adding pEF-induced MOCs to fresh crystallization droplets. The protein complex Pdx of *S. aureus*, composed of twenty-four protein monomers, was employed finally to validate the effectiveness of pEF modulating the kinetics and mechanisms of protein clustering and to confirm the role of MOCs in overcoming the energy barrier of nucleation and improving protein crystallization. In conclusion, multiple phase separation and nucleation mechanisms were observed applying the DLS/DDLS technique after tuning the proportion of specific and nonspecific protein interactions by varying the ionic strength, crowding agent, and pEF parameters in the protein solutions.



**Graphic abstract.** Illustrations of a protein nucleation model under influence of different physicochemical factors.<sup>143</sup> Four different channels from the left to the right side represent a schematic protein nucleation process, including clustering and ordering, driven by multivalent ions alone, crowding agent only, both multivalent ions and crowding agent, and multivalent ions applying an EF, respectively.

## Article

# Exploring Nucleation Pathways in Distinct Physicochemical Environments Unveiling Novel Options to Modulate and Optimize Protein Crystallization

Mengying Wang <sup>1,†</sup>, Angélica Luana C. Barra <sup>1,2,†</sup> , Hévila Brognaro <sup>1</sup> and Christian Betzel <sup>1,\*</sup> 

- <sup>1</sup> Laboratory for Structural Biology of Infection and Inflammation, Institute of Biochemistry and Molecular Biology, University of Hamburg, Notkestrasse 85, c/o DESY, Build. 22a, 22603 Hamburg, Germany; mengying.wang@chemie.uni-hamburg.de (M.W.); angelica.barra@usp.br (A.L.C.B.); hbrognao@yahoo.com.br (H.B.)
- <sup>2</sup> Pólo TerRa, São Carlos Institute of Physics, University of São Paulo, Av. João Dagnone, 1100, Jd. Santa Angelina, São Carlos 13563-120, SP, Brazil
- \* Correspondence: christian.betzel@uni-hamburg.de
- † These authors contributed equally to this work.

**Abstract:** The scientific discussion about classical and nonclassical nucleation theories has lasted for two decades so far. Recently, multiple nucleation pathways and the occurrence and role of metastable intermediates in crystallization processes have attracted increasing attention, following the discovery of functional phase separation, which is now under investigation in different fields of cellular life sciences, providing interesting and novel aspects for conventional crystallization experiments. In this context, more systematic investigations need to be carried out to extend the current knowledge about nucleation processes. In terms of the data we present, a well-studied model protein, glucose isomerase (GI), was employed first to investigate systematically the early stages of the crystallization process, covering condensing and prenucleation ordering of protein molecules in diverse scenarios, including varying ionic and crowding agent conditions, as well as the application of a pulsed electric field (pEF). The main method used to characterize the early events of nucleation was synchronized polarized and depolarized dynamic light scattering (DLS/DDLS), which is capable of collecting the polarized and depolarized component of scattered light from a sample suspension in parallel, thus monitoring the time-resolved evolution of the condensation and geometrical ordering of proteins at the early stages of nucleation. A diffusion interaction parameter,  $K_D$ , of GI under varying salt conditions was evaluated to discuss how the proportion of specific and non-specific protein–protein interactions affects the nucleation process. The effect of mesoscopic ordered clusters (MOCs) on protein crystallization was explored further by adding different ratios of MOCs induced by a pEF to fresh GI droplets in solution with different PEG concentrations. To emphasize and complement the data and results obtained with GI, a recombinant pyridoxal 5-phosphate (vitamin B6) synthase (Pdx) complex of *Staphylococcus aureus* assembled from twelve monomers of Pdx1 and twelve monomers of Pdx2 was employed to validate the ability of the pEF influencing the nucleation of complex macromolecules and the effect of MOCs on adjusting the crystallization pathway. In summary, our data revealed multiple nucleation pathways by tuning the proportion of specific and non-specific protein interactions, or by utilizing a pEF which turned out to be efficient to accelerate the nucleation process. Finally, a novel and reproducible experimental strategy, which can adjust and facilitate a crystallization process by pEF-induced MOCs, was summarized and reported for the first time.

**Keywords:** phase transition; multiple nucleation pathways; mesoscopic ordered clusters; pulsed electric field; dynamic light scattering; depolarized dynamic light scattering



**Citation:** Wang, M.; Barra, A.L.C.; Brognaro, H.; Betzel, C. Exploring Nucleation Pathways in Distinct Physicochemical Environments Unveiling Novel Options to Modulate and Optimize Protein Crystallization. *Crystals* **2022**, *12*, 437. <https://doi.org/10.3390/cryst12030437>

Academic Editors: Fajun Zhang, José Gavira, Geun Woo Lee and Dirk Zahn

Received: 1 March 2022

Accepted: 17 March 2022

Published: 21 March 2022

**Publisher's Note:** MDPI stays neutral with regard to jurisdictional claims in published maps and institutional affiliations.



**Copyright:** © 2022 by the authors. Licensee MDPI, Basel, Switzerland. This article is an open access article distributed under the terms and conditions of the Creative Commons Attribution (CC BY) license (<https://creativecommons.org/licenses/by/4.0/>).

## 1. Introduction

Regardless of the establishment of the nucleation theory for approximately a hundred years [1], the discussion between classical and nonclassical nucleation theories is still an

ongoing topic in the field of crystallogenesi s [2–12]. The most important characteristic of the classical nucleation theory (CNT) assumes a one-step nucleation of solute molecules directly from the supersaturated bulk solution, along with the simultaneous increase in two ordering parameters—concentration and structural arrangements guiding the three-dimensional (3D) ordering of a protein crystal [13]. However, proposed simulations have decoupled the development of the two ordering parameters leading towards a multi-step nucleation [14], termed as nonclassical nucleation theory (NCNT), which was supported subsequently by experimental discoveries [15–18]. In particular, the two-step nucleation theory has recently been receiving more attention since widespread observations of functional liquid-liquid phase separation (LLPS), part of the two-step nucleation process, were published in cellular biology, in the crystallization of inorganic [19–23] and organic particle system [24–27], and in the in vivo formation of crystals and fibers, which can also be involved in diseases [28–31]. According to the two-step nucleation theory, the homogeneous solution undergoes LLPS and firstly forms a liquid dense phase without internal order, after which the molecules within this liquid dense phase can rearrange to form nuclei [32,33]. This liquid dense phase is classified as a metastable intermediate, as its free energy level is lower than in the initial homogeneous solution, but higher than in the following crystalline phase [34]. By analyzing the impact of mesoscopic clusters in protein solutions in the context of the observed nucleation rate, Mike Sleutel and Alexander E. S. Van Driessche demonstrated that mesoscopic clusters can enhance the crystallization rate 10-fold for lysozyme and 100-fold for glucose isomerase [35]. With the recent options of time-resolved imaging at a molecular resolution, direct evidence of nucleation through multiple pathways was uncovered. For example, Houben et al. recorded utilizing Cryo-STEM tomography the formation of disordered ferritin aggregates, followed by a desolvation process which leads to a jointly continuous increase in density and order from the surface towards the center of aggregates [36]. This observed phenomenon is already beyond the original explanation of either CNT or NCNT. Van Driessche et al. observed, by means of Cryo-EM, the early nucleation events of GI with varying precipitants, showing no occurrence of liquid dense intermediates as a precursor of crystal nuclei, but driven by the oriented attachment of nanosized and ordered ‘building blocks’ emerged directly from the protein solution [7]. They revealed further the interplay between the earliest formed crystalline nano-assemblies and their effect of oriented attachment upon the nucleation process [37]. On the other hand, and complementarily, the group of Fajun reported the effect of multivalent ions capable of tuning protein interactions [38–41], and reviewed the interplay of specific and nonspecific interactions influencing the nucleation pathway which can contain metastable intermediate phases [9]. In this context, more comprehensive crystallization scenarios remain to be explored in more detail, applying complementary bioanalytical techniques to obtain more insights about the crystal nucleation pathways.

Here, we employed a well-studied model protein glucose isomerase (GI, 43.23 kDa) from *Streptomyces rubiginosus* to investigate systematically: (1) the early stages of protein phase transition and crystallization in a wide range of physicochemical scenarios, including varying salt conditions, crowding agent polyethylene glycol (PEG) and applying a pulsed electric field (pEF); (2) the mediating effect of mesoscopic ordered clusters (MOCs), which mostly have a dimension range of 10 to 1000 nm [42], induced by pEF on the crystallization process. Furthermore, a more challenging and complex biomacromolecular system, the pyridoxal 5-phosphate (vitamin B6) synthase (Pdx) complex of *Staphylococcus aureus*, was employed to verify the universal effect of pEFs and to verify the effect of MOCs on the crystallization process. The Pdx complex, as shown in Figure 1b, is formed by a dodecameric assembling of Pdx1 (32.12 kDa) attached to twelve monomers of Pdx2 (23.76 kDa) via a dynamic and transient complex formation that causes the crystallization to be most challenging for obtaining X-ray-suitable crystals [43]. To date, three-dimensional X-ray structures of Pdx complexes from four different organisms, but not *S. aureus*, have been reported and deposited in the protein data bank. Strohmeier and co-workers found that the H170N (H165N in Pdx2 from *S. aureus*) mutation in the catalytic site of Pdx2 from

*Bacillus subtilis* stabilizes the complex in a fully saturated form, enabling and supporting crystallization and structural analysis [44]. Therefore, in our investigations, we also applied the Pdx2 mutant of *S. aureus* to prepare a Pdx1/Pdx2<sub>H165N</sub> (Pdx) complex for the experiments performed.

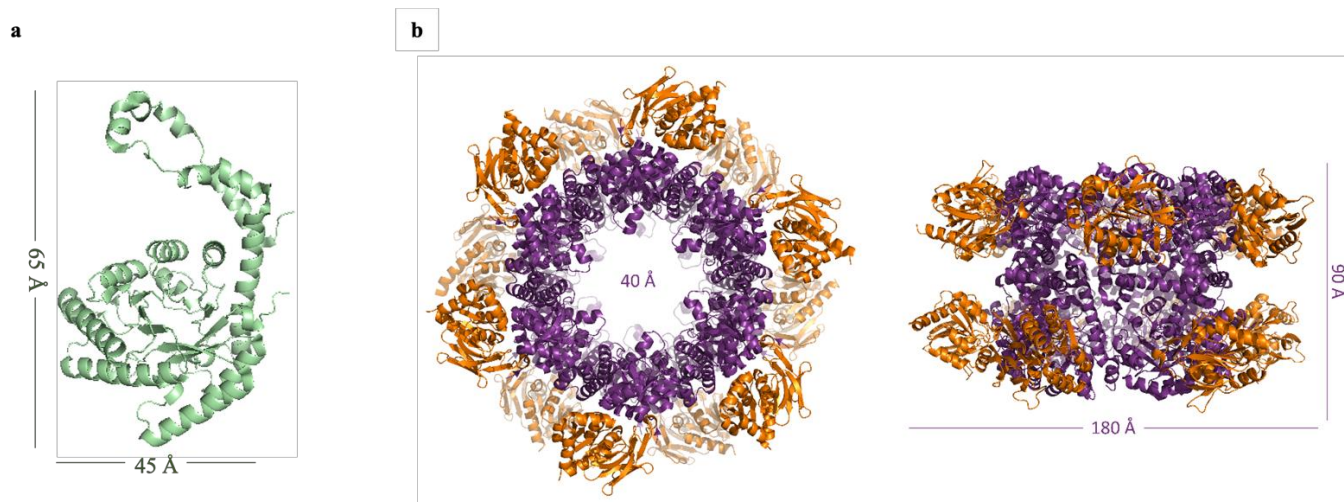


**Figure 1.** (a) The structure of monomeric glucose isomerase from *Streptomyces rubiginosus* (PDB: 4ZB2) [45]. (b) The Pdx1–Pdx2 complex from the homologue *Bacillus subtilis* (PDB: 2NV2) shown in two orientations rotated by 90°. Twelve Pdx1 synthase subunits form a double hexameric ring core (purple), to which twelve Pdx2 glutaminase subunits (orange) are attached [44].

The main technique utilized in this work is non-invasive depolarized dynamic light scattering (DDLS) [46–50], which employs the birefringent optical property of crystalline materials to detect the early and nanoscale formation of nuclei not detectable via optical microscopes. The scattered DDLS signal intensity therefore rises with the ordering of a 3D structure in a solution exposed to laser light. Meanwhile, the polarized component of scattered light is collected by a separate detector as a conventional DLS signal, whose intensity depends only on particle dimension and density in solution. Hence, synchronously monitoring DLS and DDLS signal intensities allows us to identify and investigate the early-stage evolution of a crystal nucleation process time-resolved under different physicochemical conditions following both detected signals and corresponding derived parameters—condensing and ordering. In addition, we measured the diffusion interaction parameter  $K_D$ , applying a different hardware system, to investigate the influence of different salt conditions to non-specific protein–protein interactions and to the resulting phase behaviors. Our results confirm the coexistence of different nucleation pathways by tuning the proportion of specific and non-specific protein–protein interactions and by introducing an external force–pulsed electric field. The application of pEF and the addition of pre-grown mesoscopic ordered clusters proved for both proteins applied in these investigations to be effective methods to support and improve protein nucleation towards obtaining X-ray suitable crystals.

## 2. Materials and Methods

The homotetrameric glucose isomerase (GI) from *Streptomyces rubiginosus* (Hampton Research, Aliso Viejo, CA, USA), with an isoelectric point of 5.0 and molecular weight of 43.23 kDa, was stabilized in 10 mM MES buffer, pH 6.5 with 1 mM dithiothreitol (DTT). The Pdx complex from *Staphylococcus aureus*, composed of twelve Pdx1 (32.12 kDa) and twelve Pdx2<sub>H165N</sub> (23.76 kDa) subunits, with an isoelectric point of 5.26, was expressed and purified as reported before [51] and stored in 20 mM Tris-HCl buffer, pH 8, 200 mM NaCl, 1 mM ethylenediaminetetraacetic acid (EDTA), 2 mM DTT and 10 mM L-glutamine. All the stock solutions of precipitants and salts applied were prepared in the same buffer with the corresponding proteins and filtered prior to use, applying either a 0.2  $\mu\text{m}$  or a 0.45  $\mu\text{m}$



filter (SARSTEDT, Nümbrecht, Germany). Prior to experiments, GI and the Pdx complex were centrifuged for 30 min at  $21,130\times g$  and  $4\text{ }^{\circ}\text{C}$  and the protein concentrations were determined applying a Nanodrop 2000 (Thermo Fisher Scientific, Bremen, Germany). All measurements were carried out at  $20\text{ }^{\circ}\text{C}$ .

## 2.1. Polarized and Depolarized Dynamic Light Scattering (DLS/DDLS) Experiments

### 2.1.1. DDLS Instrument and Setup for Applying Pulsed Electric Field

As shown in Figure 2a,b, one custom-built light scattering instrument, which is capable of detecting simultaneously the vertical component (polarized) and horizontal component (depolarized) of scattered light from the sample, was designed and constructed in collaboration with XtalConcepts (Hamburg, Germany). The instrument provides a laser wavelength of 532 nm and a laser output power of 100 mW. The laser light was polarized by a vertical polarizer before passing through the sample. The vertical component of scattered light (DLS signal) was collected directly at  $90^{\circ}$  by an objective (Plan APO ELWD  $20\times 0.42$  WD = 20), and the horizontal component was separated from scattered light by a polarizing beam splitter (Qioptic Photonics, Göttingen, Germany) and collected as a DDLS signal. The autocorrelators of the instrument cover an acquisition time range from 0.4 ms to 30 s. A transparent quartz cuvette (101.015-QS, Hellma Analytics, Munich, Germany), with  $3\text{ mm}\times 3\text{ mm}$  inner cross-section and 21 mm height, was used as the sample container and immersed into an index matching bath with plane parallel walls (thickness 1 mm) and filled with ultrapure water. The design and setup for applying pEF to a sample suspension in the cuvette during DLS/DDLS measurements is shown in Figure 2c and was described in detail in a previous publication [52]. Two platinum (Pt) wires with 0.3 mm diameter, 25 mm length and a resistance (R) of approx.  $37.5\text{ m}\Omega$  at  $20\text{ }^{\circ}\text{C}$  (Sigma, Neustadt, Germany) were inserted at two opposite corners of the cuvette to generate a pEF. The applied pulsed waveform is with a pulse amplitude rising continuously in the first half period and decreasing gradually in the second half period of one waveform circle (Figure 2c), which was referred to waveform 4 (W4) in our previous publication. The maximum output pulse amplitude in each wave circle was 30 V and the minimum was no larger than 1 V on  $500\text{ }\Omega$  load. The pulse width ( $\tau$ ) of each single pulse was  $0.6\pm 0.15\text{ ms}$ .

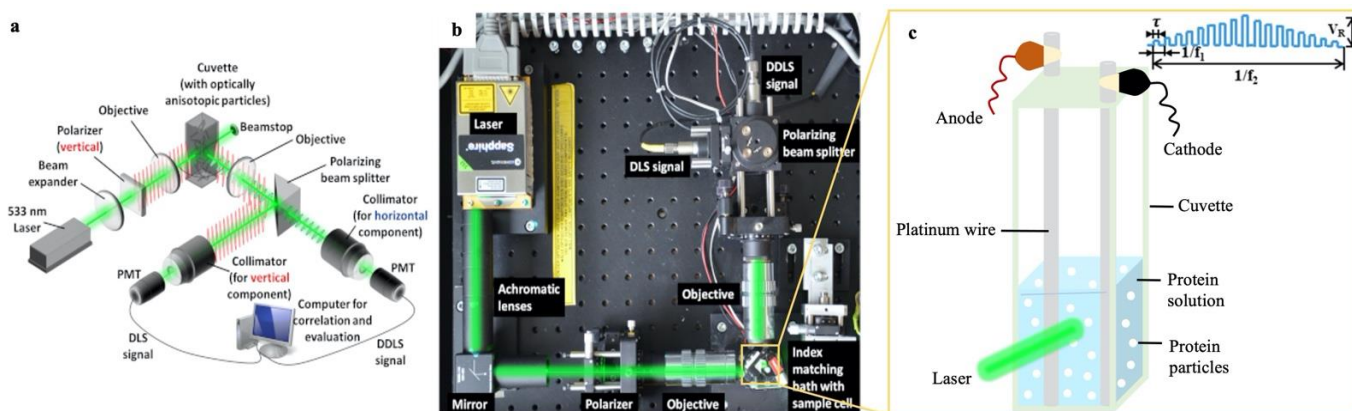


**Figure 2.** (a) Schematic [53] and (b) photographic [52] images of the DDLS instrument. (c) Illustration of the quartz cuvette with two Pt wires to apply a pulsed electric field during a DLS/DDLS measurement [52].

### 2.1.2. Sample Preparation and Experimental Methods for DLS/DDLS Measurements

Prior to DLS/DDLS measurements, the stock solutions of protein, salt and crowding agent were mixed according to the final concentration of each composite in the mixture with a final volume of  $40\text{ }\mu\text{L}$ . The measured solutions were pipetted into the transparent quartz cuvette and sealed with a glass cover slid. To investigate the effect of a pEF on protein crystallization (Sections 3.3 and 3.4), the pEF described in Section 2.1.1 and Figure 2c was applied to GI and Pdx samples of pEF groups continuously during the entire DDLS mea-

surement. For GI, each data acquisition step was recorded for 20 s followed by a delay time of 20 s for a DLS/DDLS measurement of 1 h. For the Pdx complex, each measurement was recorded for 4 h with 20 s of acquisition time for each data point and 60 s of interval delay time between two data points. The decay time constants of the DLS signal (translational diffusion coefficient,  $D_t$ ) and the DDLS signal (rotational diffusion coefficient,  $D_r$ ) are obtained from the autocorrelation function (ACF) by using the CONTIN algorithm [54]. Appropriate viscosity of each solution was considered to calculate the hydrodynamic radii ( $R_h$ ) based on the well-known Stokes–Einstein equation [55] (Equation (1)) and Stokes–Einstein–Debye equation [56] (Equation (2)):

$$D_t = \frac{K_B T}{6\pi\eta R_h} \quad (1)$$

$$D_r = \frac{K_B T}{8\pi\eta R_h^3} \quad (2)$$

where  $D_t$  and  $D_r$  are the translational and rotational diffusion coefficients derived from the ACF of the DLS and the DDLS signal as a function of time, respectively.  $K_B$  is the Boltzmann coefficient,  $T$  is the absolute temperature and  $\eta$  is the viscosity value of the solution.

## 2.2. Measuring Diffusion Interaction Parameter— $K_D$

To obtain information about the protein diffusion interaction parameter  $K_D$ , a Wyatt Mobius instrument was applied (Wyatt Technology, Santa Barbara, CA, USA), which is a non-destructive and versatile light scattering instrument applied to measure particle dimensions and electrophoretic mobility of proteins/polymers. The translational diffusion coefficient  $D_t$  determined by DLS is a function of concentration  $c$  as shown in Equation (3) [57], from which the  $K_D$  value was calculated:

$$D_t = D_0 (1 + K_D c) \quad (3)$$

where  $D_t$  is the measured transitional diffusion coefficient,  $D_0$  is the diffusion coefficient at infinite dilution, and  $c$  is the concentration of the protein in mg/mL,  $K_D$  is the first-order diffusion interaction parameter, which is fundamentally related to the common indicator of protein–protein interactions—the second virial coefficient  $A_2$  [58]:

$$K_D = 1.024A_2M - 6.18 \quad (4)$$

where  $M$  is the protein molecular weight.

For the determination of the  $K_D$  values, six concentrations of the GI solution ranging from 1 to 20 mg/mL were applied and for the Pdx complex six solutions in the range of 0.5 to 5 mg/mL were prepared and measured. Before preparing the sample suspensions the concentrations of the stock protein solutions were measured after centrifugating them for 30 min at  $21,130\times g$  and  $4^\circ\text{C}$ . Buffers were filtered, applying  $0.2\ \mu\text{m}$  filters. Then,  $45\ \mu\text{L}$  of the protein sample solution was pipetted into a quartz cuvette (WNQC45-00, Wyatt Technology, Santa Barbara, CA, USA) and recorded by DLS. The corresponding  $K_D$  values were calculated and analyzed by applying the software DYNAMICS [57].

## 2.3. Hanging-Drop Crystallization of Protein with Mesoscopic Ordered Clusters (MOCs) Induced by pEF

### 2.3.1. Glucose Isomerase

A  $40\ \mu\text{L}$  solution of 4 mg/mL GI in 10 mM MES pH 6.5, 1 mM DTT and 50 mM  $\text{MgCl}_2$  buffer was exposed to a pEF (parameters described in Section 2.1.1) for 30 min (Figure 3, Step 1). After, the pEF-treated protein solution containing MOCs was mixed on one cover slide with 4 mg/mL fresh protein solution in five different volume ratios to form a  $2\ \mu\text{L}$  protein droplet in total (Figure 3, Step 2). Finally, protein droplets on four cover slides were mixed with PEG20k in a 1:1 volume ratio (Figure 3, Step 3). Four concentrations of PEG20k (2%, 4%, 8% and 12%) were applied to droplets on different cover slides. Then,

500  $\mu\text{L}$  of PEG20k at the same initial concentration as prepared for the 5 droplets on each slide was added to the reservoir of the hanging-drop 24-well crystallization plate (Jena Bioscience, Jena, Germany), and afterwards each cover slide with 5 droplets was turned over on individual crystallization reservoirs and sealed with silicone grease (Kurt Obermeier, Bad Berleburg, Germany). All experiments were performed in quadruplicate. The crystallization plates were placed at 20  $^{\circ}\text{C}$  and observed applying an OLYMPUS SZX12 Microscope (OLYMPUS, Tokyo, Japan).

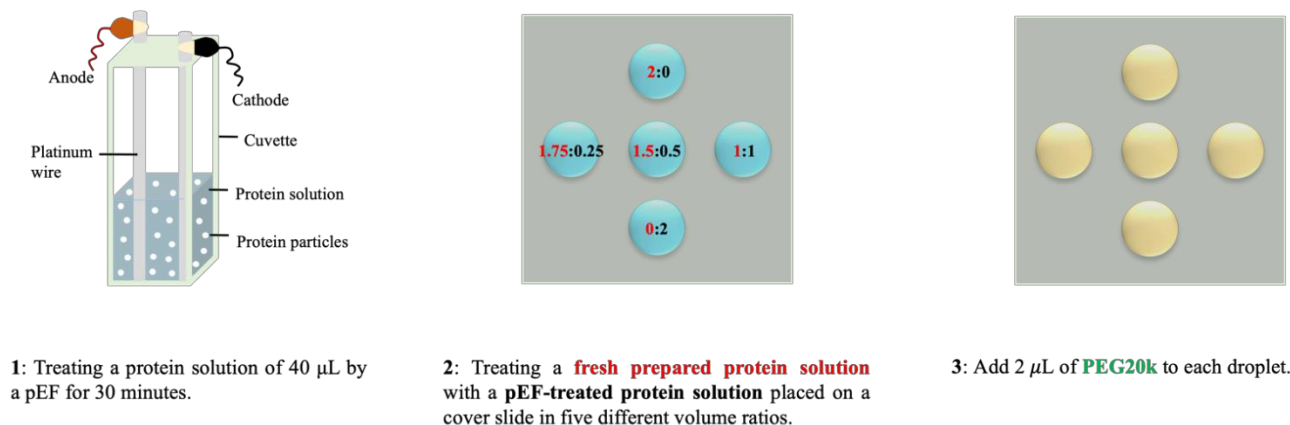


**Figure 3.** Scheme showing the three-step experimental procedure to prepare hanging-drop crystallization droplets of GI with varying volume ratios of mesoscopic ordered clusters, prior prepared by treating a protein solution with a pEF.

### 2.3.2. Pdx Complex

A 40  $\mu\text{L}$  solution of the Pdx complex at 5 mg/mL was mixed 1:1 with 10% PEG4K, 0.2 M ammonium citrate pH 7.0, 10 mM L-Glutamine and treated with pEF (parameters described before in Section 2.1.1) for 4 h as shown in step 1 of Figure 3. Afterwards, 0.5  $\mu\text{L}$  of the pEF-treated protein solution containing mesoscopic ordered clusters was taken from the cuvette and mixed on a cover slide with 2  $\mu\text{L}$  of 5 mg/mL of fresh Pdx solution to reach a final volume of 2.5  $\mu\text{L}$ . Subsequently, 0.5  $\mu\text{L}$  of 20% PEG4K was added to the droplet. For control, a 3  $\mu\text{L}$  droplet was prepared and placed on a glass cover slide without pEF-treated protein solution but containing the same final concentration of Pdx and PEG4K. All experiments were prepared in quadruplicates. Each cover slide was turned over on one crystallization reservoir of the hanging-drop 24-well plate (Jena Bioscience, Jena, Germany) containing 500  $\mu\text{L}$  of 20% PEG4K as the reservoir mother liquor and sealed with silicone grease (Kurt Obermeier, Bad Berleburg, Germany). The crystallization plate incubation and further analysis of droplets were carried as described for GI previously.

## 3. Results

### 3.1. Effect of the Metal Cations $\text{Na}^+$ and $\text{Mg}^{2+}$ on Early Stage Condensing and Prenucleation Ordering of GI

To investigate GI prenucleation under the effect of different ions and ionic strength conditions, a GI solution at 2 mg/mL was mixed with 4% PEG20k acting as crowding agent in final concentration (Figure 4). The hydrodynamic radius ( $R_h$ ) of tetrameric and negatively charged GI was stable during the 1-hour measurement and showed a value of approx. 3 nm (Figure 4a1), which is smaller than the reported tetrameric  $R_h$  of 4.4–5.0 nm [59–61], due to the hyper-diffusivity of proteins caused by the relative high repelling strength between proteins in solution at low concentrations of ions [57]. A slight fluctuation of GI  $R_h$  appeared after adding 20 mM NaCl (Figure 4a2); however, only NaCl at concentrations higher than 60 mM triggered the formation of nanoscale clusters with  $R_h$  of approx. 9 nm, which transformed along an increasing NaCl gradient towards mesoscopic clusters with initial dimensions of approx. 100 nm (Figure 4a3–a5). Clusters with larger dimensions as well



an increasing clusters density were acquired applying 250 mM of NaCl, as demonstrated by the increase in the DLS signal intensity, although nonstructural ordering was detected according to the negligible increase in DDLS signal intensity within 1 h of measurement (Figure 4a5').

The results shown in Figure 4b,b' were obtained by adding different concentrations of MgCl<sub>2</sub> into the mixtures of 2 mg/mL GI containing 4% PEG20k. The concentration of MgCl<sub>2</sub> was selected based on the aim to keep the concentrations of chloride ions and cationic net valency the same as in the NaCl+GI assays (Figure 4a,a'). Compared with the effect of NaCl, even 10 mM MgCl<sub>2</sub> induced the formation of nanoscale clusters with approx.  $R_h$  of 9 nm and mesoscopic clusters with radius of approx. 300–400 nm (Figure 4b2), accompanied by a strong increase in DLS signal intensity (Figure 4b2'). Interestingly, a synchronous rise in DDLS signal intensity showing changes in structural order also occurred at MgCl<sub>2</sub> concentrations higher than 30 mM (Figure 4b', 30–125 mM MgCl<sub>2</sub>), indicating the simultaneous evolution of structural ordering within condensing GI particles in solutions.

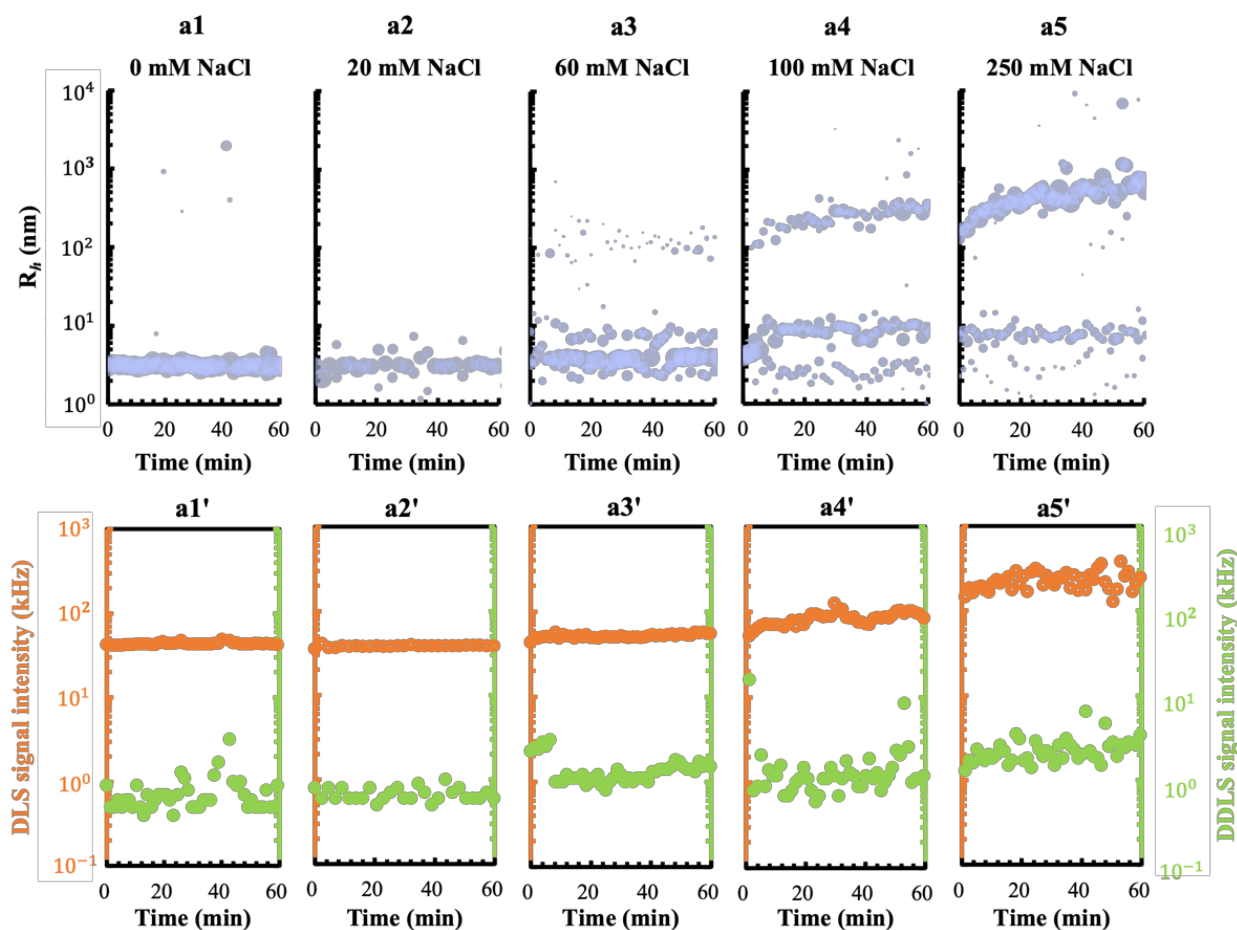
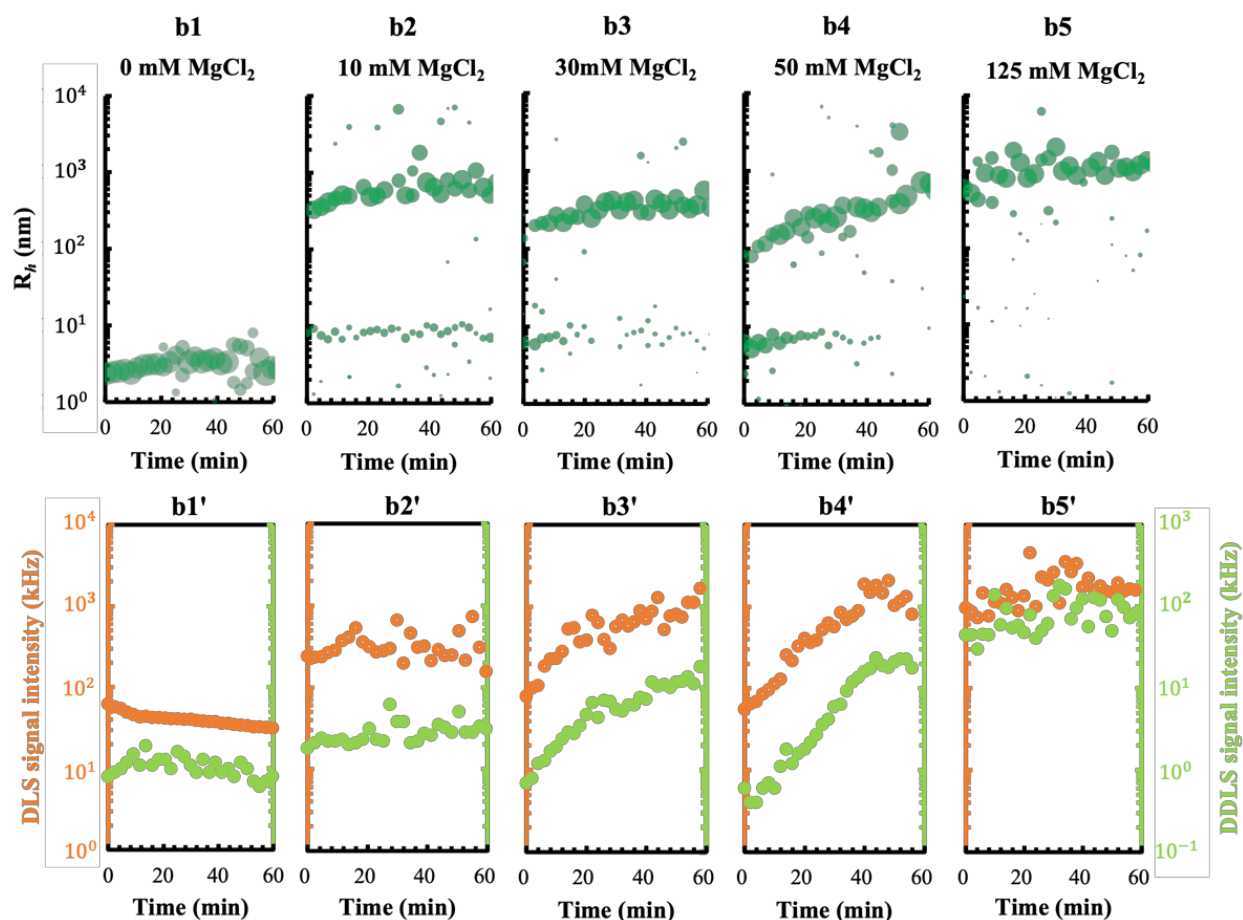


Figure 4. Cont.



**Figure 4.** Monitoring phase transition of a 2 mg/mL GI solution by DLS and DDLS under the effect of  $\text{Na}^+$  and  $\text{Mg}^{2+}$  gradients in 10 mM MES pH 6.5 and 4% PEG20k buffer. (a1–a5) Kinetic evolution of the hydrodynamic radius in the presence of a NaCl gradient (a1'–a5') showing the resultant DLS (left Y-axis, orange open circles) and DDLS (right Y-axis, green closed circles) signal intensities. (b1–b5) Kinetic evolution of the hydrodynamic radius and (b1'–b5') corresponding DLS/DDLS signal intensities of a GI solution by mixing the solution with a  $\text{MgCl}_2$  gradient.

To explore the mechanisms caused by the  $\text{NaCl}$  and  $\text{MgCl}_2$  ions on the GI phase behaviors shown above, the diffusion interaction parameter  $K_D$  of GI solutions in the corresponding gradients of  $\text{NaCl}$  (Figure 5c) and  $\text{MgCl}_2$  (Figure 5d) was measured subsequently. As an indicator of non-specific protein–protein interactions, positive  $K_D$  values indicate repulsive intermolecular interactions, while negative values denote attractive interactions. The decreased  $K_D$  value in Figure 5c (black crosses) demonstrated that an increasing  $\text{NaCl}$  concentration diminished the repulsive forces between negatively charged GI particles in solution. However, the divalent cation  $\text{Mg}^{2+}$  caused even stronger effects and obviously promoted more intermolecular interactions between GI molecules, and the  $K_D$  values of GI were reduced more sharply in the concentration range of 0 to 50 mM  $\text{Mg}^{2+}$  (black crosses in Figure 5d) compared to those of  $\text{Na}^+$  ions in the concentration range of 0 to 100 mM (black crosses in Figure 5c). The positive  $K_D$  values of GI at  $\text{MgCl}_2$  concentrations above 50 mM are higher than those of GI with  $\text{MgCl}_2$  at concentrations below 50 mM. In parallel, polydisperse  $R_h$  values indicate the formation of aggregates at  $\text{MgCl}_2$  concentrations higher than 50 mM (red dots in Figure 5d), which were also accompanied by the presence of multiple decay steps of the corresponding ACF, as shown in Figure 5b. Therefore, the obtained  $K_D$  values of GI in the presence of  $\text{MgCl}_2$  at concentrations above 50 mM probably do not reveal the real situation of protein interactions. These results correlate with the order of cations in the Hofmeister series— $\text{Na}^+$  is in a higher order in the cation series than

$Mg^{2+}$  to enhance the ‘salting in’ effect and the solubility of protein at lower ionic strengths, while the ‘salting out’ effect appeared and caused the aggregation of the protein at a high concentration of  $Mg^{2+}$  [62]. It is worth pointing out that the subtle decline in GI  $R_h$  with decreasing concentrations of 100 to 0 mM NaCl (red dots in Figure 5c) and 50 to 0 mM  $MgCl_2$  (red dots in Figure 5d) can be considered as a result of the hyper-diffusivity of the protein at low ionic strength, which is used to calculate  $R_h$  based on Equation (1).

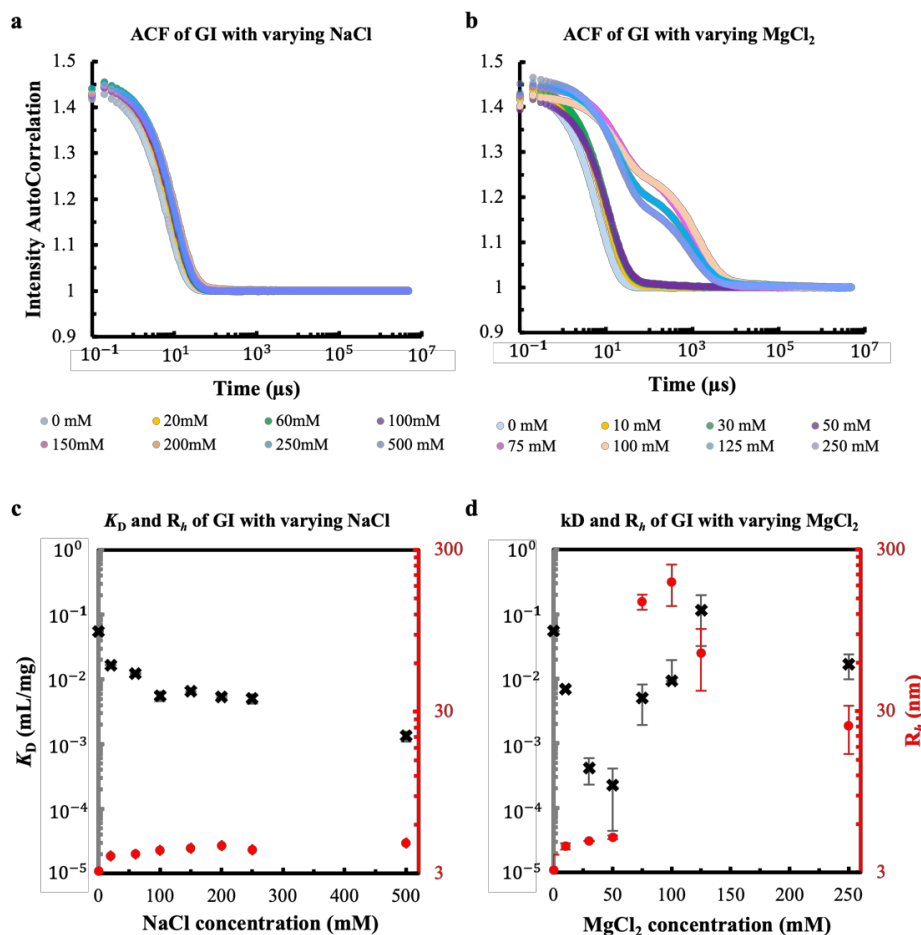


**Figure 5.** The auto-correlation function of a GI solution (a) with varying NaCl and (b) with varying  $MgCl_2$ .  $K_D$  values (left Y-axis, black cross) and the hydrodynamic radii ( $R_h$ , right Y-axis, red dot) of GI as a function of (c) NaCl and (d)  $MgCl_2$  concentration.

### 3.2. Effect of a Crowding Agent on Condensing and Prenucleation Ordering of GI

In a crowded environment, proteins are subjected to an entropic penalty if they form a large co-volume with impenetrable crowders, which occupy the solvent space and reduce the volume accessible to the protein [63]. How does volume exclusion affect the protein nucleation considering condensing and ordering? Here, we tried to answer this question by monitoring the phase behaviors of GI mixed with varying concentrations of PEG20k applying DLS/DDLS. Based on the results shown in Figures 4 and 5, the 10 mM MES pH 6.5, 1 mM DTT buffer was prepared by (i) adding 100 mM NaCl and (ii) adding 50 mM  $MgCl_2$  to investigate the effect of varying PEG20k concentrations on GI phase behavior in different ionic systems. It is very noticeable, as shown in Figure 6a, that the condensation of GI in solutions with 100 mM NaCl was promoted gradually with the rise in PEG20k concentration from 0 to 6%, but no obvious structural ordering was detected as the DDLS signal intensities remained lower than 5 kHz, as shown in Figure 6a'. ]vspace-6pt

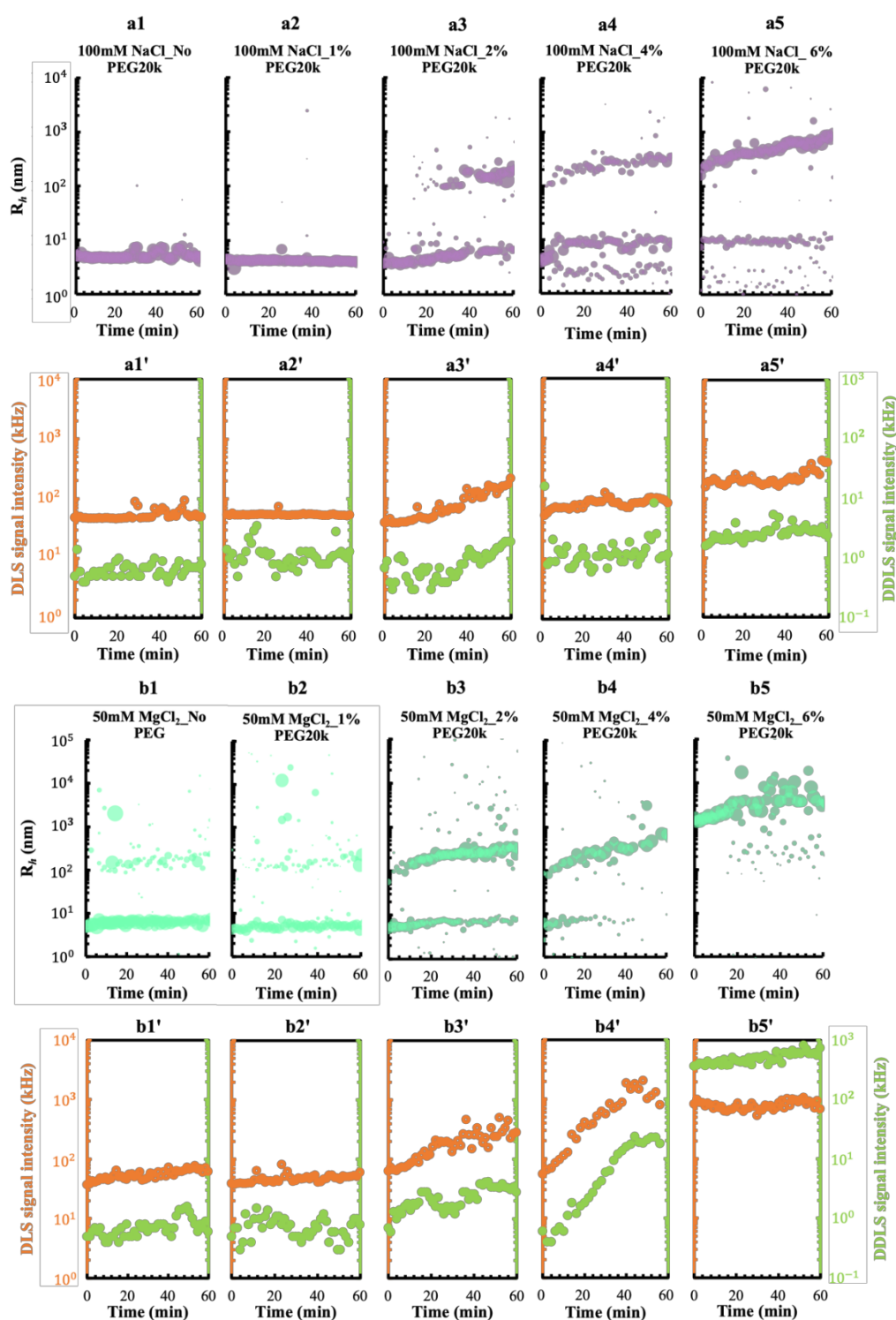


**Figure 6.** Time-resolved monitoring of GI phase transition in context of varying crowding environments. (a1–a5) Kinetic evolution of the hydrodynamic radii and (a1'–a5') corresponding DLS (left Y-axis, orange symbol)/DDLS (right Y-axis, green symbol) signal intensities of a 2 mg/mL GI solution mixed with a gradient of PEG20k in a buffer containing 100 mM NaCl. (b1–b5) Kinetic evolution of the hydrodynamic radii and (b1'–b5') corresponding DLS/DDLS signal intensities of a 2 mg/mL GI solution mixed with a gradient of PEG20k in a buffer containing 50 mM MgCl<sub>2</sub>.

However, evident structural ordering was observed in parallel with GI condensing under the effect of 4% and 6% PEG20k in the presence of 50 mM MgCl<sub>2</sub> (Figure 6b4,b4' and b5,b5').

The highest DDLS intensities of approx. 360 kHz were detected from the beginning onwards after mixing GI with 6% PEG20K, indicating a simultaneous trigger of condensing and structural ordering within the GI particles. Furthermore, 6% PEG 20k induced a different evolution pattern of  $R_h$ , from which no nanoscale or mesoscopic (10–1000 nm) clusters were detected at the beginning of the mixing; however, after 15 min, a minor population of mesoscopic clusters approx. 200–400 nm in size occurred (Figure 6b5), and may represent the existence of a re-arranging nucleation mechanism leading to the re-directing and re-ordering of MOCs within the clusters during the nucleation process. This re-arranging nucleation mechanism was also confirmed by the increase in the corresponding DDLS signal intensities from 400 kHz to 700 kHz during the last 45 min of the measurement (Figure 6b5'). The slight drop in DLS signal intensities shown in Figure 6b4',b5' can be considered to be caused by the sedimentation of larger particles.

### 3.3. Effect of a pEF on the Crystallization Process of GI under Different Ionic and Crowding Conditions

#### 3.3.1. A pEF Modulate the Early Stage of Condensing and Prenucleation Ordering of GI

In a previous work, the effect of the pulsed electric field (pEF) on protein phase separation applying five different waveforms was investigated and demonstrated a gradient pulsed waveform (W4) can support the growth of liquid dense clusters and microcrystals with homogeneous dimensions and morphology [52]. In terms of the investigations, the identical setup with waveform 4 was applied to 2 mg/mL GI solutions containing varied ionic strength and PEG20k. The  $R_h$  evolution and DLS/DDLS signal intensities of GI in conditions without a pEF (control groups) are shown in Figure 6, but the  $R_h$  of each control group is plotted together with the  $R_h$  of the corresponding pEF group in Figure 7a1–a4,b1–b4, allowing direct comparison. For DLS and DDLS signal intensities, only the pEF groups of all conditions are shown in Figure 7a1'–a4' and b1'–b4', respectively.

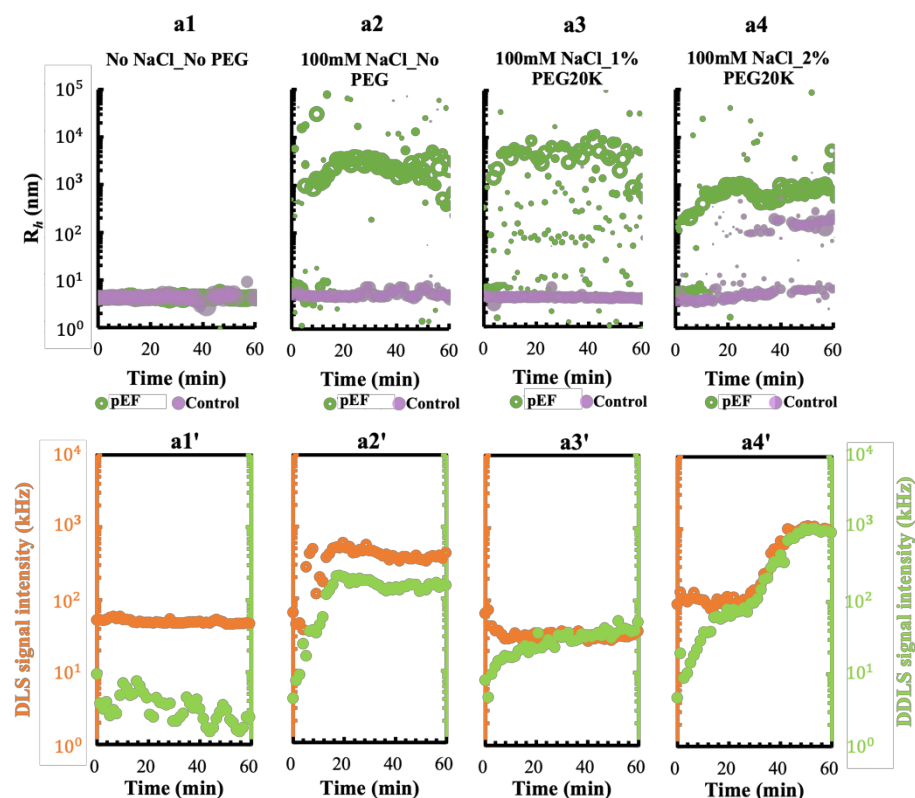
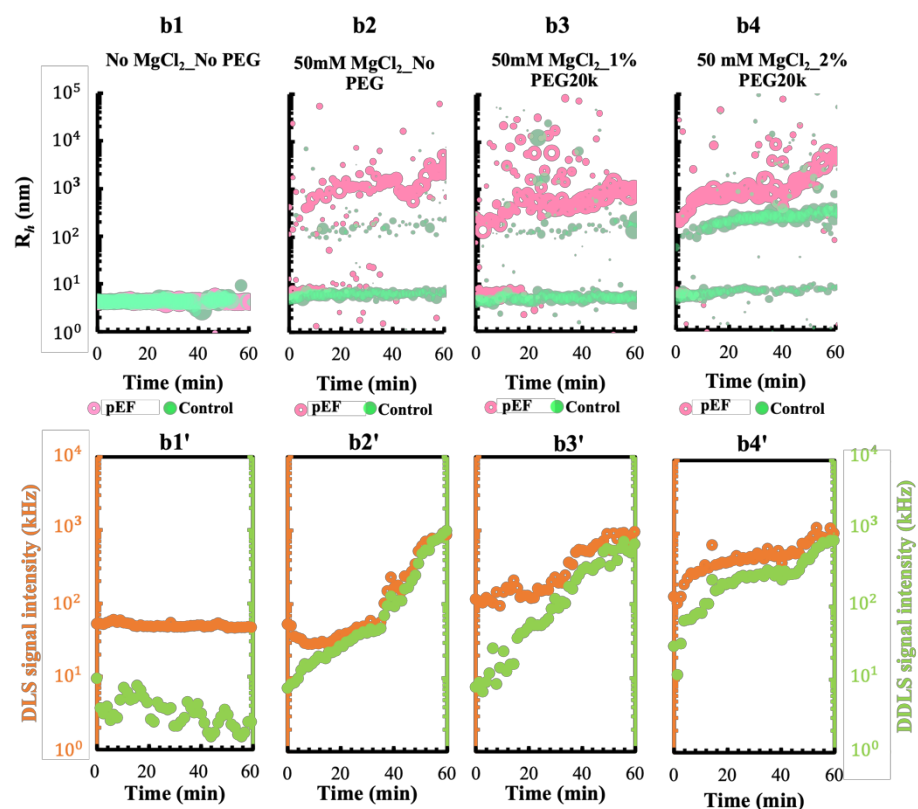


Figure 7. Cont.





**Figure 7.** The effect of a pulsed electric field on the phase behavior of GI in a solution with different ions and PEG conditions. (a1–a4) Development of the hydrodynamic radii of 2 mg/mL GI with PEG20k in a buffer containing 10 mM MES pH 6.5, 100 mM NaCl exposed to a pEF (green open circles) and without pEF (purple bubbles). (a1'–a4') The corresponding DLS (left Y-axis, orange open circles) and DDLS (right Y-axis, green closed circles) signal intensities of the pEF group monitored with a buffer containing 100 mM NaCl. (b1–b4) Evolution of the hydrodynamic radii of a 2 mg/mL GI solution mixed with PEG20k and buffer condition of 10 mM MES PH 6.5, 50 mM MgCl<sub>2</sub> with a pEF (pink open circles) and without pEF (green bubbles). (b1'–b4') The corresponding DLS and DDLS signal intensities of the pEF group monitored in a buffer containing 50 mM MgCl<sub>2</sub>. DLS/DDLS signal intensities of each control condition without pEF are shown in Figure 6.

Obviously, pEF had less or no functionality in the absence of ions, visualized by the overlap of GI  $R_h$  values between the control group (without pEF) and the pEF group (Figure 7a1). In the presence of 100 mM NaCl, the size evolution of GI with the application of pEF showed a similar pattern in Figure 7a2,a3; however, the detected DLS/DDLS intensities of GI with 1% PEG20k (Figure 7a3') was much smaller than that of GI in both conditions without PEG (Figure 7a2') and with 2% PEG20k (Figure 7a4') under pEF conditions. This is because 1% PEG20k was too low to initiate GI condensation according to the size distribution in the control group of GI with 1% PEG20k (purple bubbles in Figure 7a3), although it can slow down the motion of molecules in the solution [64]. Conversely, the formation of mesoscopic GI clusters was initiated in 20 min when PEG20k reached a concentration of 2% in the solution (purple bubbles in Figure 7a4) and was accelerated after applying a pEF (green circles in Figure 7a4), the structural ordering within mesoscopic clusters was significantly induced by the pEF, indicated by a substantial rise in the DDLS signal intensities, up to 1000 kHz (Figure 7a4'). Interestingly, based on the time at which the DLS and DDLS signal intensities rose, a simultaneous development of condensing and three-dimensional ordering was stimulated by the pEF in a GI solution without PEG (Figure 7a2'); however, an ordering prior to a condensing process occurred in a GI solution containing 1% or 2% PEG20k under the effect of pEF (Figure 7a3',a4').

The applied pEF was shown to be more effective when  $Mg^{2+}$  ions were present in the solution analyzed. The kinetic evolution of GI showed similar clustering patterns in a solution of 50 mM  $MgCl_2$  without PEG20k (Figure 7b2) and a solution with 100 mM NaCl and 2% PEG20k (Figure 7a4). In both mixing conditions, GI tetramers were consumed while particles of approx. 1  $\mu m$  were formed. Additionally, the DLS/DDLS signal intensities showed the same level of anisotropy, which may suggest that in the case of GI crystallization, a crowding agent in the crystallization solution can be replaced by a combination of applying  $Mg^{2+}$  ions and pEF. The addition of  $Mg^{2+}$  ions and PEG20k from 1% up to 2% and exposing the solution to a pEF triggered a similarly evolving pattern of size over time (Figure 7b2–b4); however, a high concentration of PEG20k accelerated the condensing and structural ordering process of GI under pEF according to the growth of DLS and DDLS signal intensities (Figure 7b2'–b4'), leading us to believe that a critical density of mesoscopic intermediates shall be reached for the nucleation, corresponding to 100 kHz of DLS signal, and may indicate the metastability of mesoscopic intermediates with respect to the crystalline phase.

### 3.3.2. Effect of Mesoscopic Ordered Clusters (MOCs) Induced by a pEF on GI Crystallization

To explore the effect of mesoscopic ordered clusters (MOCs) in a crystallization process, we applied MOCs previously produced by a pEF in a quartz cuvette (right image in Figure 8a) by adding them into the crystallization droplets of GI. As shown in Figure 3, crystallization droplets were prepared by mixing 2  $\mu L$  of the 4 mg/mL GI solution containing different volume ratios of MOCs, which served as crystallization seeds, and 2  $\mu L$  of varying concentrations of PEG20k. Then, the droplets were compared considering aspects such as the number of crystals, crystal dimensions and morphology after 24-hour incubation at 20 °C. Interestingly, the results show that the number of obtained crystals increased (Figure 8b) but their size reduced (Figure 8c) after adding increased ratios ( $v/v$ ) of MOCs in the droplet, keeping the PEG20k concentration constant. The crystal size and morphology in each droplet were kept homogenous for droplets where MOCs were placed prior to crystallization, compared to those where crystallization was performed without MOCs. This result is consistent with the assumption that increasing the number of structural ordered MOCs provided more crystallization nuclei in a droplet, and thus resulted in more crystals. However, the amount of protein molecules in a droplet is limited, and more nuclei serving as crystallization centers results in crystals with smaller dimensions. Moreover, the addition of MOCs enhanced the crystallization rate at a low concentration of PEG20k (Figure 8c, 1% PEG20k), and more crystals with homogeneous size and shape were obtained compared to the crystals formed without MOCs (Figure 8c, 4% PEG20k).

### 3.4. Effect of a pEF on Crystallizing the Pdx Complex from *S. aureus*

Large biological protein complexes, as the Pdx complex, are most of the time challenging to crystallize [43,51], thus are interesting targets to identify crystallization methods to overcome the bottleneck. Therefore, the prenucleation mechanism of a recombinant complex protein from *S. aureus*, Pdx1/Pdx2<sub>H165N</sub> (Pdx), applying the influence of a pEF was investigated to verify the general principle of the pEF to promote the biomolecular crystallization process.

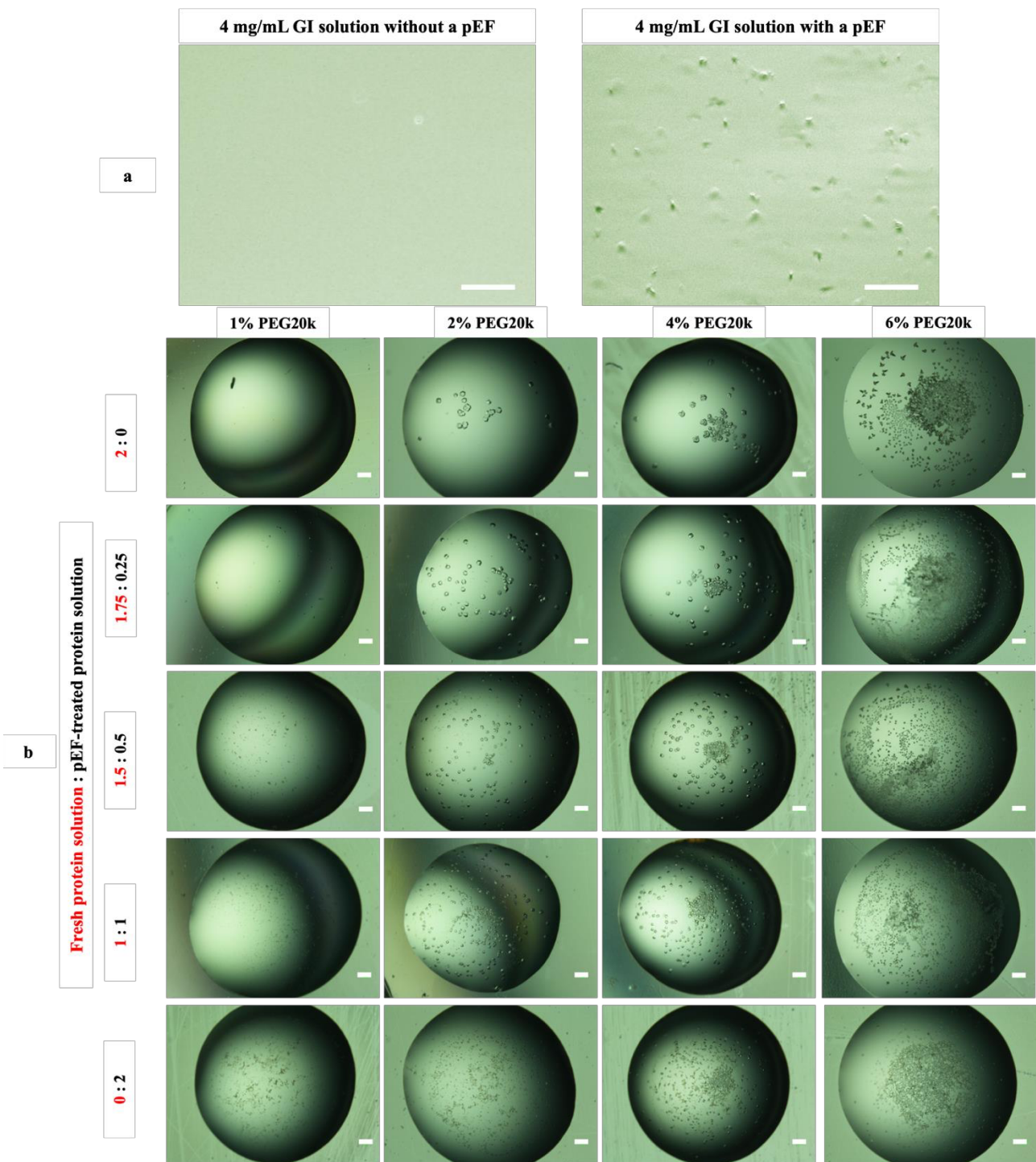
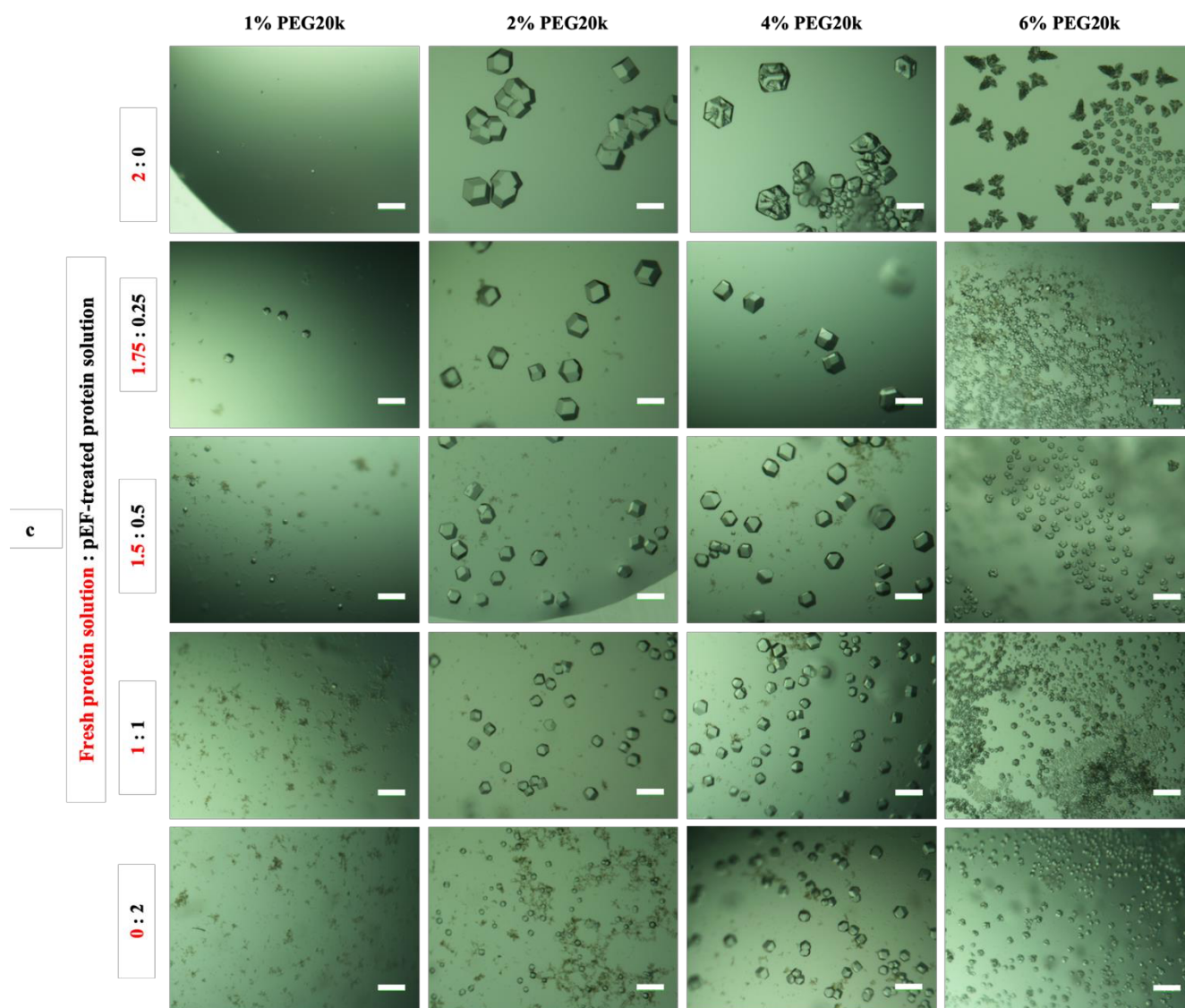


Figure 8. Cont.





**Figure 8.** (a) Forty microliters of 4 mg/mL GI in a buffer of 10 mM MES pH 6.5, 1 mM DTT and 50 mM MgCl<sub>2</sub>, incubated in a quartz cuvette for 30 min without and with the application of a pEF. The scale bar corresponds to 50  $\mu$ m. (b) GI crystals obtained from droplets with a final concentration of 2 mg/mL GI, and different ratios (*v/v*) of fresh protein solution seeded with a pEF-treated protein solution in 10 mM MES pH 6.5, 1 mM DTT and 50 mM MgCl<sub>2</sub> buffer. PEG20k in the same buffer with GI was applied as crystallization precipitant. Scale bar is 200  $\mu$ m. (c) Magnified view of crystals formed in each droplet, and the scale bar corresponds to 100  $\mu$ m. All droplets were recorded via an optical microscope after 24-hour incubation at 20  $^{\circ}$ C.

### 3.4.1. pEFs Promote the Early-Stage Ordering of Pdx Complex Nucleation

In crystallization screening experiments, crystals of the complex were obtained from a solution of 2.5 mg/mL Pdx with 5% PEG4000 after incubation of 2–5 days. The early stages of the crystallization process were monitored in the first 4 h via DLS/DDLS with and without the application of a pEF. To understand the effect of the pEF on the early-stage clustering of the Pdx complex, a Pdx crystallization concentration of 2.5 mg/mL as well as a lower concentration of 0.75 mg/mL were assessed. The Pdx complex showed a similar growth profile in terms of size evolution and density ordering at both concentrations without the application of a pEF (Figure 9a,b,a',b'). The fraction with  $R_h$  of approx. 15 nm showed a single particle population of the Pdx complex as shown in Figure 1b. The mesoscopic clusters with an initial  $R_h$  of approx. 100 nm displayed a progressive growth

(Figure 9a,b) accompanied with the rise of DLS (orange circles in Figure 9a',b') but not DDLS (green dots in Figure 9a',b') signal intensities in the first 2 h at both concentrations without the application of pEFs, indicating a condensing process of Pdx clusters without internal structural ordering within the first 4 h of the crystallization process.

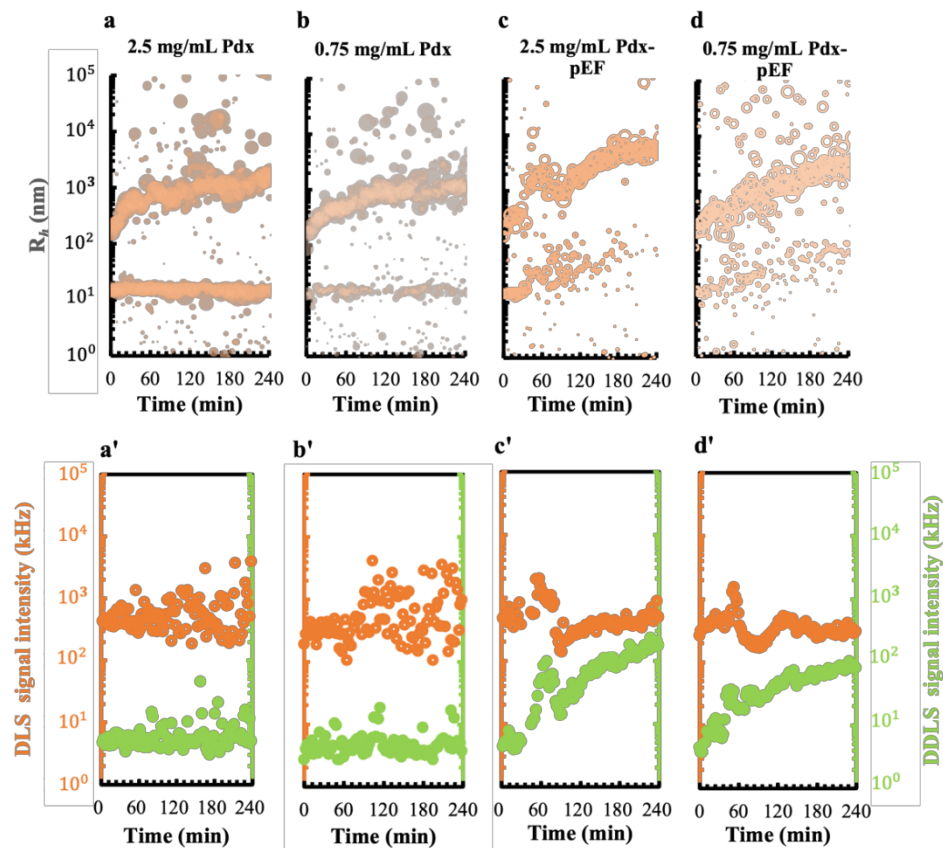


**Figure 9.** The effect of pEFs on early stages of Pdx crystallization at different protein concentrations. Kinetic evolution of the hydrodynamic particle radii from mixtures of 2.5 mg/mL Pdx with 5% PEG4000 (a) without and (c) with the application of a pEF, and mixtures at a final concentration of 0.75 mg/mL Pdx, 5% PEG4000 (b) without and (d) with a pEF. The corresponding DLS (orange open circles) and DDLS (green bubbles) signal intensities of each condition are shown in (a'–d').

The size development of Pdx mesoscopic clusters with an initial  $R_h$  of 100 nm at both protein concentrations exposed to a pEF (Figure 9c,d) showed comparable patterns with those of their corresponding control groups shown in Figure 9a,b. However, the single particle fraction of Pdx was growing steadily from approx. 15 nm to 100 nm in 4 h under the influence of the pEF (Figure 9c,d). The DDLS signal intensities fluctuated in the range of 4–20 kHz, despite the clusters growing in both control groups at 2.5 mg/mL (Figure 9a') and 0.75 mg/mL Pdx (Figure 9b'), but increased noticeably to 200 kHz in a Pdx solution of 2.5 mg/mL (Figure 9c') and to 100 kHz in a Pdx solution of 0.75 mg/mL applying the pEF for 4 h (Figure 9d'), evidencing the strong effect of the pEF on promoting the nucleation process of Pdx in a pathway where Pdx molecules ordering the three-dimensional structure in parallel with condensing.

### 3.4.2. Effect of Mesoscopic Ordered Clusters (MOCs) Induced by a pEF on Pdx Crystallization

After monitoring the early stage of Pdx crystallization, applying the pEF for 4 h via DDLS, as shown in Figure 9c, 0.5  $\mu$ L of the solution containing MOCs was taken from the cuvette and directly added as a seeding solution to the oversaturated Pdx crystallization droplets. Control droplets with the same Pdx concentration and precipitant but without

the addition of MOCs were prepared and monitored in parallel. The resulting droplets of Pdx without MOCs showed numerous cubic crystals with tiny dimensions ranging from 5 up to 30  $\mu\text{m}$  after 1 day (Figure 10a,b). In parallel, a different crystallization mechanism was observed in droplets prepared containing MOCs, which showed a lower number of homogeneous hexagonal crystals in droplets, compared to the control group after 1 day. Additionally, a lower number of larger crystals were observed after 5 days (Figure 10c,d). The crystals formed with MOCs are almost ten times larger than those formed without MOCs. Another interesting observation is the occurrence of three-dimensional multilayer stacks, also referred to as looped macrosteps visible on the surface of crystals formed with MOCs, as shown in Figure 10c,d. Those looped macrosteps on the crystals are probably caused by the fusion of mesoscopic liquid dense clusters with the macroscopic crystalline phase [35,65], characterizing the occurrence of a multiple-step nucleation of Pdx in the presence of a pEF.

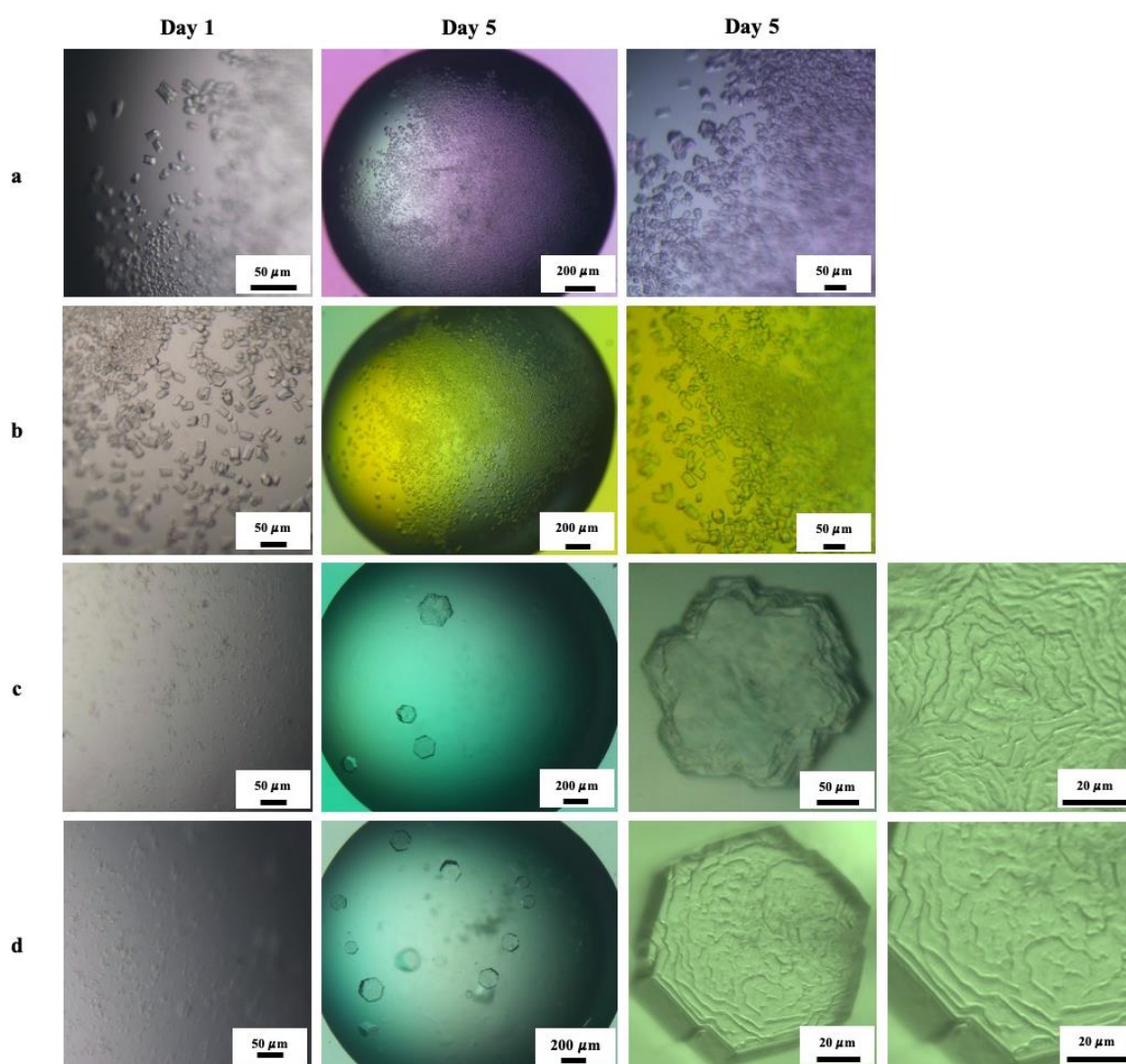


**Figure 10.** Crystallization of the Pdx complex (a,b) without and (c,d) with the addition of mesoscopic ordered clusters pre-induced by the pEF.

#### 4. Discussion

We investigated the phase and nucleation behavior of GI by monitoring time-resolved liquid phase separation, cluster formation and nucleation applying DLS/DDLS under several distinct concentrations of cations and PEG. The combined studies of the diffusion interaction parameters in solutions at different cationic conditions and the resultant phase



behavior demonstrated how cationic ions and corresponding ionic strength influence protein interactions and the development of GI clusters. Positive  $K_D$  values of GI at low ionic strength indicated strong repulsion between negatively charged GI molecules in solution. Changing a salt concentration in a protein solution at low ionic strength (<100 mM) can alter the electrostatic interactions between proteins [9]. The positive  $K_D$  values of GI decreased continuously with increasing NaCl concentration and reached a plateau in the range of 100–250 mM NaCl (black crosses in Figure 5c), where GI proteins started to form liquid dense clusters in the presence of 4% PEG20k, as shown in Figure 4a4,a5. The plateauing of protein interaction parameters at a higher ionic strength (>100 mM) was also observed by Jordan W. Bye and Robin A [66]. For GI solutions containing  $MgCl_2$ , the repulsive forces between proteins were substantially reduced at 10 mM  $MgCl_2$  (black crosses in Figure 5d), triggering the formation of mesoscopic clusters in the presence of 4% PEG20k (Figure 4b2). In an ionic strength range of 0–100 mM,  $K_D$  values dropped more sharply under the effect of  $MgCl_2$  than that influenced by NaCl, indicating that the multivalent cation is more effective in interfering with protein surface charges, therefore modulating non-specific protein interactions. Moreover,  $Mg^{2+}$  was reported to reversibly bind and dissociate at the catalytic site of GI [67], and thereby the short-range attractive interaction between GI molecules was also enhanced with increasing  $Mg^{2+}$  concentration. The driving force of GI condensing can be both non-specific (diffusion interaction, volume exclusion) and specific interactions (short-range interaction) according to the development of  $R_h$  and DLS signal intensities of GI in the presence of NaCl and  $MgCl_2$  in Figures 4 and 6. Nevertheless, to a certain extent, short-range interactions instead of only high-amplitude density fluctuations are necessary to promote structure ordering within GI clusters, as confirmed by the evolution of DDLS signal intensities of GI in a NaCl gradient and in a  $MgCl_2$  gradient, as shown in Figures 4 and 6, under the same concentration of PEG20k. Roosen-Runge et al. proposed a model which is well known in protein crystal growth, stating that multivalent metal ions can support protein contacts and can stabilize a crystal lattice by bridging protein molecules [68], which also explains the shrinkage of initial  $R_h$  of GI mesoscopic clusters formed at 10 to 50 mM  $MgCl_2$ , shown in Figure 4b, confirmed also by the increasing DDLS signal intensity, as shown in Figure 4b'. The data shown in Figures 4 and 6 also prove theoretical investigations which suggested that the crystallization pathway can be altered by adjusting the proportion of the specific and nonspecific protein interactions [69–71]. We applied an external pulsed electric field (pEF) to study how a pEF can influence the nucleation pathway of GI in different solution conditions (varying salt and PEG). The Pdx complex of high molecular weight was employed to verify the capability of pEF to modulate the protein nucleation pathway. The results from GI show that pEFs can strongly drive the protein condensing and 3D ordering. An 'ordering prior to condensing' pathway was observed for GI solutions under the influence of pEFs, demonstrated by the early rise in DDLS signal intensities, as shown in Figure 7a3',a4' and b2',b3'. This can be attributed to the effect of pEFs supporting the orientation of protein molecules and further nucleation. The substantial effect of pEFs promoting protein 3D ordering is particularly recognizable for Pdx solutions, which showed a comparative evolving pattern of an increasing size distribution (Figure 9a–d) accompanied by rising DLS signal intensities (orange open circles in Figure 9a'–d'), with a distinct rise in DDLS signal intensities in parallel (green bubbles in Figure 9c',d'). Finally, the modulating effect of obtained mesoscopic ordered clusters (MOCs), induced by a pEF, on the crystallization pathway was investigated systematically for GI applying different volume ratios of MOCs and PEG concentrations. The results show that the number of crystals and crystal dimensions obtained in a droplet can be effectively affected by changing the number of MOCs added into a droplet (Figure 8). Except for enhancing the crystallization rate of GI at a low PEG concentration (Figure 8c, 1% PEG20k), MOCs can also support the crystals' growth without crystal defects and with homogeneous size and shape for a GI solution with a high PEG concentration (Figure 8c, 4% and 6% PEG20k), probably by guiding protein molecules to attach to nuclei of pEF-induced MOCs. The universal effect of MOCs on adjusting protein crystallization was proved by applying

them to the Pdx complex (Figure 10). Notably, looped multilayer stacks emerged on the surface of the Pdx crystals formed with pre-added MOCs but not on Pdx crystals formed without MOCs. This raised the following questions: which exact mechanism contributed to the crystallization pathway with the addition of pre-induced MOCs? Do the added MOCs attach to each other and consume protein molecules in one droplet, or do they attract newly formed liquid dense clusters which attach to them and re-order to form crystals? More techniques, such as the transmission electron microscope (TEM), which can monitor crystallization processes in situ and time-resolved at the nanoscale, are required to address these questions in future.

## 5. Conclusions

The obtained data and results from GI show that short-range attractions supported by multivalent cations are required to support protein orientation and alignment in an undersaturated solution, despite the contribution of non-specific protein interactions. The nucleation pathway of GI is adaptable to the changing proportions of specific and non-specific interactions in the system. In particular, a distinct pEF is effective in driving protein ordering and clustering in the presence of ions. The structure ordering of clusters always appeared after the condensing step of GI in the absence of short-range attractions or a pEF, indicating a two-step nucleation pathway. Conversely, an ordering prior to clustering or a synchronized increase in both parameters was observed in GI solutions with a relative high concentration of  $Mg^{2+}$  ions or via the application of a pEF. Here, we also report for the first time the use of mesoscopic ordered clusters (MOCs) as ‘seeds’ with homogeneous dimensions, obtained and induced by a pEF, to systematically investigate the effect of such MOCs on the crystallization process. The application of a pEF and MOCs on the Pdx complex confirmed the rather substantial effect of pEFs in accelerating the nucleation process and the role of MOCs in modulating the crystallization pathway. Compared to the traditional seeding method utilizing a suspension of crushed crystals, the production, quality and dimensions of pEF-MOCs are reproducible and controllable. In summary, the data presented show multiple pathways for crystal nucleation and growth in complex physicochemical scenarios, which so far have not been described. In particular, the method used to induce mesoscopic ordered clusters by a pEF, which act as crystallization seeds and can be applied efficiently to modify the crystallization pathway, is most innovative.

**Author Contributions:** All authors, M.W., A.L.C.B., H.B., C.B., as listed had made a substantial, direct, and intellectual contribution to the work. Conceptualization, M.W., H.B. and C.B.; Formal analysis, M.W. and H.B.; Funding acquisition, C.B.; Investigation, M.W. and A.L.C.B.; Methodology, M.W., A.L.C.B. and H.B.; Project administration, C.B.; Supervision, H.B. and C.B.; Validation, H.B. and C.B.; Writing—original draft, M.W. and A.L.C.B.; Writing—review & editing, M.W., A.L.C.B., H.B. and C.B. All authors have read and agreed to the published version of the manuscript.

**Funding:** The authors acknowledge the support of the Cluster of Excellence ‘Advanced Imaging of Matter’ of the Deutsche Forschungsgemeinschaft (DFG)—EXC 2056—project ID 390715994, and by DFG project BE1443/29-1, financial support by the China Scholarship Council—Project ID [2020]71. We also appreciate the support of the Federal Ministry of Education and Research (BMBF) via projects 05K2020, 05K19GU4, and Fundação de Amparo à Pesquisa do Estado de São Paulo (FAPESP) through grants 2015/26722-8, 2018/21213-6, 2019/26428-3.

**Data Availability Statement:** Not applicable.

**Conflicts of Interest:** The authors declare no conflict of interest.

## References

1. Volmer, M.; Weber, A. Keimbildung in übersättigten Gebilden. *Z. Für Phys. Chem.* **1926**, *119*, 277–301. [[CrossRef](#)]
2. Li, C.; Liu, Z.; Goonetilleke, E.C.; Huang, X. Temperature-dependent kinetic pathways of heterogeneous ice nucleation competing between classical and non-classical nucleation. *Nat. Commun.* **2021**, *12*, 4954. [[CrossRef](#)] [[PubMed](#)]
3. Zhang, F.; Gavira, J.A.; Lee, G.W.; Zahn, D. Nonclassical Nucleation—Role of Metastable Intermediate Phase in Crystal Nucleation: An Editorial Prefix. *Crystals* **2021**, *11*, 174. [[CrossRef](#)]

4. Kashchiev, D. Classical nucleation theory approach to two-step nucleation of crystals. *J. Cryst. Growth* **2020**, *530*, 125300. [[CrossRef](#)]
5. Jin, B.; Liu, Z.; Tang, R. Recent experimental explorations of non-classical nucleation. *CrystEngComm* **2020**, *22*, 4057–4073. [[CrossRef](#)]
6. Brognaro, H.; Falke, S.; Mudogo, C.N.; Betzel, C. Multi-Step Concanavalin A Phase Separation and Early-Stage Nucleation Monitored Via Dynamic and Depolarized Light Scattering. *Crystals* **2019**, *9*, 620. [[CrossRef](#)]
7. Van Driessche, A.E.S.; Van Gerven, N.; Bomans, P.H.H.; Joosten, R.R.M.; Friedrich, H.; Gil-Carton, D.; Sommerdijk, N.A.J.M.; Sleutel, M. Molecular nucleation mechanisms and control strategies for crystal polymorph selection. *Nature* **2018**, *556*, 89–94. [[CrossRef](#)]
8. Sleutel, M.; Van Driessche, A.E.S. Nucleation of protein crystals—a nanoscopic perspective. *Nanoscale* **2018**, *10*, 12256–12267. [[CrossRef](#)]
9. Zhang, F. Nonclassical nucleation pathways in protein crystallization. *J. Physics Condens. Matter* **2017**, *29*, 443002. [[CrossRef](#)]
10. Sauter, A.; Roosen-Runge, F.; Zhang, F.; Lotze, G.; Jacobs, R.M.J.; Schreiber, F. Real-Time Observation of Nonclassical Protein Crystallization Kinetics. *J. Am. Chem. Soc.* **2015**, *137*, 1485–1491. [[CrossRef](#)]
11. Prestipino, S.; Laio, A.; Tosatti, E. Systematic Improvement of Classical Nucleation Theory. *Phys. Rev. Lett.* **2012**, *108*, 225701. [[CrossRef](#)] [[PubMed](#)]
12. Gebauer, D.; Cölfen, H. Prenucleation clusters and non-classical nucleation. *Nano Today* **2011**, *6*, 564–584. [[CrossRef](#)]
13. Lee, J.; Yang, J.; Kwon, S.G.; Hyeon, T. Nonclassical nucleation and growth of inorganic nanoparticles. *Nat. Rev. Mater.* **2016**, *1*, 16034. [[CrossRef](#)]
14. Ten Wolde, P.R.; Frenkel, D. Enhancement of Protein Crystal Nucleation by Critical Censity Fluctuations. *Science* **1997**, *277*, 1975–1978. [[CrossRef](#)]
15. Galkin, O.; Vekilov, P.G. Control of protein crystal nucleation around the metastable liquid–liquid phase boundary. *Proc. Natl. Acad. Sci. USA* **2000**, *97*, 6277–6281. [[CrossRef](#)]
16. Vekilov, P.G. Dense Liquid Precursor for the Nucleation of Ordered Solid Phases from Solution. *Cryst. Growth Des.* **2004**, *4*, 671–685. [[CrossRef](#)]
17. Dumetz, A.C.; Chockla, A.M.; Kaler, E.W.; Lenhoff, A.M. Comparative Effects of Salt, Organic, and Polymer Precipitants on Protein Phase Behavior and Implications for Vapor Diffusion. *Cryst. Growth Des.* **2009**, *9*, 682–691. [[CrossRef](#)]
18. Savage, J.R.; Dinsmore, A.D. Experimental Evidence for Two-Step Nucleation in Colloidal Crystallization. *Phys. Rev. Lett.* **2009**, *102*, 198302. [[CrossRef](#)]
19. Gower, L.B.; Odom, D.J. Deposition of calcium carbonate films by a polymer-induced liquid-precursor (PILP) process. *J. Cryst. Growth* **2000**, *210*, 719–734. [[CrossRef](#)]
20. Dai, L.; Douglas, E.P.; Gower, L.B. Compositional analysis of a polymer-induced liquid-precursor (PILP) amorphous CaCO<sub>3</sub> phase. *J. Non-Cryst. Solids* **2008**, *354*, 1845–1854. [[CrossRef](#)]
21. Zhu, J.; Huang, L.; Cui, M.; Ma, L.; Cao, F. A Cationic Polyelectrolyte-Controlled Liquid Mineral Precursor Process in the BaCO<sub>3</sub> System. *Eur. J. Inorg. Chem.* **2015**, *2015*, 1819–1826. [[CrossRef](#)]
22. Li, Y.; Zhu, J.; Cui, M.; Wang, J.; Zha, J. Crystallization of the polymer induced liquid mineral precursor in the constraint nanopores. *J. Cryst. Growth* **2018**, *507*, 362–369. [[CrossRef](#)]
23. Ha, T.; Kang, S. Crystallization Mechanism and Photoluminescence Properties of CaF<sub>2</sub>–Al<sub>2</sub>O<sub>3</sub>–SiO<sub>2</sub>: Eu Glass-Ceramics Based on Nano-Scale Phase Separation Phenomenon. *J. Nanosci. Nanotechnol.* **2020**, *20*, 6609–6615. [[CrossRef](#)] [[PubMed](#)]
24. Schubert, R.; Meyer, A.; Baitan, D.; Dierks, K.; Perbandt, M.; Betzel, C. Real-Time Observation of Protein Dense Liquid Cluster Evolution during Nucleation in Protein Crystallization. *Cryst. Growth Des.* **2017**, *17*, 954–958. [[CrossRef](#)]
25. Mosses, J.; Turton, D.A.; Lue, L.; Sefcik, J.; Wynne, K. Crystal templating through liquid–liquid phase separation. *Chem. Commun.* **2015**, *51*, 1139–1142. [[CrossRef](#)]
26. Dai, H.; Chen, L.; Zhang, B.; Si, G.; Liu, Y.J. Optically isotropic, electrically tunable liquid crystal droplet arrays formed by photopolymerization-induced phase separation. *Opt. Lett.* **2015**, *40*, 2723–2726. [[CrossRef](#)]
27. Trilisky, E.; Gillespie, R.; Osslund, T.D.; Vunnum, S. Crystallization and liquid-liquid phase separation of monoclonal antibodies and fc-fusion proteins: Screening results. *Biotechnol. Prog.* **2011**, *27*, 1054–1067. [[CrossRef](#)]
28. Mudogo, C.N.; Falke, S.; Brognaro, H.; Duszenko, M.; Betzel, C. Protein phase separation and determinants of in cell crystallization. *Traffic* **2020**, *21*, 220–230. [[CrossRef](#)]
29. Hasecke, F.; Miti, T.; Perez, C.; Barton, J.; Schölzel, D.; Gremer, L.; Grüning, C.S.R.; Matthews, G.; Meisl, G.; Knowles, T.P.J.; et al. Origin of metastable oligomers and their effects on amyloid fibril self-assembly. *Chem. Sci.* **2018**, *9*, 5937–5948. [[CrossRef](#)]
30. Hardenberg, M.C.; Sinnige, T.; Casford, S.; Dada, S.T.; Poudel, C.; Robinson, E.A.; Fuxreiter, M.; Kaminski, C.F.; Kaminski-Schierle, G.S.; Nollen, E.A.A.; et al. Observation of an  $\alpha$ -synuclein liquid droplet state and its maturation into Lewy body-like assemblies. *J. Mol. Cell Biol.* **2021**, *13*, 282–294. [[CrossRef](#)]
31. Sawner, A.S.; Ray, S.; Yadav, P.; Mukherjee, S.; Panigrahi, R.; Poudyal, M.; Patel, K.; Ghosh, D.; Kummerant, E.; Kumar, A.; et al. Modulating  $\alpha$ -Synuclein Liquid–Liquid Phase Separation. *Biochemistry* **2021**, *60*, 3676–3696. [[CrossRef](#)] [[PubMed](#)]
32. Kashchiev, D.; Vekilov, P.G.; Kolomeisky, A.B. Kinetics of two-step nucleation of crystals. *J. Chem. Phys.* **2005**, *122*, 244706. [[CrossRef](#)] [[PubMed](#)]
33. Vekilov, P.G. The two-step mechanism of nucleation of crystals in solution. *Nanoscale* **2010**, *2*, 2346–2357. [[CrossRef](#)] [[PubMed](#)]
34. Vekilov, P.G. Nucleation. *Cryst. Growth Des.* **2010**, *10*, 5007–5019. [[CrossRef](#)] [[PubMed](#)]

35. Sleutel, M.; Van Driessche, A.E.S. Role of clusters in nonclassical nucleation and growth of protein crystals. *Proc. Natl. Acad. Sci. USA* **2014**, *111*, E546–E553. [[CrossRef](#)]
36. Houben, L.; Weissman, H.; Wolf, S.G.; Rybtchinski, B. A mechanism of ferritin crystallization revealed by cryo-STEM tomography. *Nature* **2020**, *579*, 540–543. [[CrossRef](#)]
37. Van Driessche, A.E.S.; Van Gerven, N.; Joosten, R.R.M.; Ling, W.L.; Bacía, M.; Sommerdijk, N.; Sleutel, M. Nucleation of protein mesocrystals via oriented attachment. *Nat. Commun.* **2021**, *12*, 3902. [[CrossRef](#)]
38. Holloway, L.; Roche, A.; Marzouk, S.; Uddin, S.; Ke, P.; Ekizoglou, S.; Curtis, R. Determination of Protein-Protein Interactions at High Co-Solvent Concentrations Using Static and Dynamic Light Scattering. *J. Pharm. Sci.* **2020**, *109*, 2699–2709. [[CrossRef](#)]
39. Da Vela, S.; Begam, N.; Dyachok, D.; Schäufele, R.S.; Matsarskaia, O.; Braun, M.K.; Girelli, A.; Ragulskaya, A.; Mariani, A.; Zhang, F.; et al. Interplay between Glass Formation and Liquid-Liquid Phase Separation Revealed by the Scattering Invariant. *J. Phys. Chem. Lett.* **2020**, *11*, 7273–7278. [[CrossRef](#)]
40. Begam, N.; Matsarskaia, O.; Sztucki, M.; Zhang, F.; Schreiber, F. Unification of lower and upper critical solution temperature phase behavior of globular protein solutions in the presence of multivalent cations. *Soft Matter* **2020**, *16*, 2128–2134. [[CrossRef](#)]
41. Braun, M.K.; Sauter, A.; Matsarskaia, O.; Wolf, M.; Roosen-Runge, F.; Sztucki, M.; Roth, R.; Zhang, F.; Schreiber, F. Reentrant Phase Behavior in Protein Solutions Induced by Multivalent Salts: Strong Effect of Anions Cl<sup>-</sup> Versus NO<sub>3</sub><sup>-</sup>. *J. Phys. Chem. B* **2018**, *122*, 11978–11985. [[CrossRef](#)] [[PubMed](#)]
42. Salje, E.K.H. Multi-scaling and mesoscopic structures. *Philos. Trans. R. Soc. London. Ser. A Math. Phys. Eng. Sci.* **2010**, *368*, 1163–1174. [[CrossRef](#)] [[PubMed](#)]
43. Barra, A.L.C.; Dantas, L.D.O.C.; Morão, L.G.; Gutierrez, R.F.; Polikarpov, I.; Wrenger, C.; Nascimento, A.S. Essential Metabolic Routes as a Way to ESKAPE From Antibiotic Resistance. *Front. Public Health* **2020**, *8*, 26. [[CrossRef](#)]
44. Strohmeier, M.; Raschle, T.; Mazurkiewicz, J.; Rippe, K.; Sinning, I.; Fitzpatrick, T.B.; Tews, I. Structure of a bacterial pyridoxal 5'-phosphate synthase complex. *Proc. Natl. Acad. Sci. USA* **2006**, *103*, 19284–19289. [[CrossRef](#)]
45. Lobley, C.M.C.; Sandy, J.; Sanchez-Weatherby, J.; Mazzorana, M.; Krojer, T.; Nowak, R.P.; Sørensen, T.L.-M. A generic protocol for protein crystal dehydration using the HC1b humidity controller. *Acta Crystallogr. Sect. D Struct. Biol.* **2016**, *72*, 629–640. [[CrossRef](#)]
46. Bolisetty, S.; Harnau, L.; Jung, J.-M.; Mezzenga, R. Gelation, Phase Behavior, and Dynamics of  $\beta$ -Lactoglobulin Amyloid Fibrils at Varying Concentrations and Ionic Strengths. *Biomacromolecules* **2012**, *13*, 3241–3252. [[CrossRef](#)] [[PubMed](#)]
47. Schubert, R.; Meyer, A.; Dierks, K.; Kapis, S.; Reimer, R.; Einspahr, H.; Perbandt, M.; Betzel, C. Reliably distinguishing protein nanocrystals from amorphous precipitate by means of depolarized dynamic light scattering. *J. Appl. Crystallogr.* **2015**, *48*, 1476–1484. [[CrossRef](#)]
48. Balog, S.; Rodriguez-Lorenzo, L.; Monnier, C.A.; Obiols-Rabasa, M.; Rothen-Rutishauser, B.; Schurtenberger, P.; Petri-Fink, A. Characterizing nanoparticles in complex biological media and physiological fluids with depolarized dynamic light scattering. *Nanoscale* **2015**, *7*, 5991–5997. [[CrossRef](#)]
49. Chayen, N.; Dieckmann, M.; Dierks, K.; Fromme, P. Size and Shape Determination of Proteins in Solution by a Noninvasive Depolarized Dynamic Light Scattering Instrument. *Ann. N. Y. Acad. Sci.* **2004**, *1027*, 20–27. [[CrossRef](#)]
50. Vailati, A.; Asnaghi, D.; Giglio, M.; Piazza, R. Depolarized dynamic light scattering from optically anisotropic reaction-limited aggregates. *Phys. Rev. E* **1993**, *48*, R2358–R2361. [[CrossRef](#)]
51. Ullah, N.; Andaleeb, H.; Mudogo, C.N.; Falke, S.; Betzel, C.; Wrenger, C. Solution Structures and Dynamic Assembly of the 24-Meric Plasmodial Pdx1–Pdx2 Complex. *Int. J. Mol. Sci.* **2020**, *21*, 5971. [[CrossRef](#)] [[PubMed](#)]
52. Wang, M.; Falke, S.; Schubert, R.; Lorenzen, K.; Cheng, Q.-D.; Exner, C.; Brognaro, H.; Mudogo, C.N.; Betzel, C. Pulsed electric fields induce modulation of protein liquid-liquid phase separation. *Soft Matter* **2020**, *16*, 8547–8553. [[CrossRef](#)] [[PubMed](#)]
53. Schubert, R. Preparation and Scoring of Protein Nano- and Microcrystals for Synchrotron and Free-Electron Laser X-ray Radiation Sources. Ph.D. Thesis, University Hamburg: Hamburg, Germany, 2016; p. 157.
54. Provencher, S.W. A constrained regularization method for inverting data represented by linear algebraic or integral equations. *Comput. Phys. Commun.* **1982**, *27*, 213–227. [[CrossRef](#)]
55. Einstein, A. Theory of the Brownian movements. *Ann. Phys.* **1905**, *17*, 549. [[CrossRef](#)]
56. Debye, P. *Polar Molecules*; The Chemical Catalog Company, Inc.: Dover, NY, USA, 1929.
57. Kenrick, S.; Some, D. *The Diffusion Interaction Parameter (kD) as an Indicator of Colloidal and Thermal Stability*; Wyatt Technology Corporation: Santa Barbara, CA, USA, 2014; pp. 1–6.
58. Roberts, D.; Keeling, R.; Tracka, M.; van der Walle, C.F.; Uddin, S.; Warwicker, J.; Curtis, R. The Role of Electrostatics in Protein-Protein Interactions of a Monoclonal Antibody. *Mol. Pharm.* **2014**, *11*, 2475–2489. [[CrossRef](#)]
59. Kozak, M. Glucose isomerase from *Streptomyces rubiginosus*—potential molecular weight standard for small-angle X-ray scattering. *J. Appl. Crystallogr.* **2005**, *38*, 555–558. [[CrossRef](#)]
60. Falke, S.; Brognaro, H.; Martirosyan, A.; Dierks, K.; Betzel, C. A multi-channel in situ light scattering instrument utilized for monitoring protein aggregation and liquid dense cluster formation. *Heliyon* **2019**, *5*, e03016. [[CrossRef](#)]
61. Oberthuer, D.; Melero-García, E.; Dierks, K.; Meyer, A.; Betzel, C.; Garcia-Caballero, A.; Gavira, J.A. Monitoring and Scoring Counter-Diffusion Protein Crystallization Experiments in Capillaries by in situ Dynamic Light Scattering. *PLoS ONE* **2012**, *7*, e33545. [[CrossRef](#)]
62. Hofmeister, F. Zur Lehre von der Wirkung der Salze. *Naunyn-Schmiedebergs Arch. Exp. Pathol. Pharmacol.* **1888**, *24*, 247–260. [[CrossRef](#)]



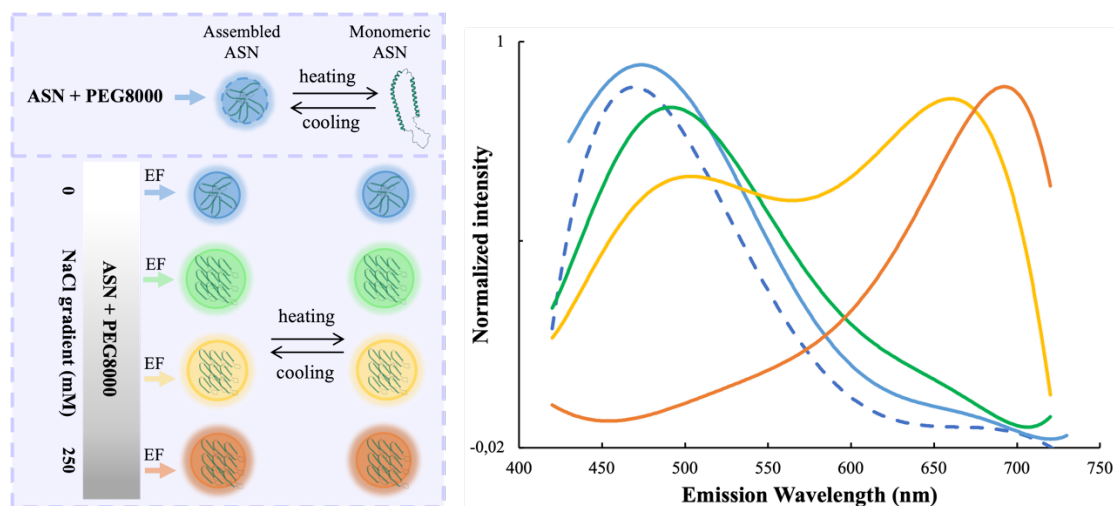
63. Miklos, A.C.; Li, C.; Sharaf, N.G.; Pielak, G.J. Volume Exclusion and Soft Interaction Effects on Protein Stability under Crowded Conditions. *Biochemistry* **2010**, *49*, 6984–6991. [[CrossRef](#)]
64. Zitserman, V.Y.; Stojilkovich, K.S.; Berezhkovskii, A.M.; Bezrukov, S.M. Electrical conductivity of aqueous solutions of polyethylene glycol. *Russ. J. Phys. Chem. A* **2005**, *79*, 1083–1089.
65. McPherson, A.; Kuznetsov, Y.G. Mechanisms, kinetics, impurities and defects: Consequences in macromolecular crystallization. *Acta Crystallogr. Sect. F Struct. Biol. Commun.* **2014**, *70*, 384–403. [[CrossRef](#)] [[PubMed](#)]
66. Bye, J.W.; Curtis, R.A. Controlling Phase Separation of Lysozyme with Polyvalent Anions. *J. Phys. Chem. B* **2018**, *123*, 593–605. [[CrossRef](#)]
67. Bae, J.-E.; Hwang, K.Y.; Nam, K.H. Structural analysis of substrate recognition by glucose isomerase in Mn<sup>2+</sup> binding mode at M2 site in *S. rubiginosus*. *Biochem. Biophys. Res. Commun.* **2018**, *503*, 770–775. [[CrossRef](#)] [[PubMed](#)]
68. Roosen-Runge, F.; Zhang, F.; Schreiber, F.; Roth, R. Ion-activated attractive patches as a mechanism for controlled protein interactions. *Sci. Rep.* **2014**, *4*, 7016. [[CrossRef](#)] [[PubMed](#)]
69. Staneva, I.; Frenkel, D. The role of non-specific interactions in a patchy model of protein crystallization. *J. Chem. Phys.* **2015**, *143*, 194511. [[CrossRef](#)]
70. Hedges, L.O.; Whitelam, S. Limit of validity of Ostwald's rule of stages in a statistical mechanical model of crystallization. *J. Chem. Phys.* **2011**, *135*, 164902. [[CrossRef](#)]
71. Whitelam, S. Control of Pathways and Yields of Protein Crystallization through the Interplay of Nonspecific and Specific Attractions. *Phys. Rev. Lett.* **2010**, *105*, 88102. [[CrossRef](#)]



### 5.3 Formation kinetics and physicochemical properties of mesoscopic $\alpha$ -synuclein (ASN) assemblies modulated by sodium chloride and a distinct pulsed electric field

#### Summary

After obtaining insights about the effect of pEFs on protein phase separation and its subsequent transition towards crystallization, we continued exploring the effect of pEFs on protein phase separation within the phase transition model of protein fibrillation. Results in this publication show the influence of ionic strengths and pEFs on the assembling kinetics of an intrinsically disordered protein, ASN, and the physicochemical properties of ASN assemblies, including the thermostability and autofluorescence properties. The subsequent fibrillation processes of mesoscopic ASN assemblies formed with distinct growth mechanisms and physicochemical properties were analysed at different time scales and resolution scales. The corresponding molecular mechanism was discussed according to the experimental data obtained from measuring the secondary structure and the diffusion interaction parameter ( $K_D$ ) of monomeric ASN. It was found that the growth mechanisms and physicochemical properties of mesoscopic ASN assemblies can be altered by applying pEFs and a NaCl gradient, which could attribute to the alterations of both conformation and electrostatic interactions of monomeric ASN.



**Graphic abstract.** The thermostability and autofluorescence properties of mesoscopic ASN assemblies formed under varied NaCl concentrations and a distinct pEF.<sup>144</sup> The scheme on the left side is showing a comparison of the thermostability of ASN assemblies induced by PEG8000 alone with the ASN assemblies formed with PEG8000 and a gradient of NaCl applying a pEF. The graph on the right side is the autofluorescence emission spectra of corresponding ASN assemblies shown in the left scheme. The dashed line represents ASN

assemblies formed without a pEF. Solid lines in different colours represent ASN assemblies formed under a pEF at different NaCl concentrations.



Cite this: DOI: 10.1039/d2sm01615j

## Formation kinetics and physicochemical properties of mesoscopic Alpha-Synuclein assemblies modulated by sodium chloride and a distinct pulsed electric field†

 Mengying Wang,<sup>a</sup> Roland Thuenauer,<sup>bcd</sup> Robin Schubert,<sup>e</sup> Susanna Gevorgyan,<sup>a</sup> Kristina Lorenzen,<sup>e</sup> Hévila Brognaro<sup>a</sup> and Christian Betzel<sup>\*a</sup>

Alpha-Synuclein (ASN), a presynaptic protein, has been widely reported to form amyloid-rich hydrogel clusters through liquid–liquid phase separation (LLPS) and liquid-to-solid transition. However, in-depth investigations about the parameters that influence the assembling kinetics, structures, and physicochemical properties of intermediate ASN assemblies are still missing. Therefore, we monitored for the first time the assembling and ordering kinetics of ASN by polarized/depolarized light scattering (DLS/DDLS) under the effect of ionic strength and a pulsed electric field (EF), followed by characterizing the resultant ASN assemblies applying thermostability assays, fluorescence/autofluorescence assays, and TEM. The underlying molecular mechanism was discussed based on experimental evidence. Results showed that in the presence of 150–250 mM NaCl, monomeric ASN is highly soluble in a temperature range of 20–70 °C and could form dissoluble liquid dense clusters *via* LLPS in crowded environments, while the ionic strength of 50 mM NaCl could trigger conformational changes and attractive diffusion interactions of ASN monomers towards the formation of mesoscopic assemblies with ordered internal structures and high thermostabilities. We discovered that pulsed EFs and ionic strength can modulate effectively the thermostability and autofluorescence effect of mesoscopic ASN assemblies by tuning the molecular interaction and arrangement. Remarkably, a specie of thermostable ASN assemblies showing a maximum autofluorescence emission at approx. 700 nm was synthesized applying 250 mM NaCl and the distinct pulsed EF, which could be attributed to the increase of  $\beta$ -sheet structures and hydrogen-bond networks within ASN assemblies. In summary, the presented data provide novel insights for modulating the growth kinetics, structures, and physicochemical properties of bio-macromolecular mesoscopic assemblies.

 Received 8th December 2022,  
Accepted 21st January 2023

DOI: 10.1039/d2sm01615j

[rsc.li/soft-matter-journal](http://rsc.li/soft-matter-journal)

## Introduction

Alpha-Synuclein (ASN) is an aggregation-prone protein, whose physiological function covers maintaining lipid-packing, sensing, and vesicle fusion.<sup>1–4</sup> Fibrillar aggregates of ASN have been widely

detected in the nerve tissue of Parkinson's patients.<sup>5–9</sup> It was demonstrated that ASN undergoes liquid–liquid phase separation (LLPS) and liquid-to-solid transition before forming amyloid fibrils.<sup>10</sup> Recently, Sawner and Ray *et al.* (2021) have investigated and published the influence of pH, salt, PD-associated multivalent cations, N-terminal acetylation on the critical time and critical concentration of ASN LLPS *in vitro* applying PEG8000.<sup>11</sup> Monomeric ASN is a natively unfolded protein and can adapt a number of conformational states, caused by different intramolecular interactions in varying physicochemical environments.<sup>12</sup> The intramolecular interactions depend on electrostatic/hydrophobic interactions and hydrogen bonds between amino acid residues.<sup>13</sup> As a result, altering the physicochemical parameters, such as pH, salt, temperature, and external fields, can induce conformational changes in monomeric ASN and in ASN assemblies. The aggregation mechanism and the early stages of ASN fibrils have been investigated for many years. Krishnan and collaborators found in

<sup>a</sup> University of Hamburg, Laboratory for Structural Biology of Infection and Inflammation, Institute of Biochemistry and Molecular Biology, Notkestrasse 85, c/o DESY, Building 22a, 22607, Hamburg, Germany. E-mail: christian.betzel@uni-hamburg.de

<sup>b</sup> Technology Platform Light Microscopy, University of Hamburg, Mittelweg 177, 20148, Hamburg, Germany

<sup>c</sup> Center for Structural Systems Biology (CSSB), Notkestrasse 85, c/o DESY, Building 15, 22607, Hamburg, Germany

<sup>d</sup> Technology Platform Microscopy and Image Analysis (TP MIA), Leibniz Institute of Virology (LIV), Martinistrasse 52, 20251, Hamburg, Germany

<sup>e</sup> European XFEL GmbH, Holzkoppel 4, 22869, Schenefeld, Germany

† Electronic supplementary information (ESI) available. See DOI: <https://doi.org/10.1039/d2sm01615j>



2003 that the formation of an ASN dimer is the critical step for fibrillation,<sup>6</sup> while in 2008 Tashiro's group, using time-resolved SAXS, detected an oligomerized heptamer at the initial stage of ASN fibrillation.<sup>14</sup> Applying dynamic light scattering, Saraiva (2021) identified micellar-like aggregates with hydrodynamic radii ( $R_h$ ) of approx. 210 nm at low concentrations of ASN (<100  $\mu\text{M}$ ) and oligomers with  $R_h$  approx. 82 nm at high protein concentrations (>100  $\mu\text{M}$ ) in the early stages of aggregation.<sup>15</sup> Especially, the metastable globular oligomers have been observed widely preceding the formation of rigid fibrils as protofibrils.<sup>16–19</sup> On the other hand, using both amyloid- $\beta$  and lysozyme, Hasecke *et al.* (2018) revealed that the fibril assembling kinetics depends on the critical oligomer concentration and suggested that the globular oligomers can compete with the fibrils consuming monomeric proteins, thus inhibiting the nucleation and growth of rigid fibrils.<sup>20</sup> Obviously, the interconvertibility among ASN monomers, dimers, oligomers, and fibrils highly depends on the physicochemical conditions.

It was reported that an electric field (EF) strength across the neuron synapses is approx. 40 kV  $\text{cm}^{-1}$ ,<sup>21</sup> which can cause the self-aggregation of proteins. In this context, the role of EFs in the assembling process of ASN and the physicochemical properties of intermediate ASN assemblies are till now not studied. Therefore, in the data we present and corresponding experiments performed, we focus on gaining insights into the effect of physicochemical factors, EFs and a NaCl gradient, on the early-stage assembling mechanism of ASN and the physicochemical properties of ASN intermediate assemblies. The experimental strategy is shown in Scheme 1. Polarized, and depolarized dynamic light scattering (DLS/DDLS) were employed to monitor simultaneously the early-stage evolution of the hydrodynamic radius and anisotropy of ASN assemblies. A light scattering instrument installed with a temperature control program was utilized to analyse the thermostability of monomeric ASN and the interconvertibility between ASN assemblies, oligomers, and monomers. Transmission electron microscopy (TEM), optical brightfield microscopy, and confocal laser scanning microscopy

(CLSM) were applied to characterize the morphologies and auto-fluorescence effect of ASN assemblies. Finally, the diffusion interaction parameter- $K_D$  and the secondary structure of monomeric ASN under different conditions were also determined to uncover the underlying molecular mechanism resulting in the diverse phase behaviours of ASN.

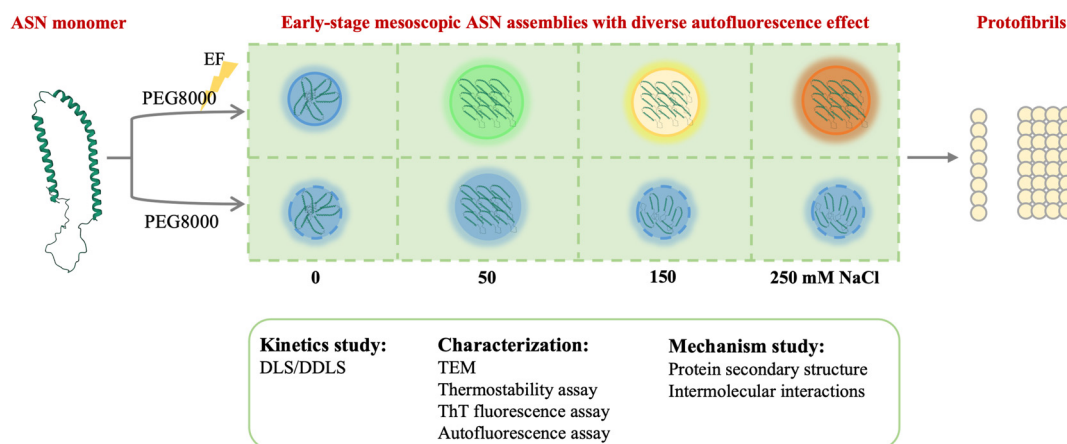
## Results and discussion

### Phase diagram of $\alpha$ -Synuclein in solution at pH 7.4 and applying PEG8000 as a crowding agent

With the resolution of an optical microscope Leica M205C, ASN dense liquid clusters (DLCs) and mesoscopic globular assemblies (10–1000 nm) were observed from droplets incubated 1 hour in a sitting-drop plate at 20 °C and conditions shown in the dotted frame of Fig. 1. It was noticed that ASN at high concentrations (200–500  $\mu\text{M}$ ) tended to undergo liquid–liquid phase separation (LLPS) and form DLCs after 1 hour incubation with 10–20% PEG8000, followed by liquid to gel-like transitions within 72 hours of incubation (ESI† Fig. S2–S4). However, at low concentrations (5–100  $\mu\text{M}$ ) ASN mainly aggregated to globular mesoscopic assemblies within 1 hour of incubation applying 15–20% PEG8000 (Fig. 1). Similar phase diagram of ASN mixed with PEG8000 was also observed by Sawner's group<sup>11</sup> and Ray's lab.<sup>22</sup> ASN self-assemblies, without applying a crowding agent, were also observed after 24 hours of incubation (the first column of ESI† Fig. S2). The mesoscopic assemblies have homogeneous dimensions regardless which protein concentration was applied. Further, fibrillar structures formed *via* the linear attachment of mesoscopic globular assemblies were observed in droplets containing 50–100  $\mu\text{M}$  ASN and PEG8000 after 24 hours of incubation (ESI† Fig. S2–S4), which can be considered to be the origin of fibrillation.

### Monitoring the dynamic assembling and three dimensional (3D)-ordering of $\alpha$ -Synuclein in a NaCl gradient exposed to pulsed EFs

To obtain insights about the early-stage assembling and 3D-ordering kinetics of ASN, a non-invasive DLS/DDLS technique



**Scheme 1** Experimental strategy. The coordinates of monomeric  $\alpha$ -Synuclein (ASN) were obtained from the protein data bank (PDB code: 2KKW).<sup>40</sup> The colour of mesoscopic assemblies denotes the diverse autofluorescence effects. The molecular arrangement shown in different assemblies do not represent the real inner structure of ASN assemblies.



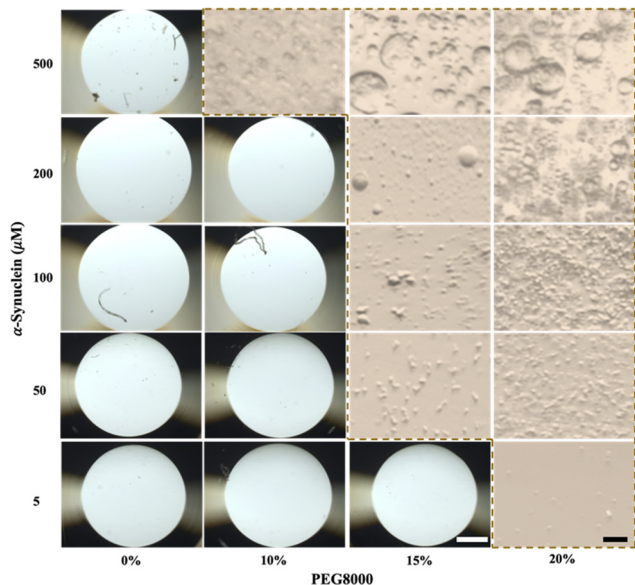


**Fig. 1** Representative phase diagram of  $\alpha$ -Synuclein after 1 hour incubation applying PEG8000 in a buffer of 20 mM Tris pH 7.4, 150 mM NaCl and 1 mM DTT at 20 °C. The white scale bar corresponds to 50  $\mu$ m for all droplets, while the black scale bar represents 10  $\mu$ m for all magnified images shown in the dotted frame.

monitoring simultaneously and time-resolved the hydrodynamic radii and optical anisotropy of particles was utilized. Firstly, ASN solutions applying NaCl in a range of 0–250 mM and pH 7.4 were investigated at 20 °C to understand the effect of NaCl and the applied EF on ASN stabilities and self-assembling behaviour. As a sufficient DLS signal intensity is required for generating a normal autocorrelation function to analyse the particle radii, a concentration of 200  $\mu$ M ASN was applied for the pure protein samples. Results showed that the monomeric ASN was stable within 2 hours of measurements at high concentrations of NaCl, 150–250 mM (the upper panel of Fig. 2a). However, oligomers with a hydrodynamic radius ( $R_h$ ) of approx. 7.6 nm and 46.0 nm formed after 2 hours in solutions containing none NaCl, and 50 mM of NaCl, respectively.

The clustering evolution was also monitored in solutions containing 50  $\mu$ M ASN, a physiological relevant ASN concentration, 15% PEG8000, and NaCl ranging from 0 up to 250 mM. Fig. 2b revealed the instant formation of ASN oligomers with  $R_h$  of approx. 20 nm in the absence, and the presence of 150–250 mM NaCl. Accordingly, the  $R_h$  growth kinetics of ASN oligomers in presence of 150–250 mM NaCl followed the scaling power law of  $R_h = k \times t^{0.33}$ , where  $k$  is a constant pre-factor and  $t$  is the time,<sup>23</sup> demonstrating a diffusion-limited Ostwald ripening mechanism of LLPS.<sup>24</sup> Despite the fact that the initial and final  $R_h$  of ASN assemblies obtained at 0 mM NaCl are comparable with assemblies obtained at 150–250 mM NaCl, the  $R_h$  developing pattern observed within 2 hours of measurements showed a power law of  $t^{0.2}$  at 0 mM NaCl. The ionic strength of 50 mM NaCl favoured the largest ASN assemblies with  $R_h$  approx. 100 nm appearing and growing with the power law of  $R_h = k \times t^{0.5}$ , implying a surface attachment-limited coarsening.<sup>23</sup> It's worth noting that the growth of ASN  $R_h$

from 100 to 500 nm in 18 minutes was accompanied by the descent of the corresponding DLS signal intensity (purple circles) and an increase of the DDLS signal intensity (green rhombuses) (Fig. 2b). Considering that the DLS signal intensity depends on the particle size and concentration,<sup>25</sup> thus the reducing DLS signal intensity indicated that parts of metastable mesoscopic assemblies formed at the beginning of mixing and were consumed during the growth and ordering of ASN assemblies. Both, DLS and DDLS signal intensities reached a plateau after 18 minutes, considering the continuous growth of  $R_h$ , it indicates an equilibrium between the growth in size and the decrease in the number of ASN assemblies. Fig. 2c and d are displaying the evolving results of ASN in the same solutions, as shown in Fig. 2a and b, respectively, but under the influence of a pulsed electric field (EF) applied throughout during the measurement. Compared to the corresponding control groups, it is apparent that EFs prompted the formation of ANS assemblies with a slight anisotropy in the absence of PEG8000. According to the  $R_h$  growth pattern and DLS/DDLS signal intensities obtained for the control and EF experiments we showed that EF cannot influence the phase behaviour of ASN in a PEG8000 solution without the presence of ions (Fig. 2b and d, 0 mM NaCl). However, the applied EF modified the early-stage phase behaviours of ASN in PEG8000 solutions containing 50–250 mM NaCl, since the obtained  $R_h$  data did not fit to the scaling power law of both the surface attachment-limited coarsening ( $t^{0.5}$ ) and the diffusion-limited Ostwald ripening ( $t^{0.33}$ ) mechanisms (Fig. 2d, 50–250 mM NaCl). The DDLS signal intensities of EF groups at 150–250 mM NaCl were stronger than their corresponding control groups, suggesting a more ordered alignment of ASN molecules, guided by the applied EF. To analyse further the effect of NaCl and applied EF on physicochemical properties of ASN assemblies and considering the visible particle dimension, samples, presented in Fig. 2b and d, were characterized by TEM and optical microscopy, as summarized below.

### Characterizing the morphologies and $\beta$ -sheet structures of assembled $\alpha$ -Synuclein at different time scale

To track the morphological transitions of ASN assemblies considering a physiological relevant protein concentration of 50  $\mu$ M,<sup>26,27</sup> samples shown in Fig. 2b and d were incubated at 20 °C for 3 days and analysed afterwards by TEM. Results showed that mesoscopic ASN assemblies formed in control groups without EFs showed mainly a globular shape (upper row of Fig. 3a), whereas aggregated assemblies were also observed in EF groups (lower row of Fig. 3a). Especially, protofibril-like morphologies formed through curvilinear or linear attachment of globular assemblies were detected in EF groups containing 0 and 50 mM NaCl, respectively. Thioflavin T (ThT), which increases the fluorescence intensity upon binding to amyloid  $\beta$  sheets, was used to analyse the fibrillation of ASN assemblies. In accordance with the DDLS results about the internal structure changes, ASN assemblies in the EF group containing 150 or 250 mM NaCl exhibited a higher fluorescence intensity than the control group, while no noticeable difference was detected between the control and EF groups at solution conditions of 0–50 mM NaCl (Fig. 3b). It was reported that Congo red (CR) dye specifically stains stacked  $\beta$ -sheet aggregates and





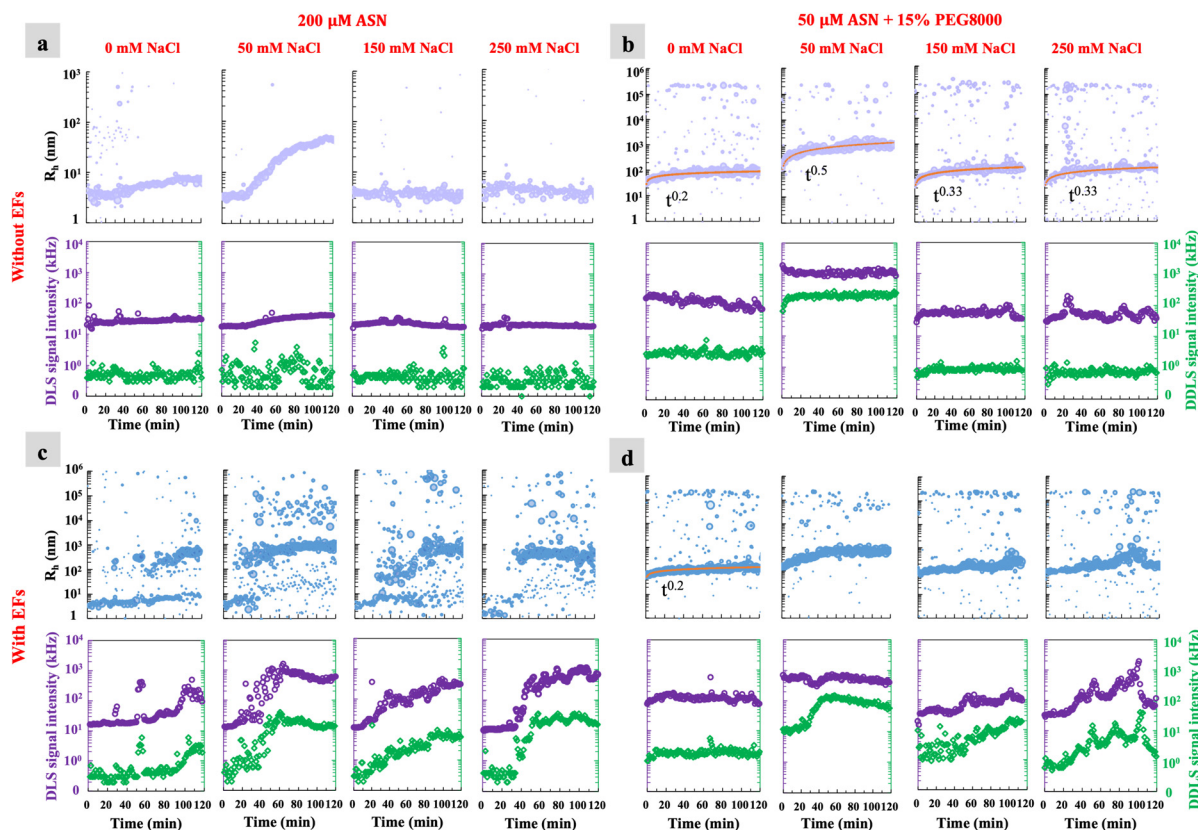


Fig. 2 The dynamic evolution of hydrodynamic radii and internal order during the early stage assembling of  $\alpha$ -Synuclein applying a NaCl gradient and pulsed EFs. 200  $\mu$ M of  $\alpha$ -Synuclein solutions containing a gradient of NaCl from 0 up to 250 mM (a) without and (c) with the application of EFs. Mixtures of 50  $\mu$ M  $\alpha$ -Synuclein with 15% PEG8000 and NaCl range of 0–250 mM (b) without and (d) with the stimulus of EFs. All solutions are in 20 mM Tris–HCl buffer at pH 7.4 and containing 1 mM DTT. The DLS (purple circles) and DDLS (green rhombuses) signal intensities detected from each condition were plotted below the corresponding hydrodynamic radii graph.

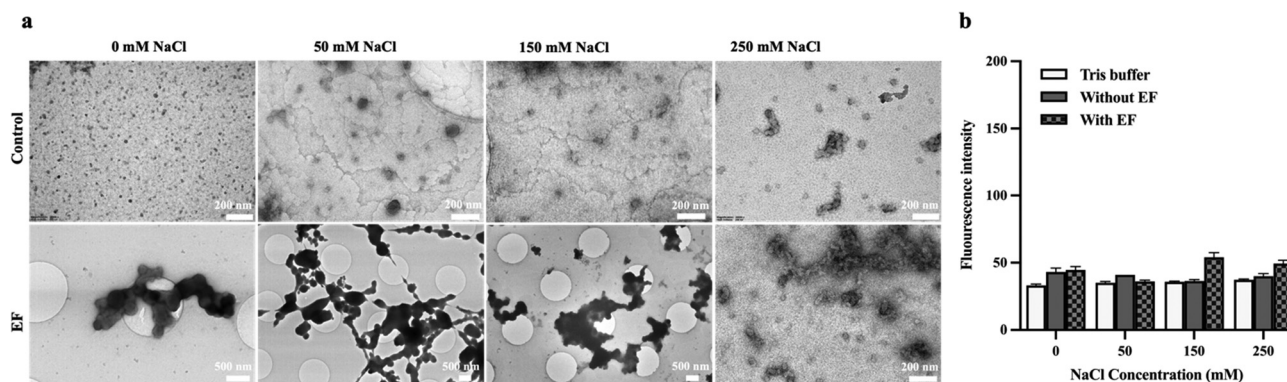


Fig. 3 (a) TEM images and (b) ThT fluorescence assays of ASN assemblies incubated at 20 °C for 3 days in solutions of 50  $\mu$ M ASN, 15% PEG8000, and a NaCl gradient in the absence (control) or being exposed for 2 hours by a pulsed electric field.

does not bind to non-polymerized amyloid peptides.<sup>28–30</sup> Therefore, 0.01% (w/v) CR was added to the solutions containing 50  $\mu$ M ASN and 15% PEG8000 to detect stacked  $\beta$ -sheet structure elements. As presented in ESI† Fig. S5a, monodisperse globular ASN assemblies showed the same colour as the surrounding solution. Nonetheless, the aggregated assemblies showed a more intensive colour of CR dye than the solvent, demonstrating the

presence of stacked  $\beta$  sheets inside the aggregated ASN assemblies. ESI† Fig. S5b displayed the CR staining results for the eight ASN samples prepared applying the same procedure as for the samples used for TEM and ThT assays. Except for globular ASN assemblies observed in the control group with solution conditions containing 50–250 mM NaCl, aggregated ASN assemblies formed in all other groups showed a strong binding of the CR



dye, revealing the formation of stacked  $\beta$  sheets within ASN assemblies.

After a continuous incubation of samples displayed in Fig. 2b and d for 30 days, mesoscopic globular ASN assemblies appeared to aggregate with each other particular in control groups having 0–50 mM NaCl in the solution and in all EF groups (Fig. 4a). Remarkably, the ordered arrangement of globular assemblies within the aggregated structure is particularly discernible in the control group at 50 mM NaCl and in the EF group containing 250 mM NaCl (Fig. 4a), which also exhibited relatively high fluorescence intensities applying the ThT assay (Fig. 4b). According to the DDLS results (Fig. 2), optical anisotropy was detected for early-stage ASN mesoscopic assemblies formed in the control group applying 50 mM NaCl and in the EF group applying 250 mM NaCl. Thus, we presume that the driving force for ASN mesoscopic assemblies attaching to each other to form larger aggregated structures with internal order might be attributed to the early-stage nucleation.

### Characterizing the thermostability of monomeric and assembled $\alpha$ -Synuclein

The thermostability of ASN monomers was analysed in solutions containing different NaCl concentrations (0, 50, 150, and 250 mM) along with a temperature ramp up (purple circles in Fig. 5) and subsequently ramp down (green circles). Results demonstrated that monomeric ASN with  $R_h$  of approx. 3.6 nm in solutions applying 150–250 mM NaCl is highly soluble in the temperature range of 20–70 °C (Fig. 5a). On the other hand, irreversible and stable ASN oligomerization was observed after the temperature ramp down in solutions containing 0–50 mM NaCl.

Mesoscopic ASN assemblies formed after 2 hour incubation in presence of NaCl and PEG8000 were also monitored in the solution along the temperature ramping (Fig. 5b) and demonstrated a temperature dependency in the presence of 0, 150, and 250 mM NaCl, which reveals weaker bonding forces of attraction among the ASN clusters. The reversible ability meets

well with the property of liquid dense clusters formed *via* LLPS, for which the kinetics is shown in Fig. 2b.

Further, highly thermostable ASN assemblies, formed in the presence of pulsed EFs during 2 hour incubation, were detected in the temperature ramp experiment applying all NaCl conditions, as mentioned before (Fig. 5c). Also, the thermostability observed for the mesoscopic assemblies of ASN containing 50 mM NaCl without applying EFs (Fig. 5b) corroborates well with the DDLS results and confirmed that changes in the optical properties of the colloidal material are related to the formation of a geometrically ordered molecular arrangement within ASN assemblies (Fig. 2b, 50 mM NaCl). In conclusion, ASN monomers are more thermostable at higher NaCl concentrations (150–250 mM), while ordered mesoscopic ASN assemblies are more resistant to higher temperature than the disordered DLCs. The regularization of the ACF fitting curves at different temperatures are shown for each condition in ESI† Fig. S6.

### Characterizing the autofluorescence effect of $\alpha$ -Synuclein assemblies

It is reported that the aromatic amino acid residues tyrosine, phenylalanine and tryptophan exhibit intrinsic fluorescence with both excitation and emission in the UV range of 260–280 nm.<sup>31</sup> However, amyloid fibrils specifically emit fluorescence in the visible spectra range of 400–450 nm because of the electron delocalization in the hydrogen-bond-rich network of fibrils.<sup>31–33</sup> It is also observed that dityrosine can emit fluorescence in the range of 400–420 nm upon excitation at 284 nm or 315 nm, due to noncovalent  $\pi$ - $\pi$  stacking between tyrosine residues.<sup>34</sup> ASN contains two phenylalanine and four tyrosine amino acids. Therefore, to avoid the contribution of aromatic amino acid residues to the autofluorescence intensity, we analysed the autofluorescence effect of ASN assemblies within the emission spectra range of 420–780 nm applying an excitation wavelength of 405 nm utilizing a confocal laser scanning microscopy (CLSM). The CLSM brightfield images (Fig. 6a) and autofluorescence images (Fig. 6b) showed early-stage morphologies of ASN assemblies formed in solutions within 2 hours at 20 °C.

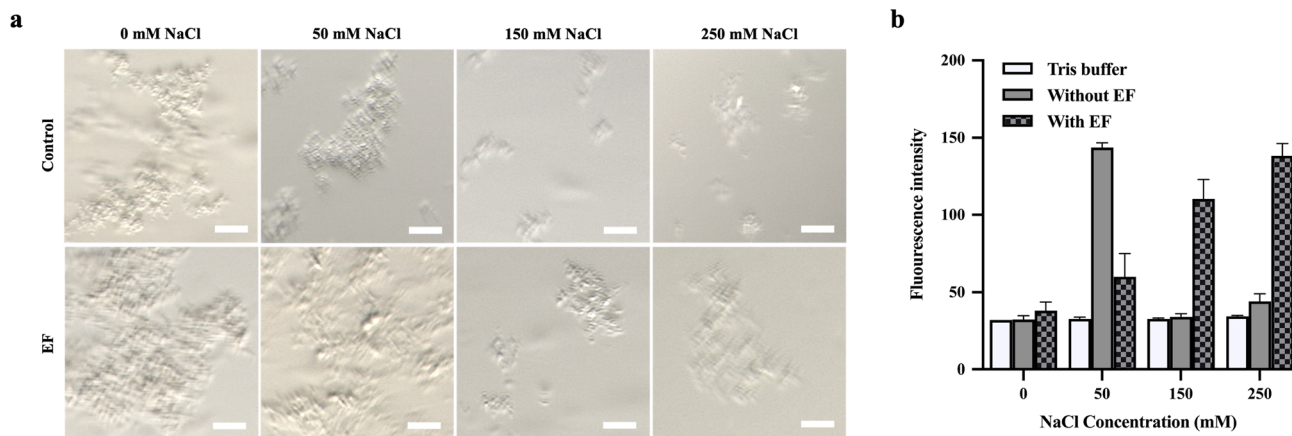


Fig. 4 (a) Optical brightfield microscopy images and (b) ThT fluorescence assays of 50  $\mu$ M  $\alpha$ -Synuclein incubated with 15% PEG8000 and applying a NaCl gradient for 30 days at 20 °C, in the absence (control) or being exposed for 2 hours by a pulsed EF. Scale bars correspond to 20  $\mu$ m.





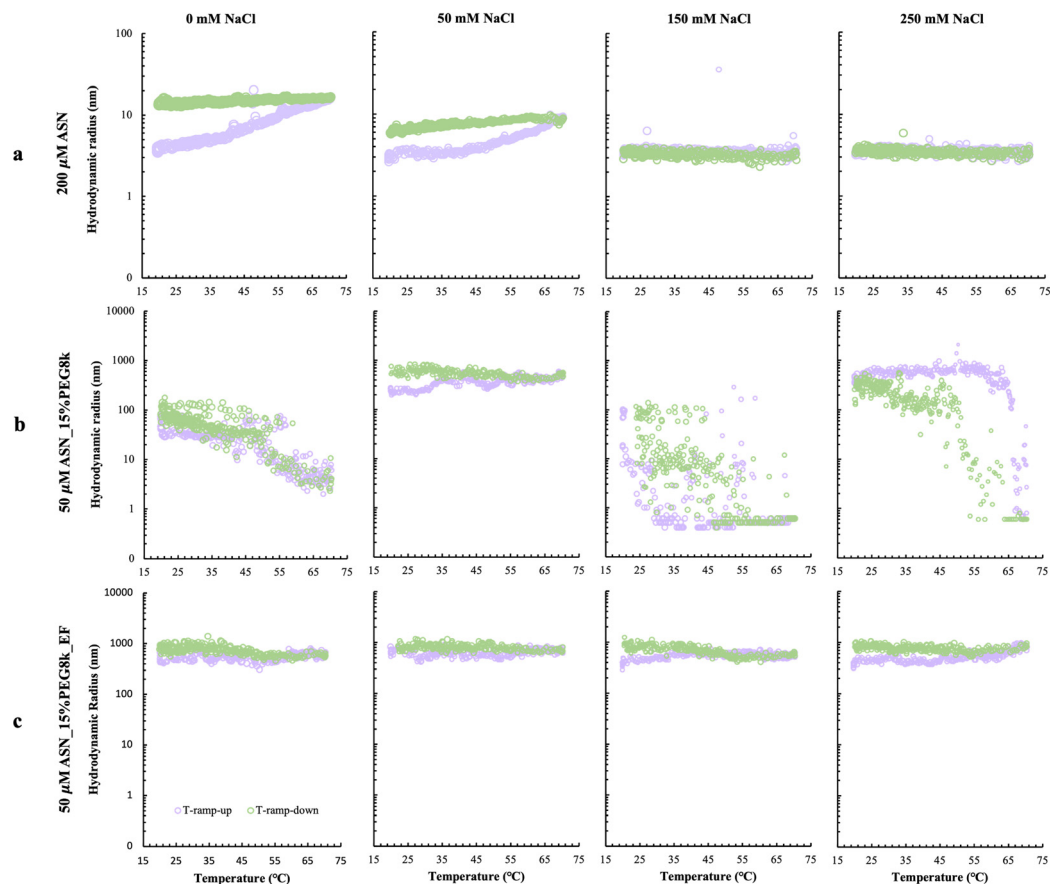


Fig. 5 The thermostability of (a) monomeric ASN, and the reversibility of assembled ASN induced by PEG8000 after 2 hours (b) without and (c) with a pulsed EF exposing to the solutions containing 20 mM Tris buffer pH 7.4 and a NaCl gradient.

Identical aforementioned conditions were applied in the presence and the absence (control group) of EFs. Consistent with TEM observations, mesoscopic ASN assemblies exhibited mainly monodisperse, globular, and relatively homogeneous dimension in the solution of the control group (upper rows of Fig. 6a and b), while under the effect of pulsed EFs the mesoscopic ASN assemblies packed up into an agglomerated arrangement (lower panels of Fig. 6a and b). The three-dimensional (3D) distribution of ASN assemblies in each solution were also analysed applying *in situ* 3D fluorescence scanning. The spatial distribution and the morphologies of ASN assemblies observed in the solution at different conditions are shown in ESI<sup>†</sup> Fig. S7.

The fluorescence emission spectra of ASN assemblies formed in the aforementioned conditions were also analysed. Results showed that mesoscopic ASN assemblies formed without applying EFs (control group) in all NaCl concentrations emitted a main peak with a maximum intensity at 470–490 nm, while the maximum emission spectrum of ASN assemblies, induced by pulsed EFs, presented a gradual red shift along with the increasing concentration of NaCl up to 250 mM (Fig. 6c). In the presence of EFs, applying 50 mM NaCl, a second minor peak at approx. 660 nm emerged in the spectrum and became more prominent at 150 mM NaCl, which two different electronic structures with emission spectrum peaks detected at 500 and 660 nm (Fig. 6c, 150 mM NaCl). Further, the maximum emission spectra of ASN assemblies

formed in the presence of 250 mM NaCl and EFs completely red-shifted the spectrum to the wavelength range of 680–700 nm. In other words, only changing ionic strength cannot alter the optical properties of ASN assemblies, however, an ionic gradient can assist EFs to induce assemblies with diverse secondary structures formed in the ASN agglomerates.

Efforts have been made to red-shift the emission wavelength for bioimaging applications, as longer emission wavelengths have less damage to cells and can minimize the background absorption.<sup>35</sup> Therefore, mesoscopic ASN assemblies with red-light autofluorescence are very prospective to be applied as label-free bioimaging markers. Grelich-Mucha and collaborators have revealed in 2021 that the arrangement of  $\beta$ -sheet structures and the resultant hydrogen-bond patterns influence the autofluorescence of fibrils by comparing the structural and optical properties of twisted and tapelike fibrils.<sup>36</sup> Therefore, based on the data obtained by DDLS measurements (Fig. 2b and d) and ThT assays (Fig. 3b), which showed the internal order rearrangement and the composition of  $\beta$ -sheet structures within ASN assemblies according to the rise of NaCl concentration and the presence of pulsed EFs, we deduce that the red-shifted emission spectra of ASN assemblies could be attributed to the increased composition of  $\beta$ -sheet stacks and hydrogen-bond networks within ASN assemblies. It's worth noticing that assemblies formed at 50 mM NaCl and in the absence of EFs



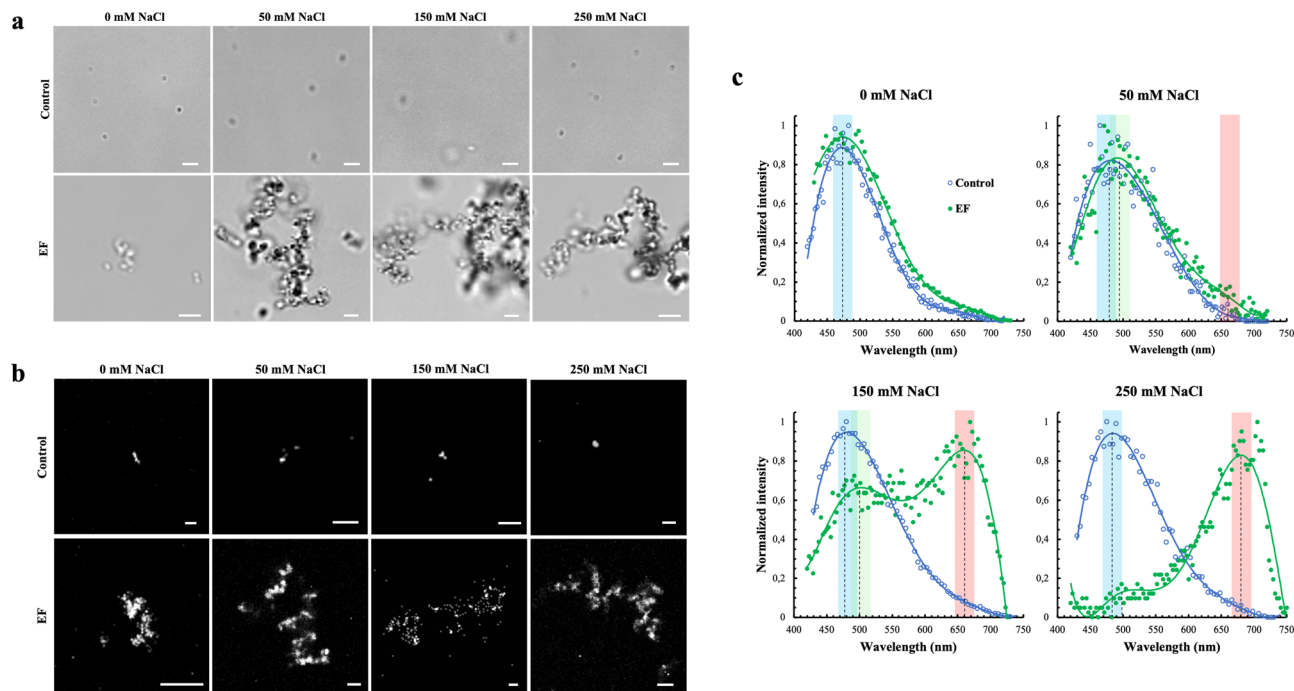


**Fig. 6** (a) CLSM bright-field images of ASN assemblies observed after 2-hour incubation of 50  $\mu\text{M}$  ASN with 15% PEG8000 in different NaCl solutions without (control group) or in presence of pulsed EFs at 20  $^{\circ}\text{C}$ . (b) The autofluorescence images and (c) corresponding normalized emission spectra upon excitation at 405 nm. Scale bars in figures a and b correspond to 2  $\mu\text{m}$ . Blue circular symbols and green dots in each graph of figure c are showing the experimental data of ASN samples without (control) and with EF treatment, respectively, the solid line is the corresponding fitting curve for each experimental data set.

did not show a clear redshift, although orientation-dependent interactions were detected by DDLs. The low ThT fluorescent intensity (Fig. 3b) and the light CR colour (ESI $^{\dagger}$  Fig. S5b) observed from ASN assemblies, incubated with 50 mM NaCl for 3 days, indicate that their internal molecular arrangement in early stages is different from the observed  $\beta$ -sheet structures induced by EFs.

#### Determination of the diffusion interaction parameter ( $K_D$ ) and the secondary structure of monomeric $\alpha$ -Synuclein

To understand the molecular mechanism resulting in the diverse behaviours of ASN described before, the diffusion interaction parameter- $K_D$  values and the secondary structure of ASN monomers were investigated.

**$K_D$  values.** The parameter  $K_D$  indicates the protein diffusion interactions and can be determined by analysing the dependence of the diffusion coefficient in context of the protein concentration in solution. Positive  $K_D$  value reveals a repulsive diffusion interaction while negative  $K_D$  value denotes an attractive interaction among protein monomers. To analyse the effect of different NaCl concentrations on the molecular diffusion interactions of ASN, the diffusion coefficient of monomeric ASN at different protein concentrations were measured by DLS in solutions with NaCl ranging from 0 to 250 mM.  $K_D$  value was determined, based on Equation 3, for each solution and is shown in Fig. 7. Monomeric ASN in all NaCl solutions presented a negative  $K_D$  value indicating attractive diffusion interactions, which is probably caused by the intrinsic disordered

structure of ASN. The ionic strength of 10 mM NaCl promoted the strongest attractive interaction among ASN monomers. Nonetheless, the increase of  $\text{Na}^+/\text{Cl}^-$  in the solution gradually raised the repulsive force and thus stabilized ASN molecules. This fact is also shown in Fig. 2a and 5a, since none ASN aggregation was observed in solutions with NaCl concentrations of 150 and 250 mM.

**The secondary structure.** The far-UV circular dichroism (CD) spectra of monomeric ASN in solutions containing 20 mM Tris buffer at pH 7.4 in the presence of a gradient of NaF were measured to study the ionic strength influence on the secondary structure of ASN. In this experiment NaCl was replaced by NaF because the chloride ions show strong absorption at wavelengths less than 195 nm. For each NaF concentration an ASN sample was pretreated by EFs for 1 hour and measured by CD to study the effect of EFs on the conformation of ASN. The full wavelength spectra (190–260 nm) of all ASN samples showed a main negative peak between 195 and 200 nm, which characterizes the secondary structure of random coils (Fig. 8a). A magnified view of the spectra of all samples in the range of 190 up to 210 nm exhibited a similar spectra profile with minor fluctuations in the region of the main peak, 195–200 nm. The only exception noticed was a second main peak maximum at a wavelength of 191–192 nm for a ASN solution containing 50 mM NaF without applying a pulsed EF (green dashed line in Fig. 8b).

After analysing the results described above, one question became nonnegligible: why 50 mM NaCl showed distinct effect on the conformation and phase behaviour of ASN although ASN



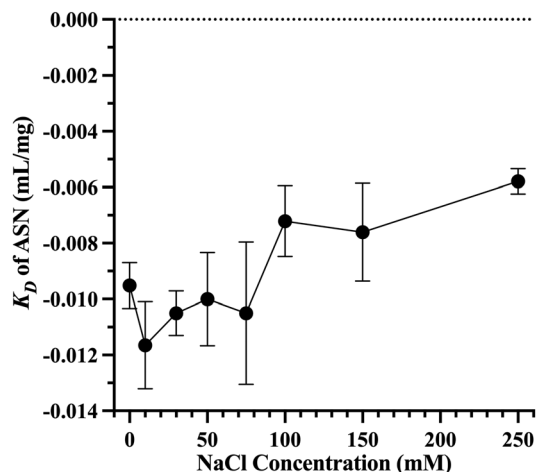


Fig. 7 The determined diffusion interaction parameter  $-K_D$  value of ASN in solutions with Tris buffer pH 7.4 and varied NaCl concentrations.

$K_D$  values at 0 and 50 mM NaCl are similar? Recently, Ubbiali *et al.* showed by applying cross-linking/mass spectrometry that the native ASN monomer can form a hairpin-like structure *via* the long-range interaction between the positively charged N-terminal region with the negatively charged C-terminal region, and can change to a more elongated structure after LLPS.<sup>37</sup> As an intrinsically disordered protein (IDP), ASN monomers can form intra- and inter-molecular interactions thus performing conformational transitions according to the environments. Based on our  $K_D$  results (Fig. 7), the intermolecular attraction of unfolded ASN induced by NaCl was maximum at 10 mM NaCl and gradually reduced upon increasing the NaCl concentration from 30 to 250 mM. Using the same methods, we have investigated previously the effect of NaCl on the diffusion interactions of the well folded protein glucose isomerase (GI) and showed that increasing NaCl within the range of 0–500 mM can constantly weaken the repulsive intermolecular interactions of GI.<sup>38</sup> Obviously, the charge screening effect of NaCl on unfolded ASN and well folded GI is

different because of the surface accessible regions of the protein. For well folded proteins, the monovalent ions mainly modulate the surface net charge thus the electrostatic interactions; But for unfolded IDPs, ions can access most of the protein domains to influence not only inter- but also intra-molecular interactions thus resulting in the conformational transition and the nonlinear dependence of the intermolecular interactions of ASN on ionic concentration (Fig. 7). We confirmed that the charge screening effect of 50 mM NaCl on ASN induced a specific conformation (Fig. 8) which favours protein–protein interactions towards the formation of ordered mesoscopic ASN assemblies (Fig. 2b) and  $\beta$ -sheet structure (Fig. 4). Based on those data, now we can also understand the different morphologies of ASN mesoscopic assemblies induced by EF at different NaCl conditions, as shown in Fig. 3a. Demonstrated by the DDLs results, shown in Fig. 2d, different internal ordering was detected for mesoscopic assemblies of ASN formed at different NaCl concentrations. ASN monomers can elongate to distinct conformations upon interacting and forming mesoscopic assemblies with different structures, as observed by TEM from ASN samples incubated for 3 days (Fig. 3a).

Another nonnegligible question came up from the observed phenomena is: why EF showed different influential trend on the later organization (Fig. 4a) and fibrillation level (Fig. 4b) of mesoscopic ASN assemblies induced at different NaCl concentrations? Recently, it was reported that the critical size of ASN oligomers/assemblies capable to form stable fibrils is approx. 40 nm.<sup>39</sup> Our data showed that ASN self-assemblies with  $R_h$  of approx. 46 nm formed at 50 mM NaCl within 2 hours (Fig. 2a, 50 mM NaCl) thereby revealed the interaction propensity of ASN towards fibrillation, which was subsequently validated by DDLs indicating significant internal order (Fig. 2b, 50 mM NaCl), higher thermostability (Fig. 5b, 50 mM NaCl), and stronger ThT fluorescence intensity (Fig. 4, 50 mM NaCl). On the other hand, the  $R_h$  (Fig. 2a and 5a, 150–250 mM NaCl) and lower  $K_D$  values (Fig. 7) unveiled that ASN monomers have relatively weak interactions at 150–250 mM NaCl, resulting in a smaller number of disordered ASN assemblies with lower

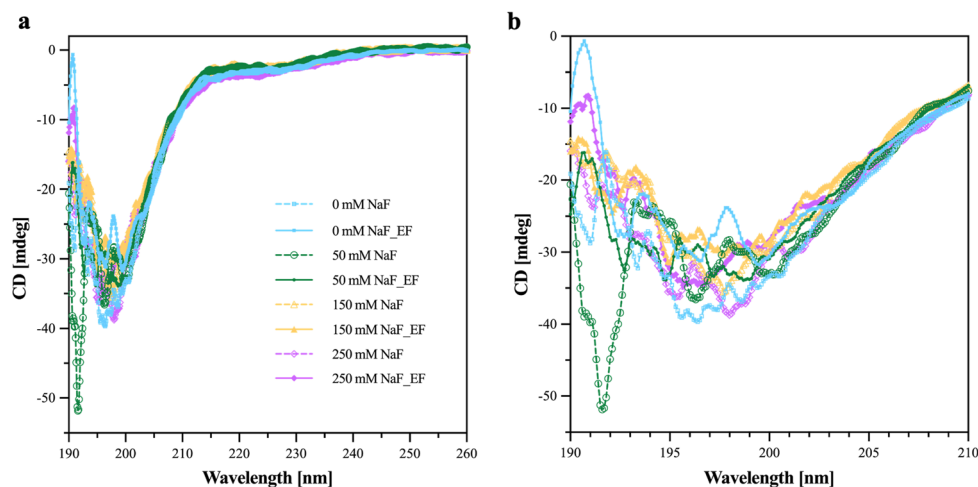


Fig. 8 The far-UV CD spectra of ASN ( $0.2 \text{ mg mL}^{-1}$ ) without and with the effect of EFs in solutions containing a gradient of NaF (0–250 mM). (a) The full-wavelength far-UV CD spectra of ASN. (b) Magnified view of the ASN CD spectra in the wavelength range of 190–210 nm.



thermostability (Fig. 2b and 5b, 150–250 mM NaCl). The effect of the applied EF on ASN organization was supported by increasing NaCl concentrations (Fig. 2, 4, and 6c). The only exception is that the optical anisotropy level of ASN mesoscopic assemblies formed at 50 mM NaCl and applying EF (DDLS signal intensities in Fig. 2d, 50 mM NaCl) and the later observed fibrillation (Fig. 4b, 50 mM NaCl) reduced compared to the corresponding control group. This can be explained by the CD results obtained (Fig. 8), as a specific conformational transition favouring fibrillation was induced by 50 mM NaCl, but was altered by EF. Thus, we conclude that the effect of pulsed EF on ASN assembling/fibrillation is reinforced by increasing the ionic strength, except for the case of particular conformational modulations induced by certain ionic concentrations.

## Conclusion

We investigated the kinetics and physicochemical properties of ASN assemblies applying PEG8000 as a crowding agent at pH 7.4. Results obtained confirmed that ASN tended to undergo LLPS and form DLCs in crowded environments at relative high protein concentrations ( $>100 \mu\text{M}$ ). However, it preferred to assemble oligomers or mesoscopic globular assemblies at low protein concentrations ( $<100 \mu\text{M}$ ). The early-stage evolution of the dimensions and the internal arrangement of ASN assemblies was monitored applying a series of NaCl solutions and utilizing the DLS/DDLS technique. We could demonstrate that the protein conformational transition and attractive diffusion interactions of monomeric ASN towards a simultaneous assembling and ordering process was triggered only at 50 mM NaCl. Further, the effect of pulsed EFs was investigated and proved to guide ASN assembling and ordering without influencing the protein secondary conformation but accelerating the  $\beta$ -sheet formation. Characterization of physicochemical properties showed in presence of 150 or 250 mM NaCl that the ASN monomers are thermostable and the PEG-induced ASN assemblies show tendency to dissolve and reassemble along with the temperature ramp up and down in a temperature range of 20–70 °C. Mesoscopic ASN assemblies formed at 50 mM NaCl or formed applying pulsed EFs were highly thermostable due to the probably more ordered organization of ASN molecules within the assemblies. More interestingly, pulsed EFs have proved to modify the autofluorescence effect of induced ASN assemblies by adjusting the molecular arrangement and extending the hydrogen-bond networks within assemblies. Especially, we discovered for the first time an extraordinary redshift at 700 nm emission wavelength detected from assemblies formed under the influence of a pulsed EF and applying 250 mM NaCl. Overall, the results presented provide experimental strategies to adjust the kinetics and physicochemical properties of ASN assemblies by applying a NaCl gradient and distinct pulsed EFs.

## Conflicts of interest

There are no conflicts to declare.

## Acknowledgements

The authors acknowledge financial support by the DFG – project ID BE1443/29-1, by the Cluster of Excellence ‘Advanced Imaging of Matter’ of the Deutsche Forschungsgemeinschaft (DFG) – EXC 2056 – project ID 390715994, BMBF *via* projects 05K19GU4 and 05K16GUA, and by the China Scholarship Council – project ID [2020]71. The TEM part of work was supported by the European XFEL GmbH, Schenefeld, Germany.

## References

- 1 M. M. Ouberaï, J. Wang, M. J. Swann, C. Galvagnion, T. Williams, C. M. Dobson and M. E. Welland, *J. Biol. Chem.*, 2013, **288**, 20883–20895.
- 2 B. Nuscher, F. Kamp, T. Mehnert, S. Odoy, C. Haass, P. J. Kahle and K. Beyer, *J. Biol. Chem.*, 2004, **279**, 21966–21975.
- 3 L. Krabben, A. Fassio, V. K. Bhatia, A. Pechstein, F. Onofri, M. Fadda, M. Messa, Y. Rao, O. Shupliakov, D. Stamou, F. Benfenati and V. Haucke, *J. Neurosci.*, 2011, **31**, 18149–18154.
- 4 J. T. Bendor, T. P. Logan and R. H. Edwards, *Neuron*, 2013, **79**, 1044–1066.
- 5 A. Zbinden, M. Pérez-Berlanga, P. De Rossi and M. Polymenidou, *Dev. Cell*, 2020, **55**, 45–68.
- 6 S. Krishnan, E. Y. Chi, S. J. Wood, B. S. Kendrick, C. Li, W. Garzon-Rodriguez, J. Wypych, T. W. Randolph, L. O. Narhi, A. L. Biere, M. Citron and J. F. Carpenter, *Biochemistry*, 2003, **42**, 829–837.
- 7 Y. J. Guo, H. Xiong, K. Chen, J. J. Zou and P. Lei, *Mol. Psychiatry*, 2022, **27**, 758–770.
- 8 L. M. A. Oliveira, T. Gasser, R. Edwards, M. Zweckstetter, R. Melki, L. Stefanis, H. A. Lashuel, D. Sulzer, K. Vekrellis, G. M. Halliday, J. J. Tomlinson, M. Schlossmacher, P. H. Jensen, J. Schulze-Hentrich, O. Riess, W. D. Hirst, O. El-Agnaf, B. Mollenhauer, P. Lansbury and T. F. Outeiro, *npj Parkinson's Dis.*, 2021, **7**, 65.
- 9 J.-H. Lee, D.-S. Yang, C. N. Goulbourne, E. Im, P. Stavrides, A. Pensalfini, H. Chan, C. Bouchet-Marquis, C. Bleiwas, M. J. Berg, C. Huo, J. Peddy, M. Pawlik, E. Levy, M. Rao, M. Staufenbiel and R. A. Nixon, *Nat. Neurosci.*, 2022, **25**, 688–701.
- 10 S. Ray, N. Singh, R. Kumar, K. Patel, S. Pandey, D. Datta, J. Mahato, R. Panigrahi, A. Navalkar, S. Mehra, L. Gadhe, D. Chatterjee, A. S. Sawner, S. Maiti, S. Bhatia, J. A. Gerez, A. Chowdhury, A. Kumar, R. Padinhateeri, R. Riek, G. Krishnamoorthy and S. K. Maji, *Nat. Chem.*, 2020, **12**, 705–716.
- 11 A. S. Sawner, S. Ray, P. Yadav, S. Mukherjee, R. Panigrahi, M. Poudyal, K. Patel, D. Ghosh, E. Kummerant, A. Kumar, R. Riek and S. K. Maji, *Biochemistry*, 2021, **60**, 3676–3696.
- 12 P. Alam, L. Bousset, R. Melki and D. E. Otzen, *J. Neurochem.*, 2019, **150**, 522–534.
- 13 T. M. Krygowski, *J. Chem. Inf. Comput. Sci.*, 1993, **33**, 70–78.
- 14 M. Tashiro, M. Kojima, H. Kihara, K. Kasai, T. Kamiyoshihara, K. Ueda and S. Shimotakahara, *Biochem. Biophys. Res. Commun.*, 2008, **369**, 910–914.





- 15 M. A. Saraiva, *Int. J. Biol. Macromol.*, 2021, **177**, 392–400.
- 16 K. A. Conway, S. J. Lee, J. C. Rochet, T. T. Ding, R. E. Williamson and P. T. Lansbury, *Proc. Natl. Acad. Sci. U. S. A.*, 2000, **97**, 571–576.
- 17 D. M. Walsh, A. Lomakin, G. B. Benedek, M. M. Condrón and D. B. Teplow, *J. Biol. Chem.*, 1997, **272**, 22364–22372.
- 18 R. Kaye, E. Head, J. L. Thompson, T. M. McIntire, S. C. Milton, C. W. Cotman and C. G. Glabe, *Science*, 2003, **300**, 486–489.
- 19 I. Benilova, E. Karran and B. De Strooper, *Nat. Neurosci.*, 2012, **15**, 349–357.
- 20 F. Hasecke, T. Miti, C. Perez, J. Barton, D. Schölzel, L. Gremer, C. S. R. Grüning, G. Matthews, G. Meisl, T. P. J. Knowles, D. Willbold, P. Neudecker, H. Heise, G. Ullah, W. Hoyer and M. Muschol, *Chem. Sci.*, 2018, **9**, 5937–5948.
- 21 G. P. Concepcion and E. A. Padlan, *Med. Hypotheses*, 2010, **74**, 27–28.
- 22 S. Ray, T. O. Mason, L. Boyens-Thiele, N. Jahnke and A. K. Buell, *BioRxiv*, 2022, 490467.
- 23 J. Berry, C. P. Brangwynne and M. Haataja, *Rep. Prog. Phys.*, 2018, **81**, 046601.
- 24 G. Madras and B. J. McCoy, *J. Chem. Phys.*, 2002, **117**, 8042–8049.
- 25 J. Stetefeld, S. A. McKenna and T. R. Patel, *Biophys. Rev.*, 2016, **8**, 409–427.
- 26 B. G. Wilhelm, S. Mandad, S. Truckenbrodt, K. Kröhnert, C. Schäfer, B. Rammner, S. J. Koo, G. A. Claßen, M. Krauss, V. Haucke, H. Urlaub and S. O. Rizzoli, *Science*, 2014, **344**, 1023–1028.
- 27 C. R. Bodner, C. M. Dobson and A. Bax, *J. Mol. Biol.*, 2009, **390**, 775–790.
- 28 E. I. Yakupova, L. G. Bobyleva, I. M. Vikhlyantsev and A. G. Bobylev, *Biosci. Rep.*, 2019, **39**, BSR20181415.
- 29 R. Khurana, V. N. Uversky, L. Nielsen and A. L. Fink, *J. Biol. Chem.*, 2001, **276**, 22715–22721.
- 30 B. Frieg, L. Gremer, H. Heise, D. Willbold and H. Gohlke, *Chem. Commun.*, 2020, **56**, 7589–7592.
- 31 C. W. Chung, A. D. Stephens, E. Ward, Y. Feng, M. J. Davis, C. F. Kaminski and G. S. Kaminski Schierle, *Anal. Chem.*, 2022, **94**, 5367–5374.
- 32 D. Pinotsi, L. Grisanti, P. Mahou, R. Gebauer, C. F. Kaminski, A. Hassanali and G. S. Kaminski Schierle, *J. Am. Chem. Soc.*, 2016, **138**, 3046–3057.
- 33 A. D. Stephens, M. N. Qaisrani, M. T. Ruggiero, G. D. Mirón, U. N. Morzan, M. C. González Lebrero, S. T. E. Jones, E. Poli, A. D. Bond, P. J. Woodhams, E. M. Kleist, L. Grisanti, R. Gebauer, J. A. Zeitler, D. Credgington, A. Hassanali and G. S. Kaminski Schierle, *Proc. Natl. Acad. Sci. U. S. A.*, 2021, **118**, e2020389118.
- 34 D. A. Malencik and S. R. Anderson, *Amino Acids*, 2003, **25**, 233–247.
- 35 R. A. Chica, M. M. Moore, B. D. Allen and S. L. Mayo, *Proc. Natl. Acad. Sci. U. S. A.*, 2010, **107**, 20257–20262.
- 36 M. Grelich-Mucha, A. M. Garcia, V. Torbeev, K. Ożga, Ł. Berlicki and J. Olesiak-Bañska, *J. Phys. Chem. B*, 2021, **125**, 5502–5510.
- 37 D. Ubbiali, M. Fratini, L. Piersimoni, C. H. Ihling, M. Kipping, I. Heilmann, C. Iacobucci and A. Sinz, *Angew. Chem.*, 2022, **134**, 1–6.
- 38 M. Wang, A. L. C. Barra, H. Brognaro and C. Betzel, *Crystals*, 2022, **12**, 437.
- 39 S. E. Sanchez, D. R. Whiten, G. Meisl, F. S. Ruggeri, E. Hidari and D. Klenerman, *ChemBioChem*, 2021, **22**, 2867–2871.
- 40 J. N. Rao, C. C. Jao, B. G. Hegde, R. Langen and T. S. Ulmer, *J. Am. Chem. Soc.*, 2010, **132**, 8657–8668.



## **6 Discussion and Conclusion**

### **6.1 Effect of EFs on well-folded proteins: Conformational transition, phase separation, nucleation, and crystallization**

#### **6.1.1 EFs influence the conformation of well-folded proteins**

As described before, a screening experiment applying distinctive pEFs to a solution of GI and other selected model proteins was performed firstly. This experiment aimed to observe how proteins with different parameters react to pEFs and which pulsed waveform is most evident and efficient for influencing protein LLPS. Due to secondary structure elements and the distribution of charged amino acids, most proteins have a non-zero electric dipole moment, which causes the reorientation of proteins upon applying an external electric field. After analysing the aggregation behaviour of proteins with distinct dipole moments and exposure to EFs, it was confirmed that proteins with higher dipole moments are more sensitive to the effect of pEFs. Results obtained by optical microscopy and CD measurements showed that the applied pEFs not only guided the orientation and motion of proteins in solution but also triggered conformational transitions, which changed protein phase behaviours consequently. Using computational simulations, Sinelnikova and co-workers investigated the changes in orientation and conformation of gas-phase proteins in time-dependent electric fields.<sup>145</sup> They found that a protein reorientation always occurred before the unfolding of protein structures, regardless of the strength of EFs. A minimum field strength of 0.5 V/nm and 45 V/nm is required to reorient proteins and break essential structural interactions, respectively.

#### **6.1.2 EFs modulate the morphologies of protein DLCs/aggregates formed via phase separation**

Regarding the spatial distributions, dimensions, and morphologies of protein DLCs, it was found that parallel EFs can guide proteins forming DLCs with identical spatial orientation and comparable morphologies regardless of the waveforms of pEF. In contrast, the pEFs generated by platinum (Pt) wires caused different spatial distribution modes of protein DLCs/aggregates in solutions, depending on the waveform applied (Fig.1 in publication 1). Compared to the DLCs formed with external pEFs, protein DLCs induced by the pEFs do not fuse with each other (Fig. 2 in publication 1), which can be attributed to the polarised ions distributions on the surface of protein DLCs, caused by the pEFs. Among all pEFs tested, one specific pEF generated by Pt wires and waveform 4 was discovered can induce homogeneous and micron-sized protein DLCs distributed in a solution evenly, which can phase transit to crystal nuclei

(Fig.2 c2-c3 and Fig.4 in publication 1). Kang and Platten analysed effects in lysozyme protein aggregates in response to an alternating current (AC) electric field.<sup>146</sup> They demonstrated that the external AC EFs can disintegrate, polarize, and reorientate the preformed protein aggregates. Therefore, using EFs of different configurations and waveforms can modify the dimensions, spatial distributions, and phase transitions of protein DLCs during or after formation.

### **6.1.3 Assembling and 3D-ordering kinetics of well-folded proteins can be accelerated by applying a pEF**

The distinctive pEF generated by Pt wires and waveform 4 was applied further to GI solutions, as shown in publication 2, to explore further how pEFs influence the assembling and 3D-ordering kinetics of proteins in different physicochemical environments. Firstly, it was confirmed that multivalent ions are more effective than monovalent ions in influencing protein phase behaviours, since multivalent ions can induce and form specific and non-specific interactions. In contrast, monovalent ions mainly affect the electrostatic interactions of proteins. As the second parameter investigated, pEF showed high efficacy in enhancing protein assembling kinetics and 3D-ordering in the presence of ions. The effect of pEFs on protein interactions can be weakened by adding a low amount of crowding agents to slow down the protein motions and can be reinforced by increasing the ionic strength of the solution. By adjusting experimental parameters of ionic strength, crowding agent concentration, and pEFs applied to the protein solution, I observed multiple nucleation pathways of GI by DLS/DDLS method.

### **6.1.4 Role of mesoscopic clusters in protein crystallization and the advantages of applying MOCs to optimize protein crystallization**

#### **Role of mesoscopic clusters in protein nucleation and crystallization**

Since the discovery of the two-step nucleation theory, it is well known that protein DLCs can support the system to overcome the energy barrier of nucleation, thus improving the crystallization process. Typical studies about the role of metastable and mesoscopic protein DLCs in nonclassical nucleation and growth of protein crystals were also reported by Sleutel and co-workers. They showed that mesoscopic DLCs can trigger a self-purifying cascade on the surfaces of crystals and can increase the protein nucleation rate significantly.<sup>147</sup> Further, using time-resolved cryo-TEM to follow the nucleation process of GI, they uncovered a kind of mesoscopic protein clusters acting not as precursors of nuclei formation. These mesoscopic



protein clusters already showed a degree of crystallinity and can attach with each other in orientations to drive further the nucleation events. Eventually, the different binding ways of these mesoscopic clusters result in crystal polymorphisms.<sup>148</sup> Recently, Sleutel's group demonstrated at the molecular resolution that mesoscopic GI clusters formed in the early stages already have the same lattice symmetry as observed for the mature GI crystals.<sup>149</sup>

In terms of my PhD research activities, I observed that nanosized protein clusters organizing within DLCs support the formation of crystal nuclei, as shown in Fig. 6-1. The protein molecules within the nanosized clusters may adjust the orientation to coordinate with the surrounding nanosized clusters, forming a more ordered alignment and a stable state as crystal nuclei. Questions about 1) whether the molecular alignments of all nanosized clusters within one DLC are the same at the beginning and 2) how the molecular alignment changes along with time still need to be explored further in the future at nanoscales applying also more advanced techniques, such as time-resolved TEM.

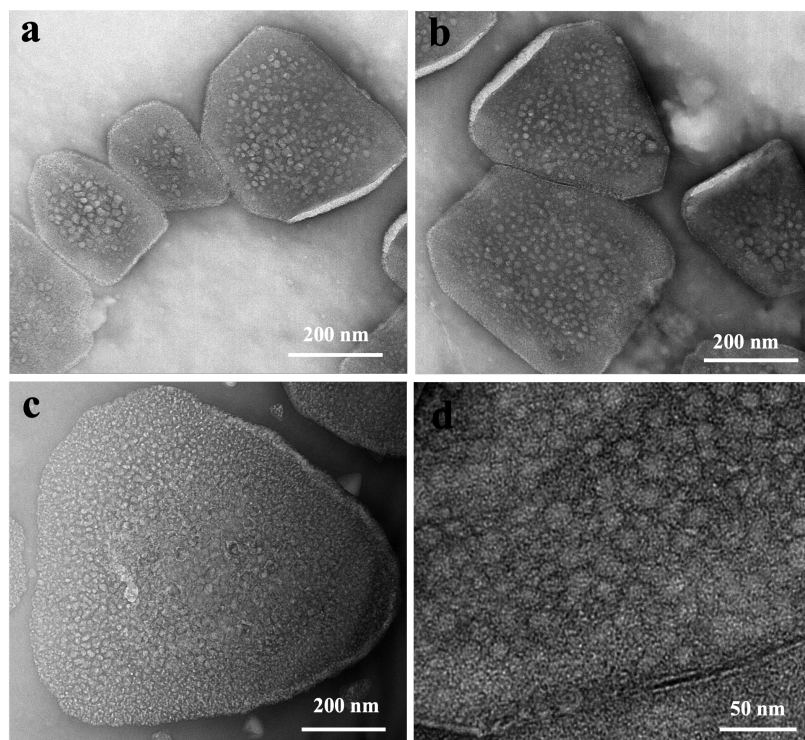


**Figure 6-1.** TEM images of GI crystal nuclei formed under the same condition as the pEF sample shown in the TEM results of publication 1.

The stacking behaviour of protein DLCs during the formation of protein crystals was also observed in this research work. GI crystals shown in Fig. 6-2 were formed after adding preformed MOCs at a rather low protein concentration of 2 mg/mL GI and a low ionic strength of 100 mM NaCl. The alignment and stacking of small clusters within one crystal are

pronounced as shown in figures 6-2a, 2d, 2g and 2h. Crystals in figures 6-2b, 2c, 2e, and 2f have parallel layers and edges, which can be attributed to the molecular reorientation and reorganization of all small clusters within one crystal. Remarkably, a remaining frame of the preliminarily formed crystals with the same structure as the final matured small crystals were also observed, as shown in Fig. 6-2i. The identical structure and orientation of the remaining old crystal frame with the final matured crystal also suggests a growth mechanism of crystals, that crystal tightens its structure with time from the out layer to the centre according to the crystal lattice formed at the early stages.

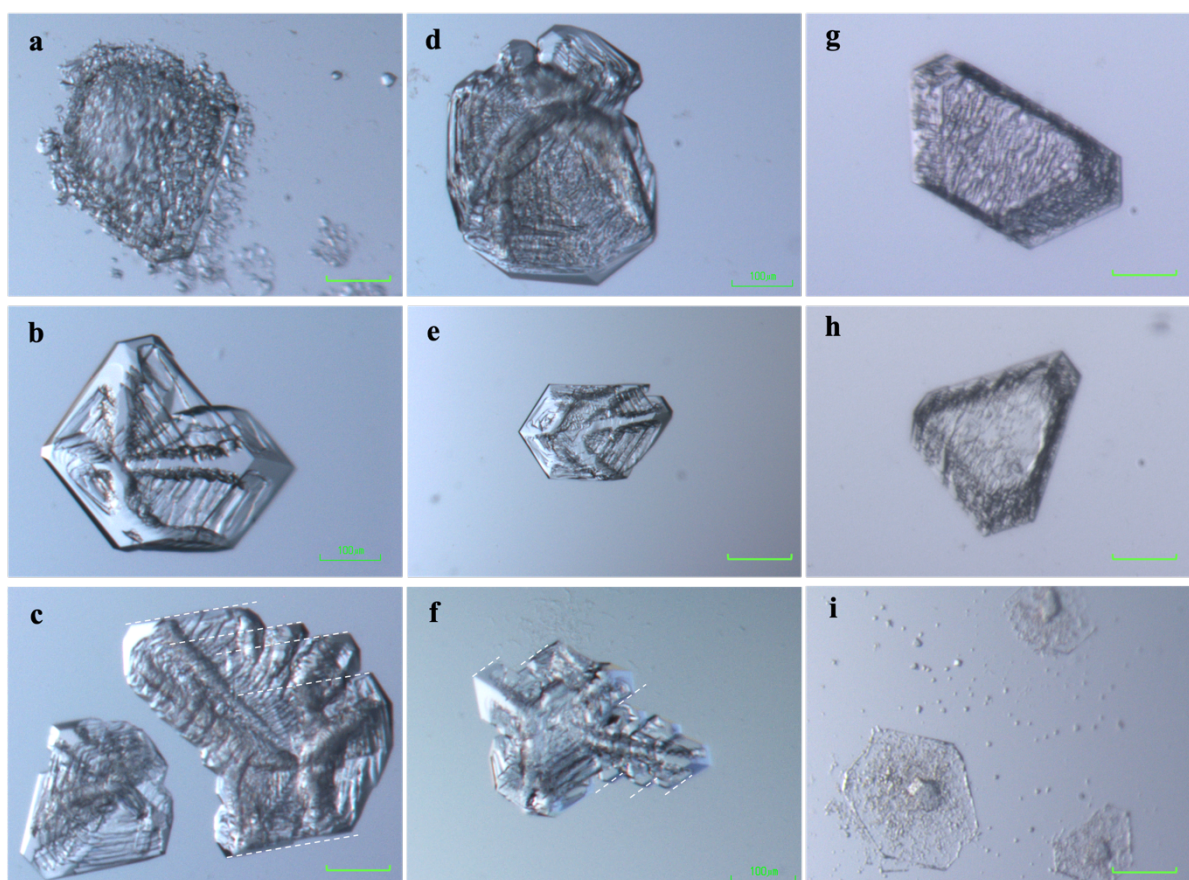


**Figure 6-2.** GI crystals observed in crystallization droplets containing (a-f) 2 mg/mL GI and 10% PEG20000, (g-i) 2 mg/mL GI and 8% PEG20000, incubated for 100 days at 20°C in a buffer of 10 mM MES pH 6.5 and 100 mM NaCl. Scale bars represent 100 µm. The preparation procedure of the crystallization droplets was the same, as for the crystallization droplets shown in Fig. 8 of publication 2.

### **Advantages of applying MOCs to optimize protein crystallization**

DLCs of different physicochemical properties can contribute differently to the later stages of phase transition. Metastable intermediates of protein DLCs can dissolve with time, while DLCs of high viscoelasticity can quench crystallization. The DLS/DDLS results presented in publication 2 (Fig. 4 and Fig. 6) showed that the phase separation and nucleation kinetics can be adjusted by changing the ionic strength and crowding agent conditions, which are traditional ways for screening experiments to obtain suitable crystallization conditions. However, these procedures consume a substantial amount of protein and chemical materials. I found that the application of pEFs can induce proteins to form homogeneous and mesoscopic ordered clusters (MOCs), which are proved to be stable and can be added to fresh crystallization solutions as seeds, to overcome the nucleation energy barrier and optimize the crystal amount and dimensions (Fig. 8 and Fig. 10 in publication 2). Both monomeric protein GI and the complex protein Pdx validated the efficient effect of distinctive pEFs on accelerating protein nucleation and the reproducible role of MOCs supporting protein crystallization. As shown in Fig. 6-3, homogenous MOCs can overcome the flaws existing in the traditional seeding method (Fig. 6-3a), which is normally achieved by crushing a large crystal to obtain a seed solution. Nonetheless, the quality and size of the crushed seeds is challenging to controlled, so the number and quality of crystals grown from those seeds are hardly guaranteed. It is also generally time-consuming to screen many conditions to identify suitable crystallization conditions before making crystal seeds. From the aspect of applying EFs to improve protein crystallization, instead of applying EFs directly to the crystallization solution (Fig. 6-3c), the advantage of using EFs to induce MOCs and then apply the EFs-induced MOCs as crystallization seeds is to avoid the possible effect of EFs on the native protein 3D structure.

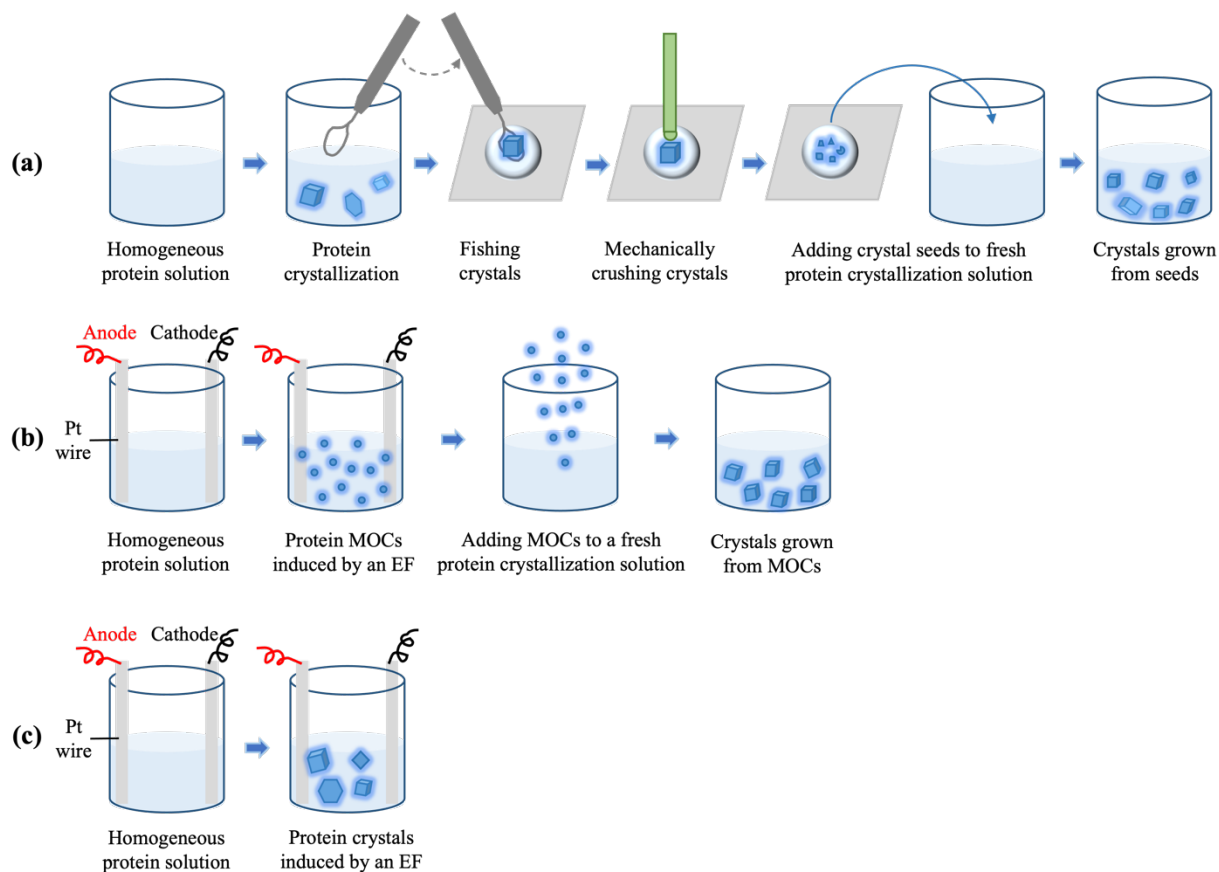


**Figure 6-3.** Comparisons of three different methods for optimizing protein crystallization. **(a)** The traditional seeding method in protein crystallization. **(b)** The seeding method established in this project by using EFs-induced and homogeneous MOCs as crystallization seeds. **(c)** The general way to use EFs to improve protein crystallization.

## 6.2 Effect of EFs on intrinsically disordered proteins: Conformational transition, phase separation, and fibrillation

To understand the effect of pulsed EFs and ions on the interaction and phase separation of IDPs leading to fibrillation, a Parkinson's disease-related protein ASN, was employed. It was confirmed that pulsed EF of waveform 4 can accelerate the assembling and ordering kinetics of IDPs with the presence of ions. It was also discovered that applying pulsed EF and altering NaCl concentration can modulate the physicochemical properties of intermediate ASN assemblies, such as the optical anisotropy, thermostability, and autofluorescence of mesoscopic ASN assemblies.

Compared to the well-folded protein GI, I found that the monovalent ions as  $\text{Na}^+/\text{Cl}^-$  can modulate not only molecular interactions but also cause conformational transitions of ASN (Fig. 7-8 of publication 3). This is probably because more protein domains in unfolded ASN

can be approached and affected by ions, as shown in Fig. 6-4. Thus, the relation between the electrostatic interaction strength of ASN and the ionic concentration is nonlinear. Dogan and collaborators investigated the binding mechanisms of IDPs/IDPRs and reported that the conformational changes of IDPs/IDPRs normally appear after the binding of IDPs/IDPRs, although sometimes particular secondary elements (such as helices) may form prior to the protein-protein interactions.<sup>150</sup> Using two oppositely charged IDPs, Berlow and Wright revealed that charge complementarity can enable IDPs binding tightly and reversibly, leading to an ensemble of protein complex conformations.<sup>151</sup> In the case of ASN, having a positively charged N-terminal and a negatively charged C-terminal region, the overall conformation can differ according to the long-range charge-charge interactions between the two regions. This results in a more complicated relationship between protein interaction and conformational changes considering the effect of ions. Applying cross-linking/mass spectrometry, Ubbiali *et al.* (2022) reported a hairpin-like structure of native ASN monomers, which can elongate after the formation of intermolecular interactions and LLPS.<sup>152</sup>

Among the conditions analysed for ASN, pEFs did not trigger a recognisable conformational change of ASN regardless of the ionic strengths in the protein solution. Only one NaCl concentration of 50 mM was identified by CD inducing an obvious conformational change, which triggered attractive interaction of ASN towards the formation of ordered mesoscopic assemblies and a faster fibrillation process than other salt conditions. Therefore, this work demonstrated that pEFs can modulate the interaction, assembly, and fibrillation of IDPs. This pEF-generated effect can be reinforced by increasing ionic strength, except for the certain ionic concentrations which can induce protein conformational changes.

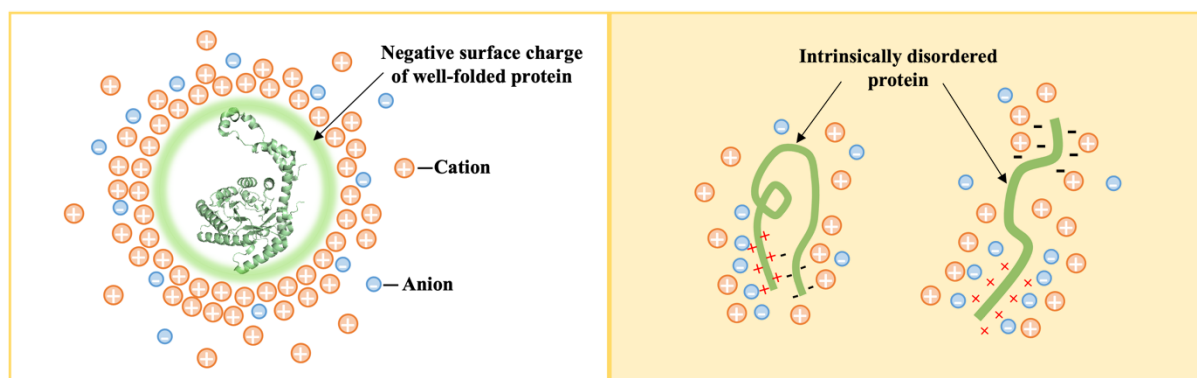


**Figure 6-4.** Schematic comparisons of the well-folded proteins and intrinsically disordered proteins (IDPs) in terms of the surface regions accessible to ions. The 3D cartoon structure representing the well-folded protein is from GI of *S. rubiginosus* (PDB code: 4ZB2).<sup>153</sup>

### 6.3 Conclusions and Prospects

In summary, this PhD thesis research focused on investigating the effect of physicochemical factors, specifically ionic strengths and pulsed EFs, on mesoscopic protein clusters' growth kinetics and dimensional properties. Additionally, parameters playing a key role in protein crystallization and fibrillation pathways were studied. The presented data contribute to the theoretical and practical knowledge and understanding of protein clusters and fibril formation. A comprehensive analysis of physicochemical scenarios and consideration of the various properties of the selected proteins provided new and additional insights into the processes involved in the formation of mesoscopic clusters for both well-folded and intrinsically disordered proteins. The experimental results provided an understanding of the molecular mechanisms underlying the effects of pEFs and ions on the phase behaviour of well-folded and intrinsically disordered proteins. Modulating the physical properties of protein clusters provided a deeper understanding of mesoscopic protein clusters and DLCs that play a crucial role in protein crystallization and fibrillation. In addition, multiple nucleation and crystal formation pathways were observed while investigating different crystallization conditions. Thus, this study enriches the experimental database required for understanding phase separation, self-assembly, and the nucleation process in proteins. The data obtained and presented also provide further knowledge for scientists in other fields to study LLPS, such as polymer science and pharmaceutical engineering. In terms of applications, the established and presented seeding method applying MOCs can enhance the efficiency and quality of protein crystallization experiments. This method was validated to be reproducible and universal for model and complex protein oligomers. The obtained results also can inspire the development of new physicochemical approaches to intervene in the LLPS, particularly LLPS involving in or causing diseases.

## 7 Bibliography

- 1 Y. Shin and C. P. Brangwynne, *Science*, 2017, **357**, 1253.
- 2 S. Kroschwald and S. Alberti, *Cell*, 2017, **168**, 947–948.
- 3 A. Boija, I. A. Klein, B. R. Sabari, A. Dall’Agnese, E. L. Coffey, A. V. Zamudio, C. H. Li, K. Shrinivas, J. C. Manteiga, N. M. Hannett, B. J. Abraham, L. K. Afeyan, Y. E. Guo, J. K. Rimel, C. B. Fant, J. Schuijers, T. I. Lee, D. J. Taatjes and R. A. Young, *Cell*, 2018, **175**, 1–14.
- 4 S. Qamar, G. Z. Wang, S. J. Randle, F. S. Ruggeri, J. A. Varela, J. Q. Lin, E. C. Phillips, A. Miyashita, D. Williams, F. Ströhl, W. Meadows, R. Ferry, V. J. Dardov, G. G. Tartaglia, L. A. Farrer, G. S. Kaminski Schierle, C. F. Kaminski, C. E. Holt, P. E. Fraser, G. Schmitt-Ulms, D. Klenerman, T. Knowles, M. Vendruscolo and P. St George-Hyslop, *Cell*, 2018, **173**, 720-734.e15.
- 5 H. Lu, D. Yu, A. S. Hansen, S. Ganguly, R. Liu, A. Heckert, X. Darzacq and Q. Zhou, *Nature*, 2018, **558**, 318–323.
- 6 M. Polymenidou, *Science*, 2018, **360**, 859–860.
- 7 T. M. Franzmann, M. Jahnel, A. Pozniakovsky, J. Mahamid, A. S. Holehouse, E. Nüske, D. Richter, W. Baumeister, S. W. Grill, R. V. Pappu, A. A. Hyman and S. Alberti, *Science*, 2018, **359**, eaao5654.
- 8 J. a Riback, C. D. Katanski, J. L. Kear-scott, V. Evgeny, A. E. Rojek, T. R. Sosnick and D. A. Drummond, *Cell*, 2018, **168**, 1028–1040.
- 9 P. Ball, *Cell. Mol. Biol.*, 2001, **47**, 717–720.
- 10 J. C. P. Renjie Chen, Erik Lascaris, *J. Chem. Phys.*, 2017, **146**, 234503.
- 11 W. L. Wang, Y. H. Wu, L. H. Li, W. Zhai, X. M. Zhang and B. Wei, *Sci. Rep.*, 2015, **5**, 1–10.
- 12 M. Muschol and F. Rosenberger, *J. Chem. Phys.*, 1997, **107**, 1953–1962.
- 13 T. Alber, F. C. Hartman, R. M. Johnson, G. A. Petsko and D. Tsernoglou, *J. Biol. Chem.*, 1981, **256**, 1356–1361.
- 14 O. Galkin and P. G. Vekilov, *Proc. Natl. Acad. Sci. U. S. A.*, 2000, **97**, 6277–81.
- 15 D. Vivarès, E. W. Kaler and A. M. Lenhoff, *Acta Crystallogr. Sect. D Biol. Crystallogr.*, 2005, **61**, 819–825.
- 16 C. C. de la Tour, *Ann. Chim. Phys.*, 1822, **21**, 127–132.
- 17 T. Andrews, *R. Soc.*, 1869, **159**, 575–590.
- 18 J. W. Gibbs, *Trans. Connect. Acad.*, 1873, **1**, 309–342.



- 19 J. W. Gibbs, *Trans. Connect. Acad.*, 1873, **2**, 382–404.
- 20 E. M. Courchaine, A. Lu and K. M. Neugebauer, *EMBO J.*, 2016, **35**, 1603–1612.
- 21 D. Zhao and J. Gao, *Philos. Trans. R. Soc. A Math. Phys. Eng. Sci.*, 2019, **377**, 20180207.
- 22 C. L. Heaysman, G. J. Philips, A. W. Lloyd and A. L. Lewis, *Acta Biomater.*, 2017, **53**, 190–198.
- 23 P. Kheddo, J. E. Bramham, R. J. Dearman, S. Uddin, C. F. Van Der Walle and A. P. Golovanov, *Mol. Pharm.*, 2017, **14**, 2852–2860.
- 24 C. Luebbert, F. Huxoll, G. Sadowski, G. Van Den Mooter and H. Grohgan, *Molecules*, 2017, **22**, 1–17.
- 25 M. J. Jackson, U. S. Kestur, M. A. Hussain and L. S. Taylor, *Mol. Pharm.*, 2016, **13**, 223–231.
- 26 P. Tipduangta, P. Belton, L. Fábíán, L. Y. Wang, H. Tang, M. Eddleston and S. Qi, *Mol. Pharm.*, 2016, **13**, 25–39.
- 27 A. S. Indulkar, Y. Gao, S. A. Raina, G. G. Z. Zhang and L. S. Taylor, *Mol. Pharm.*, 2016, **13**, 2059–2069.
- 28 D. Durgalakshmi and S. Balakumar, *Phys. Chem. Chem. Phys.*, 2015, **17**, 15316–15323.
- 29 S. E. Gilchrist, D. L. Rickard, K. Letchford, D. Needham and H. M. Burt, *Mol. Pharm.*, 2012, **9**, 1489–1501.
- 30 X. Lou, S. Munro and S. Wang, *Biomaterials*, 2004, **25**, 5071–5080.
- 31 C. L. T. Tanaka T, Ishimoto C, *Science*, 1977, **197**, 1010–1012.
- 32 C. P. Brangwynne, *Science*, 2009, **324**, 1729–1732.
- 33 A. Burgess, K. Shah, O. Hough and K. Hynynen, *Expert Rev Neurother*, 2015, **15**, 477–491.
- 34 D. M. Miller, R. Delgado, J. M. Chirgwin, S. C. Hardies and P. M. Horowitz, *J. Biol. Chem.*, 1991, **266**, 4686–4691.
- 35 M. Du and Z. J. Chen, *Science*, 2018, **361**, 704–709.
- 36 Y. Shin, Y. C. Chang, D. S. W. Lee, J. Berry, D. W. Sanders, P. Ronceray, N. S. Wingreen, M. Haataja and C. P. Brangwynne, *Cell*, 2018, **175**, 1481-1491.e13.
- 37 G. Zhang, Z. Wang, Z. Du and H. Zhang, *Cell*, 2018, **174**, 1–15.
- 38 A. Ablasser, *Science*, 2018, **361**, 646–647.
- 39 Y. Cheng, T. Legall, C. J. Oldfield, A. K. Dunker and V. N. Uversky, *Biochemistry*, 2006, **45**, 10448–10460.
- 40 V. N. Uversky, C. J. Oldfield and A. K. Dunker, *Annu. Rev. Biophys.*, 2008, **37**, 215–246.

- 41 A. C. J. Vladimirov, N. Uversky, Vrushank Davé, Lilia M. Iakoucheva, Prerna Malaney, Steven J. Metallo, Ravi Ramesh Pathak, *Chem Rev*, 2014, **114**, 6844–6879.
- 42 H. J. Kim, N. C. Kim, Y. Wang, E. A. Scarborough, Z. Diaz, K. S. Maclea, B. Freibaum, S. Li, A. P. Kanagaraj, R. Carter, K. B. Boylan, M. Aleksandra, R. Rademakers, J. L. Pinkus, S. A. Greenberg, Q. John, B. J. Traynor, B. N. Smith, S. Topp, A. Pestronk, Y. R. Li, A. F. Ford, A. D. Gitler, M. Benatar, O. D. King, V. E. Kimonis, E. D. Ross, C. C. Weihl, J. Shorter and J. P. Taylor, *Nature*, 2013, **495**, 467–473.
- 43 A. Aguzzi and M. Altmeyer, *Trends Cell Biol.*, 2016, **26**, 547–558.
- 44 Y. Liu, H. Hou, J. Li, Q.-D. Cheng, X. Zhang, X.-B. Zeng, A. Fiaz, B. Wang, C.-Y. Zhang, Q.-Q. Lu and D.-C. Yin, *Cryst. Growth Des.*, 2020, **20**, 1694–1705.
- 45 E. D. Zanotto and P. F. James, *J. Non. Cryst. Solids*, 1985, **74**, 373–394.
- 46 K. F. Kelton and A. L. Greer, *Phys. Rev. B*, 1988, **38**, 10089–10092.
- 47 J. F. Lutsko and M. A. Durán-Olivencia, *J. Chem. Phys.*, 2013, **138**, 244908.
- 48 J. Mosses, D. A. Turton, L. Lue, J. Sefcik and K. Wynne, *Chem. Commun.*, 2015, **51**, 1139–1142.
- 49 P. G. Vekilov, *Cryst. Growth Des.*, 2010, **10**, 5007–5019.
- 50 P. R. Ten Wolde and D. Frenkel, *Science*, 1997, **277**, 1975–1978.
- 51 D. Gebauer, M. Kellermeier, J. D. Gale, L. Bergström and H. Cölfen, *Chem. Soc. Rev.*, 2014, **43**, 2348–2371.
- 52 R. J. Collier, E. M. Westbrook, D. B. McKay and D. Eisenberg, *J. Biol. Chem.*, 1982, **257**, 5283–5285.
- 53 W. J. Ray and C. E. Bracker, *J. Cryst. Growth*, 1986, **76**, 562–576.
- 54 T. Albers, F. C. Hartmann, R. M. Johnson and G. A. Petsko, *J. Biol. Chem.*, 1981, **256**, 1356–1361.
- 55 P. G. Vekilov and A. R. Feinberg, *Acta Crystallogr. Sect. D Biol. Crystallogr.*, 2002, **58**, 1611–1616.
- 56 J. R. Savage and A. D. Dinsmore, *Phys. Rev. Lett.*, 2009, **102**, 15–18.
- 57 O. Galkin, W. Pan, L. Filobelo, R. E. Hirsch, R. L. Nagel and P. G. Vekilov, *Biophys. J.*, 2007, **93**, 902–913.
- 58 D. Gebauer, A. Völkel and H. Cölfen, *Science*, 2008, **322**, 1819–1822.
- 59 D. S. W. Lee, A. R. Strom and C. P. Brangwynne, *APL Bioeng.*, 2022, **6**, 21503.
- 60 E. Lacroix and T. E. Audas, *Front. Mol. Biosci.*, 2022, **9**, 1–17.
- 61 S. E. Liao and O. Regev, *Nucleic Acids Res.*, 2021, **49**, 636–645.
- 62 K. Ninomiya and T. Hirose, *Non-Coding RNA*, 2020, **6**, 6.

- 63 P. A and S. C. Weber, *Non-Coding RNA*, 2019, **5**, 50.
- 64 A. R. Strom and C. P. Brangwynne, *J. Cell Sci.*, 2019, **132**, jcs235093.
- 65 F. Erdel and K. Rippe, *Biophys. J.*, 2018, **114**, 2262–2270.
- 66 A. K. Tiwary and Y. Zheng, *Curr. Opin. Cell Biol.*, 2019, **60**, 92–98.
- 67 X. Liu, X. Liu, H. Wang, Z. Dou, K. Ruan, D. L. Hill, L. Li, Y. Shi and X. Yao, *J. Biol. Chem.*, 2020, **295**, 13419–13431.
- 68 C. So, S. Cheng and M. Schuh, *Trends Cell Biol.*, 2021, **31**, 254–268.
- 69 X. Jiang, D. B. T. Ho, K. Mahe, J. Mia, G. Sepulveda, M. Antkowiak, L. Jiang, S. Yamada and L.-E. Jao, *J. Cell Sci.*, 2021, **134**, jcs258897.
- 70 C. Roden and A. S. Gladfelter, *Nat. Rev. Mol. Cell Biol.*, 2021, **22**, 183–195.
- 71 R. Wagner, *Müller's Arch. Anat Physiol Wiss. Med*, 1835, **268**, 373–377.
- 72 W. W. B. Strome S, *Proc. Natl. Acad. Sci.*, 1982, **79**, 1558–1562.
- 73 S. Strome and W. B. Wood, *Cell*, 1983, **35**, 15–25.
- 74 J. T. Wang and G. Seydoux, *Curr Biol.*, 2016, **24**, R637–R638.
- 75 V. N. Uversky, *Adv. Colloid Interface Sci.*, 2017, **239**, 97–114.
- 76 T. Misteli and R. D. Phair, *Nature*, 2000, **404**, 604–609.
- 77 T. Pederson, *Cell*, 2001, **104**, 635–638.
- 78 A. H.-A. Hanieh Falahati, *R. Soc. Chem.*, 2019, **15**, 1135–1154.
- 79 J. Voigts, J. H. Siegle, D. L. Pritchett, C. I. Moore, A. G. Siapas, M. A. Wilson, R. Urioste, J. Hetke, K. Wise, A. Draguhn, R. D. Traub, D. Schmitz, J. G. Jefferys, J. M. Siegel, M. H. Kryger, T. Roth, W. C. Dement, D. J. Foster, M. A. Wilson, M. A. Wilson, B. L. Menaughton, J. Lu, D. Sherman, M. Devor, C. B. Saper, J. A. Hobson, R. W. Mccarley, P. W. Wyzinski, C. B. Saper, T. C. Chou, T. E. Scammell, C. B. Saper, T. E. Scammell, J. Lu, R. G. Northcutt, I. Timofeev, M. Steriade, D. R. Collins, J. G. Pelletier, J. Csicsvari, D. Buhl, M. Klinkmann, A. Arends, T. Manthey, C. Thum, F. Baier, T. Maurer and G. Schmalbach, *Science*, 2016, **352**, 595–600.
- 80 A. Vovk, C. Gu, M. G. Opferman, L. E. Kapinos, R. Y. H. Lim, R. D. Coalson, D. Jasnow and A. Zilman, *Elife*, 2016, **5**, 1–29.
- 81 R. P. Sarah Rauscher, *Elife*, 2017, **6**, 1–21.
- 82 J. B. Woodruff, B. Ferreira Gomes, P. O. Widlund, J. Mahamid, A. Honigmann and A. A. Hyman, *Cell*, 2017, **169**, 1066–1077.
- 83 A. R. Strom, A. V. Emelyanov, M. Mir, D. V. Fyodorov, X. Darzacq and G. H. Karpen, *Nature*, 2017, **547**, 241–245.
- 84 B. R. Sabari, A. Dall'Agnese, A. Bojja, I. A. Klein, E. L. Coffey, K. Shrinivas, B. J.

- Abraham, N. M. Hannett, A. V. Zamudio, J. C. Manteiga, C. H. Li, Y. E. Guo, D. S. Day, J. Schuijers, E. Vasile, S. Malik, D. Hnisz, T. I. Lee, I. I. Cisse, R. G. Roeder, P. A. Sharp, A. K. Chakraborty and R. A. Young, *Science*, 2018, **361**, eaar3958.
- 85 L. Latonen, *Front. Cell. Neurosci.*, 2019, **13**, 1–10.
- 86 A. Shakya and J. T. King, *Biophys. J.*, 2018, **115**, 1840–1847.
- 87 P. J. Godowski, D. Picard and K. R. Yamamoto, *Science*, 1988, **241**, 812–816.
- 88 C. Plaschka, K. Nozawa and P. Cramer, *J. Mol. Biol.*, 2016, **428**, 2569–2574.
- 89 N. Wang and C. Liu, *Curr. Opin. Genet. Dev.*, 2019, **55**, 59–65.
- 90 X. Fang, L. Wang, R. Ishikawa, Y. Li, M. Fiedler, F. Liu, G. Calder, B. Rowan, D. Weigel, P. Li and C. Dean, *Nature*, 2019, **569**, 265.
- 91 A. N. Lupas and J. Bassler, *Trends Biochem. Sci.*, 2017, **42**, 130–140.
- 92 C. P. Brangwynne, P. Tompa and R. V. Pappu, *Nat. Phys.*, 2015, **11**, 899–904.
- 93 C. J. Oldfield and A. K. Dunker, *Annu. Rev. Biochem.*, 2014, **83**, 553–584.
- 94 J. G. Olsen, K. Teilum and B. B. Kragelund, *Cell. Mol. Life Sci.*, 2017, **74**, 3175–3183.
- 95 P. Radivojac, L. M. Iakoucheva, C. J. Oldfield, Z. Obradovic, V. N. Uversky and A. K. Dunker, *Biophys. J.*, 2007, **92**, 1439–1456.
- 96 S. A. Fromm, J. Kamenz, E. R. Nöldeke, A. Neu, G. Zocher and R. Sprangers, *Angew. Chemie Int. Ed.*, 2014, **53**, 7354–7359.
- 97 R. V. Pappu, M. K. Rosen, S. Banjade, W. B. Peeples, Q. Wu and A. Mittal, *Proc. Natl. Acad. Sci.*, 2015, **112**, E6426–E6435.
- 98 J. Amaya, V. H. Ryan and N. L. Fawzi, *J. Biol. Chem.*, 2018, **293**, 19522–19531.
- 99 N. Gilks, N. Kedersha, M. Ayodele, L. Shen, G. Stoecklin, L. M. Dember and P. Anderson, *Mol. Biol. Cell*, 2004, **15**, 5383–5398.
- 100 S. C. Weber and C. P. Brangwynne, *Curr. Biol.*, 2015, **25**, 641–646.
- 101 A. Molliex, J. Temirov, J. Lee, H. J. Kim, T. Mittag, J. P. Taylor, A. Molliex, J. Temirov, J. Lee, M. Coughlin, A. P. Kanagaraj and H. J. Kim, *Cell*, 2015, **163**, 123–133.
- 102 P. Li, S. Banjade, H. Cheng, S. Kim, B. Chen, L. Guo, M. Llaguno, J. V Hollingsworth, D. S. King, S. F. Banani, P. S. Russo, Q. Jiang, B. T. Nixon and M. K. Rosen, *Nature*, 2012, **483**, 336–340.
- 103 J. A. Toretsky and P. E. Wright, *J. Cell Biol.*, 2014, **206**, 579–588.
- 104 T. E. Audas, D. E. Audas, M. D. Jacob, J. J. D. Ho, M. Khacho, M. Wang, J. K. Perera, C. Gardiner, C. A. Bennett, T. Head, O. N. Kryvenko, M. Jorda, S. Daunert, A. Malhotra, L. Trinkle-Mulcahy, M. L. Gonzalvo and S. Lee, *Dev. Cell*, 2016, **39**, 155–168.
- 105 L. Latonen, H. M. Moore, B. Bai, S. Jäämaa and M. Laiho, *Oncogene*, 2011, **30**, 790–

- 805.
- 106 C. O. E. Ishimoto, *Proc. Natl. Acad. Sci.*, 1979, **76**, 4414–4416.
- 107 J. I. Clark, F. J. Giblin, V. N. Reddy and G. B. Benedek, *Invest. Ophthalmol. Vis. Sci.*, 2018, **22**, 186–190.
- 108 G. B. Benedek, J. I. Clark, E. N. Serrallach, C. Y. Young, L. Mengel, T. Sauke, A. Bagg and K. Benedek, *Philos. Trans. R. Soc. A Math. Phys. Eng. Sci.*, 1979, **293**, 329–340.
- 109 J. I. Clark and D. Carper, *Proc. Natl. Acad. Sci. U. S. A.*, 1987, **84**, 122–5.
- 110 T. Tanaka and G. B. Benedek, *Invest. Ophthalmol. Vis. Sci.*, 2016, **14**, 449–456.
- 111 S. Elbaum-Garfinkle, *J. Biol. Chem.*, 2019, **294**, 7160–7168.
- 112 A. Zbinden, M. Pérez-Berlanga, P. De Rossi and M. Polymenidou, *Dev. Cell*, 2020, **55**, 45–68.
- 113 C. Mathieu, R. V Pappu and J. P. Taylor, *Science*, 2020, **370**, 56–60.
- 114 Y. Hayashi, L. K. Ford, L. Fioriti, L. McGurk and M. Zhang, *J. Neurosci.*, 2021, **41**, 834–844.
- 115 M. L. Sprunger and M. E. Jackrel, *Biomolecules*, 2021, **11**, 1014.
- 116 J. D. Forman-Kay, R. W. Kriwacki and G. Seydoux, *J. Mol. Biol.*, 2018, **430**, 4603–4606.
- 117 F. Chiti and C. M. Dobson, *Annu. Rev. Biochem.*, 2006, **75**, 333–366.
- 118 J. Shorter, *Cell*, 2017, **171**, 30–31.
- 119 A. Mukherjee and C. Soto, *Cold Spring Harb. Perspect. Med.*, 2017, **7**, a024315.
- 120 S. Maharana, J. Wang, D. K. Papadopoulos, D. Richter, A. Pozniakovsky, I. Poser, M. Bickle, S. Rizk, J. Guillén-boixet, T. M. Franzmann, M. Jahnel, L. Marrone, Y. Chang, J. Sternecker, P. Tomancak, A. A. Hyman and S. Alberti, *Mol. Biol.*, 2018, **921**, 918–921.
- 121 J. J. Bouchard, J. H. Otero, D. C. Scott, E. Szulc, E. W. Martin, N. Sabri, D. Granata, M. R. Marzahn, K. Lindorff-Larsen, X. Salvatella, B. A. Schulman and T. Mittag, *Mol. Cell*, 2018, **72**, 19-36.e8.
- 122 V. N. Uversky, *Front. Mol. Biosci.*, 2014, **1**, 1–24.
- 123 V. N. Uversky, C. J. Oldfield, U. Midic, H. Xie, B. Xue, S. Vucetic, L. M. Iakoucheva, Z. Obradovic and K. Dunker, *BMC Genomics*, 2009, **17**, 1–17.
- 124 V. N. Uversky, *Expert Rev Proteomics*, 2012, **7**, 543–564.
- 125 V. Pejaver, W. L. Hsu, F. Xin, A. K. Dunker, V. N. Uversky and P. Radivojac, *Protein Sci.*, 2014, **23**, 1077–1093.
- 126 P. Radivojac, V. Vacic, C. Haynes, R. R. Cocklin, A. Mohan, J. W. Heyen, M. G. Goebel

- and L. M. Iakoucheva, *Proteins*, 2011, **78**, 365–380.
- 127 A. Roque, I. Ponte and P. Suau, *Biochim. Biophys. Acta (BBA)-Gene Regul. Mech.*, 2015, **1859**, 444–454.
- 128 S. Li, L. M. Iakoucheva, S. D. Mooney and P. Radivojac, *Biocomput.2010*, 2009, 337–347.
- 129 J. J. Blaker, J. C. Knowles and R. M. Day, *Acta Biomater.*, 2008, **4**, 264–272.
- 130 M. Alhijaj, J. Bouman, N. Wellner, P. Belton and S. Qi, *Mol. Pharm.*, 2015, **12**, 4349–4362.
- 131 L. Bromberg, J. Rashba-step and T. Scott, *Biophys. J.*, 2005, **89**, 3424–3433.
- 132 M. Tan, P. Huang, M. Xia, P.-A. Fang, W. Zhong, M. McNeal, C. Wei, W. Jiang and X. Jiang, *J. Virol.*, 2011, **85**, 753–764.
- 133 M. Tan and X. Jiang, *Immunology*, 2012, **136**, 28–29.
- 134 E. E. Nelson and A. E. Guyer, *Virology*, 2012, **382**, 115–123.
- 135 A. S. Raut and D. S. Kalonia, *Mol. Pharm.*, 2016, **13**, 1431–1444.
- 136 N. Debnath, T. Kawaguchi, H. Das, S. Suzuki and W. Kumasaka, *Sci. Technol. Adv. Mater.*, 2018, **19**, 507–516.
- 137 G. Sazaki, A. Moreno and K. Nakajima, *J. Cryst. Growth*, 2004, **262**, 499–502.
- 138 G. Sazaki, H. Komatsu, T. Nakada, S. Miyashita and K. Watanabe, *J. Cryst. Growth*, 1997, **8**, 231–234.
- 139 D. Yin, *Prog. Cryst. Growth Charact. Mater.*, 2015, **61**, 1–26.
- 140 Z. Hammadi and S. Veessler, *Prog. Biophys. Mol. Biol.*, 2009, **101**, 38–44.
- 141 M. A. and N. I. Wakayama, *Acta Crystallogr. Sect. D Biol. Crystallogr.*, 2002, **58**, 1708–1710.
- 142 M. Wang, S. Falke, R. Schubert, K. Lorenzen, Q. Di Cheng, C. Exner, H. Brognaro, C. N. Mudogo and C. Betzel, *Soft Matter*, 2020, **16**, 8547–8553.
- 143 M. Wang, A. L. C. Barra, H. Brognaro and C. Betzel, *Crystals*, 2022, **12**, 437.
- 144 M. Wang, R. Thuenauer, R. Schubert, S. Gevorgyan, K. Lorenzen, H. Brognaro and C. Betzel, *Soft Matter*, 2023, **19**, 1363–1372.
- 145 A. Sinelnikova, T. Mandl, H. Agelii, O. Grånäs, E. G. Marklund, C. Caleman and E. De Santis, *Biophys. J.*, 2021, **120**, 3709–3717.
- 146 K. Kang and F. Platten, *Sci. Rep.*, 2022, **12**, 1–16.
- 147 M. Sleutel and A. E. S. Van Driessche, *Proc. Natl. Acad. Sci. U. S. A.*, 2014, **111**, E546–E553.
- 148 A. E. S. Van Driessche, N. Van Gerven, P. H. H. Bomans, R. R. M. Joosten, H. Friedrich,

- D. Gil-Carton, N. A. J. M. Sommerdijk and M. Sleutel, *Nature*, 2018, **556**, 89–94.
- 149 A. E. S. Van Driessche, W. L. Ling, G. Schoehn and M. Sleutel, *Proc. Natl. Acad. Sci. U. S. A.*, 2022, **119**, e2108674119.
- 150 J. Dogan, S. Gianni and P. Jemth, *Phys. Chem. Chem. Phys.*, 2014, **16**, 6323–6331.
- 151 R. B. Berlow and P. E. Wright, *Nature*, 2018, **555**, 37–38.
- 152 D. Ubbiali, M. Fratini, L. Piersimoni, C. H. Ihling, M. Kipping, I. Heilmann, C. Iacobucci and A. Sinz, *Angew. Chemie*, 2022, **134**, 1–6.
- 153 C. M. C. Lobley, J. Sandy, J. Sanchez-Weatherby, M. Mazzorana, T. Krojer, R. P. Nowak and T. L. Sorensen, *Acta Crystallogr. Sect. D Struct. Biol.*, 2016, **72**, 629–640.



## 8 Appendix

### 8.1 Amino acid sequence of full-length $\alpha$ -synuclein

MDVFMKGLSK<sup>10</sup> AKEGVVAAA<sup>20</sup>E KTKQGVAAEAA<sup>30</sup> GKTKEGVLYV<sup>40</sup> GSKTKEGVVH<sup>50</sup> GVATVAEKT<sup>60</sup>  
EQVTNVGGAV<sup>70</sup> VTGVTAVAQK<sup>80</sup> TVEGAGSIAA<sup>90</sup> ATGFVKKDQL<sup>100</sup> GKNEEGAPQE<sup>110</sup> GILEDMPVDP<sup>120</sup>  
DNEAYEMPSE<sup>130</sup> EGYQDYEPEA<sup>140</sup> ENLYFQG

Amino acid in black is the full-length (140 AA) amino acid sequence of Alpha-synuclein.

Amino acids in red represent the TEV cleavage site.

## 8.2 Protein List

Protein	Organism	Supplier	Mw (kDa)	Isoelectric point	Dipole moment (D)	Buffer
Glucose Isomerase	<i>Streptomyces rubiginosus</i>	Hampton Research (USA)	43.23	5.0	1082	10 mM MES, pH 6.5
Ovalbumin	<i>Gallus gallus</i>	Sigma (Germany)	42.86	5.19	1061	150 mM K <sub>2</sub> HPO <sub>4</sub> -KH <sub>2</sub> PO <sub>4</sub> , pH 7.4
BPTI	<i>Bovine</i>		6.5 (58aa)	10.5	941	50 mM NaAc, pH 4.5
β-lactoglobulin	<i>Bovine</i>		18.4	4.76	594	1×PBS, pH 7.4
Hemoglobin	<i>Bovine</i>		64.5 (tetramer)	6.8	201	50 mM Tris- HCl, pH 9.0
Pyridoxal 5-phosphate synthase complex (Pdx)	<i>Staphylococcus aureus</i>	In-house product	670.56	5.25	-	20 mM Tris-HCl, pH 8, 200 mM NaCl, 1 mM EDTA, 2 mM DTT and 10 mM L-glutamine
Alpha-synuclein	<i>Homo sapiens</i>		14.6	4.67	2764	20 mM Tris, pH 7.4

### 8.3 Instrumentations List

<b>Instrument</b>	<b>Type and Manufacturer</b>
DLS instrumentation	Spectrolight300 (XtalConcepts, Germany)
	Wyatt Mobius (Wyatt Technology, USA)
DDLS instrumentation	Development project (XtalConcepts, Germany)
CD-Spectrometer	JASCO-815 (Jasco, Japan)
Transmission electron microscope	Jeol JEM-2100 Plus (Jeol, Germany)
Glow discharge system	GloQube Plus (Quorum, UK)
Optical microscope	Microscope SZX12 with camera DP10 (Olympus, Japan)
	Leica M205C Microscope (Leica, Germany)
Confocal laser scanning microscope	SP8 (Leica, Germany)
TECAN plate reader	Infinite 200 PRO (Tecan Trading AG, Switzerland)
Pulsed electric field instrument	KWD-808 (Jiangsu, China)
Photospectrometry	Nanodrop ND-2000 (Thermo-Scientific, Germany)
Microbalance	Sartorius TE3102S (Sartorius, Germany)
pH Meter	SevenEasy (Mettler-Toledo, Switzerland)
SDS-PAGE	Four Gel Caster (SE275)
	EV 231 (Peqlab, Germany)
	SE260 Mighty Small II Deluxe Mini (Hoefer, US)
Incubator	RUMED 3001 (Rubarth, Germany)
	Heraeus B6120 (Heraeus, Germany)
Centrifuges	5415R/5415C/5804R/5810R MinispinPlus (Eppendorf, Germany)
	Thinky ARE-250 (Intertronics, UK)
Äkta purifier	Äkta purifier 900 (GE Healthcare, USA)

## 8.4 Chemical List

Chemical	Supplier	Hazard Statements	Precautionary Statements
Acetic acid	Chem- solute	H226, H314	P280, P305+351+338, P310
Acrylamide	Carl Roth	H301, H312, H315, H317, H319, H332, H340, H350, H361f, H372	P201, P280, P301+310, P305+351+338, P308+313
Ampicillin	Carl Roth	H334, H317	P280, P261, P302+352, P342+311
Ammonium sulphate	Carl Roth	-	-
Ammonium acetate	Carl Roth	-	-
Ammonium citrate	Carl Roth	H315, H319, H335	P261, P280, P302+P352, P305+P351+P338, P312, P403+P233, P501
Ammonium Persulfate (APS)	Carl Roth	H272, H302, H315, H317, H319, H334, H335	P280, P305+351+338, P302+352, P304+341, P342+311
Bromophenol blue	Applichem	-	-
Coomassie Brilliant Blue R250	Serva	-	-
Congo red	Sigma	H350, H361d	P201, P202, P280, P308 + P313, P405, P501
DTT	Applichem	H302, H315, H319, H335	P302+352, P305+351+338
Dipotassium hydrogen phosphate	Applichem	-	-
Disodium hydrogen phosphate	Applichem	-	-
Potassium dihydrogen phosphate	Applichem	-	-
Potassium chloride	Carl Roth	-	-
EDTA	Sigma	H319	P305+351+338
Ethanol	Carl Roth	H225	P210
Glutaraldehyde	Sigma	H301+H331, H314-H317, H334-H335, H400-H411	P221-P273-P280-P301+P310-P305+P351+P338-P310
L-Glutamine	Carl Roth	-	-
Glycerol	Sigma	-	-
Hydrochloric acid	Merck	H314, H335	P261, P280, P310, P305+351+338
IPTG	Sigma	-	-
Magnesium chloride	Carl Roth	-	-
MES	Carl Roth	-	-
PEG3500	Sigma	-	-
PEG4000	Sigma	-	-
PEG6000	Sigma	-	-
PEG8000	Sigma	-	-
PEG20000	Sigma	-	-
Paraffin oil	Applichem	-	-

Potassium thiocyanate (KSCN)	Carl Roth	H302+H312+H332, H412	P261, P280, P302+P352
Sodium chloride	Carl Roth	-	-
Sodium dihydrogen phosphate	Applichem	-	-
Sodium fluoride	Sigma	-	-
Sodium hydroxide	Merck	H314	P280, P310, P305+351+338
SDS	Sigma	H228, H302, H311, H315, H319, H335	P210, P261, P280, P312, P305+351+338
Streptomycin sulphate			
Tris	Sigma	H315, H319, H335	P261, P305+351+338
TEMED	Merck	H225, H302, H314, H332	P261, P280, P305+351+338
Thioflavin T	Sigma	H301, H317, H318, H319, H400, H410, H411	P261, P264, P264+P265, P270, P272, P273, P280, P301+P316, P302+P352, P305+P351+P338, P305+P354+P338, P317, P321, P330, P333+P313, P337+P317, P362+P364, P391, P405, P501
Uranyl acetate	Ted Pella	H300+H330, H373, H411	P260, P264, P270, P271, P273, P284, P301 + P310, P304 + P340, P310, P320, P330, P391, P403 + P233, P405, P501
Yeast Extract	Serva	-	-

## **8.5 Supplementary Information-Pulsed electric fields induce modulation of protein liquid-liquid phase separation (LLPS)**

## SUPPLEMENTARY INFORMATION

### Preparation of protein solutions

Glucose Isomerase (GI) from *Streptomyces rubiginosus* was purchased from Hampton Research (USA). Ovalbumin from *Gallus gallus*,  $\beta$ -lactoglobulin and hemoglobin from *Bovine* and bovine pancreatic trypsin inhibitor (BPTI) were purchased from Sigma (Germany). These proteins were selected according to the individual dipole moment, which was calculated using the Protein Dipole Moments Server<sup>1</sup>. The unit of the dipole moment is Debye (D, 1 D=1 $\times$ 10<sup>-18</sup> statC·cm). All buffers and precipitant solutions (SI Table 1) were filtered through a 0.2  $\mu$ m or 0.45  $\mu$ m filter (SARSTEDT, Germany). Protein solutions were centrifuged for 60 minutes at 16000  $\times$  g and 4  $^{\circ}$ C before use. Concentrations were measured applying a Nanodrop ND-2000 (Thermo-Scientific, Germany).

**Table 1. Solution conditions and molecular parameters of proteins and precipitants**

Protein	Glucose Isomerase	Ovalbumin	BPTI	$\beta$ -lactoglobulin	Hemoglobin
Dipole moment (D)	1082	1061	941	594	201
Mw (kDa)	43.23	42.86	6.5 (58aa)	18.4	64.5 (tetramer)
Isoelectric point	5.0	5.19	10.5	4.76	6.8
Protein buffer	10 mM MES pH 6.5, 500 mM NaCl	150 mM K <sub>2</sub> HPO <sub>4</sub> -KH <sub>2</sub> PO <sub>4</sub> pH 7.4	50 mM NaAc pH 4.5	1 $\times$ PBS pH 7.4	50 mM Tris-HCl pH 9.0
Initial concentration of protein solution (mg/ml)	27	50	40	25	50
Precipitant	12% PEG 20000	3 M (NH <sub>4</sub> ) <sub>2</sub> SO <sub>4</sub>	700 mM KSCN	25% PEG 3350	9% PEG 6000
Mixing ratio	1:1	1:1	1:1	1:1	1:1

### Setups for producing pulsed electric fields

Two EF setups were assembled to apply pulsed electric fields (EFs) to protein suspensions. The one shown in SI Fig. 1a, is platinum (Pt) wire EF setup, consisted of a rectangular plastic piece in the middle with a round cell covered by two rectangular glass plates and two inserted Pt wires with 0.3 mm diameter, 1.5 cm length and a resistance of approx. 22.5 m $\Omega$  at 20  $^{\circ}$ C (Sigma, Germany). The other one shown in SI Fig. 1b, called parallel conductive glass (PCG) EF setup, consisted of a rectangular plastic piece in the middle with a round cell covered by two rectangular conductive glasses, which are indium tin oxide (ITO) coated with dimensions of 2 cm  $\times$  2 cm and a surface resistance of 3.2-4.8 m $\Omega$  (Sigma, Germany). The ITO coated surfaces of the two glass plates were positioned inwards and facing towards each other. The sample container capacity of each EF setup is approximately 45  $\mu$ l. The setup was connected to a KWD-808 instrument (Jiangsu, China) which can generate defined pulsed electric fields, as shown in SI Fig.1c. The pulse-width ( $\tau$ ) of the basic waveform component in each waveform was 0.6 $\pm$ 0.15 ms. The maximum pulse amplitude in each waveform outputted on 500  $\Omega$  load ( $V_{\max-500\Omega}$ ) during this experiment was 20 V. Waveform 1 is composed of equidistant identical pulses. In the waveform 2, bunches of rectangular pulses alternately appeared at high frequency and low frequency. Rectangular pulses appeared in the first half period of waveform 3 with a uniform amplitude, but no pulses output in the second half period. The pulse amplitude of the pulse in the waveform 4 rises up in the first half period and falls down with identical pulses in the second half period. In the waveform 5, the amplitude of the basic pulse rises up in the first half pulse pattern period with no output pulse in the second half period.



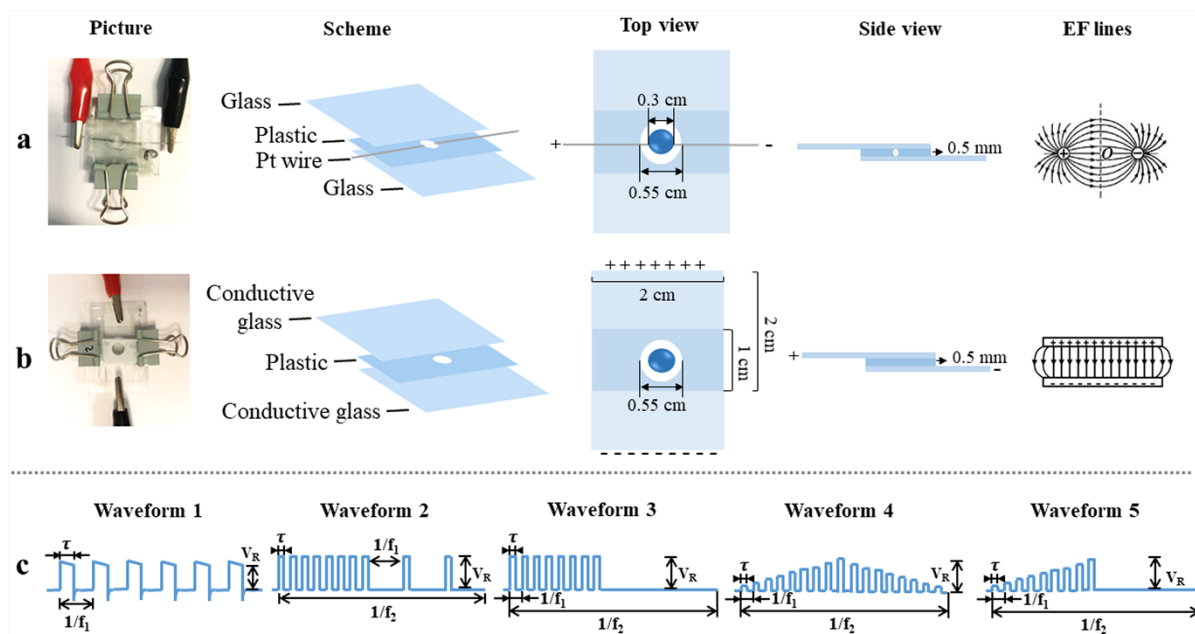


**Figure 1** Scheme and photographic pictures of (a) the Pt EF setup and (b) the PCG EF setup. The direction and distribution of corresponding EF lines to each EF setup is shown in the left bottom of each scheme. (c) Diagrams of five EF waveforms, the maximum output pulse amplitude ( $V_R$ ) depends on the resistance ( $R$ ) of the load.

## Methods and experimental setup applied to monitor protein LLPS applying optical microscopy

Droplets with 1:1 protein to precipitant volume ratio and a total volume of 3  $\mu\text{L}$  were sealed with two glass cover slides. Then, they were subsequently exposed to EFs and monitored over time by a Leica M205C Microscope with an adapted cold light source. Glucose isomerase (GI), ovalbumin, bovine pancreatic trypsin inhibitor (BPTI) and  $\beta$ -lactoglobulin shown in SI Table 1 were selected and investigated applying five different EF waveforms ( $V_{\text{max-500}\Omega}=20$  V) with the Pt EF and the PCG EF setup, respectively. Conditions of protein solutions and corresponding precipitants used for the experiments are summarized in SI Table 1. To evaluate the morphologies of LDCs nearby the anode and nearby the cathode of the PCG EF setup, the pictures were recorded from the anode side (+) and the cathode side (-), respectively, by turning the PCG EF setup upwards.

## Polarized and depolarized dynamic light scattering (DLS/DDLS) experiments

To study the dynamic assembly and the internal order of protein liquid dense clusters applying DLS and DDLS, an instrument providing a laser wavelength of 532 nm and a laser output power of 100 mW was utilized (SI Fig. 2. XtalConcepts, Germany). The instrument allows to acquire parallel DLS and DDLS measurements, each data acquisition of which was for 20 s with 120 s waiting time performed at 20  $^{\circ}\text{C}$ . The appropriate viscosity values were considered to calculate the hydrodynamic radii. A transparent cuvette (101.015-QS, Hellma Analytics, Germany), with 3 mm  $\times$  3 mm inner cross-section and 21 mm height was used as the sample container. As shown in SI Fig. 2, two Pt wires were inserted at two opposite corners of the cuvette to generate electric fields. In preparation, 20  $\mu\text{L}$  of GI solution at 7.5 mg/ml was mixed with 20  $\mu\text{L}$  of 12% PEG 20000 and pipetted into a cuvette. The sealed cuvette was placed in the cuvette holder of the DDLS instrument and an EF with waveform 4 ( $V_{\text{max-500}\Omega}=20$  V) was applied up to 5 h.

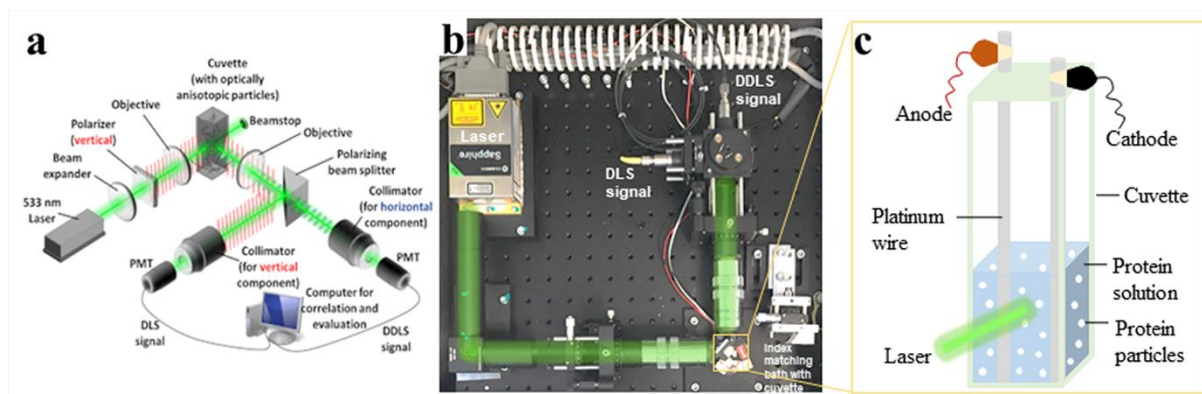


**Figure 2** (a) Schematic<sup>2</sup> and (b) photographic representation of the DDLS instrument. (c) Scheme of the cuvette used for the DDLS experiments with two Pt wires.

### Sample preparation for Transmission Electron Microscopy

A volume of 2  $\mu\text{l}$  of GI protein solution was mixed with 2  $\mu\text{l}$  of 12% (w/v) PEG 20000 in the platinum wire EF setup and treated with waveform 4 ( $V_{\text{max-500}\Omega}=20\text{ V}$ ) for 5 hours. Subsequently, the sample was centrifuged at  $3000 \times g$  for 5 minutes to separate GI LDCs. The supernatant was exchanged with 10  $\mu\text{l}$  12% PEG 20000 and centrifuged for 5 minutes at  $3000 \times g$  and  $20\text{ }^\circ\text{C}$ . The supernatant was exchanged with 20  $\mu\text{l}$  cross-linking solution (5 mM MES pH6.5, 250 mM NaCl, 6 % PEG 20000 and 2.5 % (v/v) glutaraldehyde), which was mixed with LDCs gently then incubated at  $20\text{ }^\circ\text{C}$  for 48 h to stabilize LDCs. After incubation the cross-linked sample was again centrifuged at the same conditions and the supernatant was replaced with 10  $\mu\text{l}$  of ultrapure water to wash out most of the buffer components after another centrifugation step. Finally, the LDCs were resuspended in 5-10  $\mu\text{l}$  fresh ultrapure water (depending on the amount of LDCs pellets) for negative staining to increase the contrast of LDCs. For negative staining, a carbon coated 3.05 mm copper grid (300 mesh) (PLANO GmbH, Germany) was used. Before loading the sample, the grid was glow-discharged for 30 s at 25 mV (GloQube Plus, Quorum). The respective sample solution was pipetted onto the grid and blotted with Whatman paper after 30 s, followed by two times grid washing with 10  $\mu\text{l}$  ultrapure water. For staining, 10  $\mu\text{l}$  of 2 % (w/v) uranyl acetate in ultrapure water was used and pipetted onto the grid. Afterwards the grid was incubated on the droplet surface for 30 s, the uranyl acetate liquid was blotted with Whatman paper and finally the grid was dried on the Whatman paper. A Jeol JEM-2100 Plus transmission electron microscope operated at 200 keV was used for the imaging experiments.

### Methods and experimental procedure of Circular dichroism spectrum

CD spectroscopy was applied to investigate the secondary structure content of selected proteins with distinct solvents composition under different EF conditions using a JASCO-815 spectropolarimeter (JASCO, Japan), applying in parallel EFs with five different pulse waveforms, respectively. For experiments 100  $\mu\text{L}$  protein solution at a concentration of 0.2 mg/ml was pipetted into a microplate (PolySorp F8-Wells Nunc-Immuno Module, VWR, Germany) with two Pt wire- electrodes attached to expose protein samples with five pulsed waveforms ( $V_{\text{max-500}\Omega}=20\text{ V}$ ), respectively. After 1 hour of exposure, the protein samples were transferred to a quartz cuvette with 1 mm path length (Hellma-Analytische, Germany). Protein solutions used for all groups were prepared in one tube to keep the same protein concentration. CD measurements were averaged over 10 individual spectra, recorded within a wavelength range of 260 - 190 nm, with a scanning speed of 100 nm/min and a bandwidth of 1 nm. The spectra were evaluated by the Software Spectra Manager from JASCO.

## Supplementary Figures

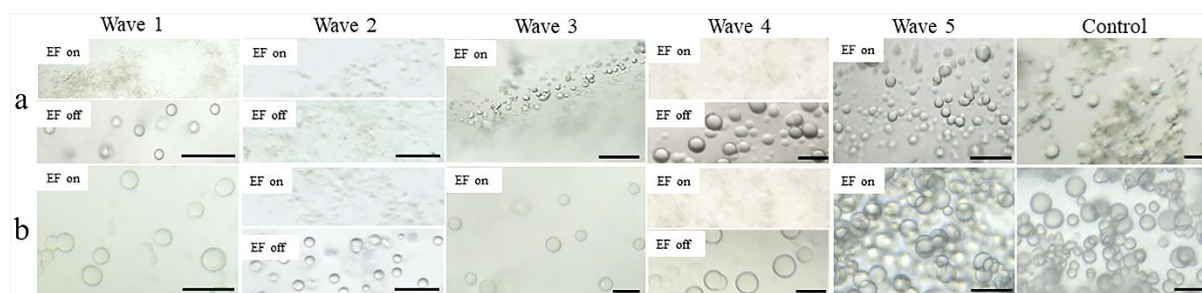


**Figure 3** LDCs of ovalbumin formed with (a) the Pt EF setup and (b) the PCG EF setup. The dimensions of LDCs formed with Pt EFs are smaller compared to those formed with PCG EFs when applying waveforms 3 and 5. The phase separation was hindered when EFs of waveforms 1, 2, and 4 were applied and reversible when EFs with the waveforms 1, 4 and PCG EF with waveform 2 were switched off. Irreversibility was observed for waveform 2 of the Pt EF setup. This observation is probably explained by the high frequency and average pulse amplitude of waveform 2. The scale bars correspond all to 25  $\mu\text{m}$ .

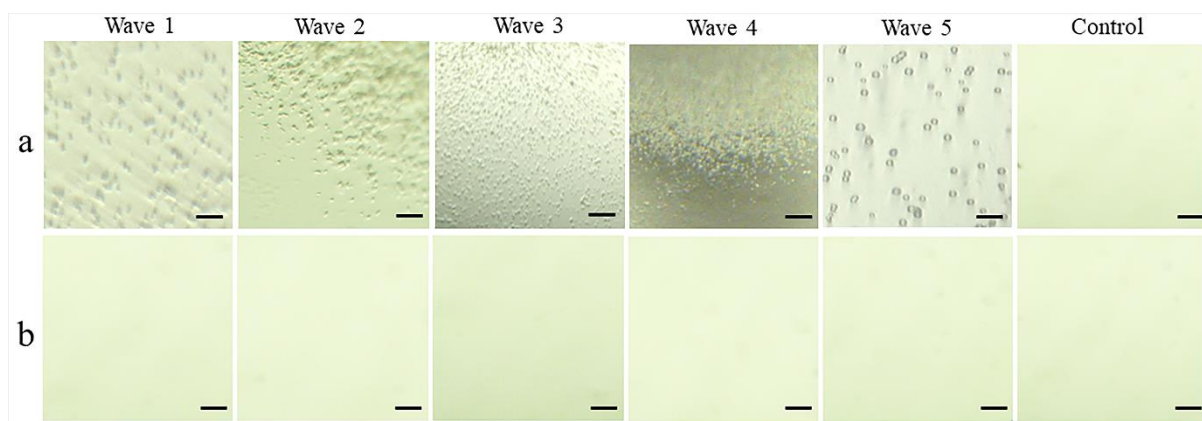


**Figure 4** LDCs of BPTI formed with (a) the Pt EF setup and (b) the PCG EF setup. No LLPS was observed after mixing BPTI with KSCN at 20°C when an EF was absent (control). Generally, the LDC formation of BPTI in the presence of  $\text{SCN}^-$  is reported to be temperature dependent,<sup>3</sup> therefore, the droplets in the control sample remained clear even after an incubation of 24 hours. However, LDCs appeared in the same condition after 1 hour of applying Pt wire EFs. Induction of BPTI phase separation did not appear when applying the EFs based on parallel conductive glass. All scale bars correspond to 50  $\mu\text{m}$ .

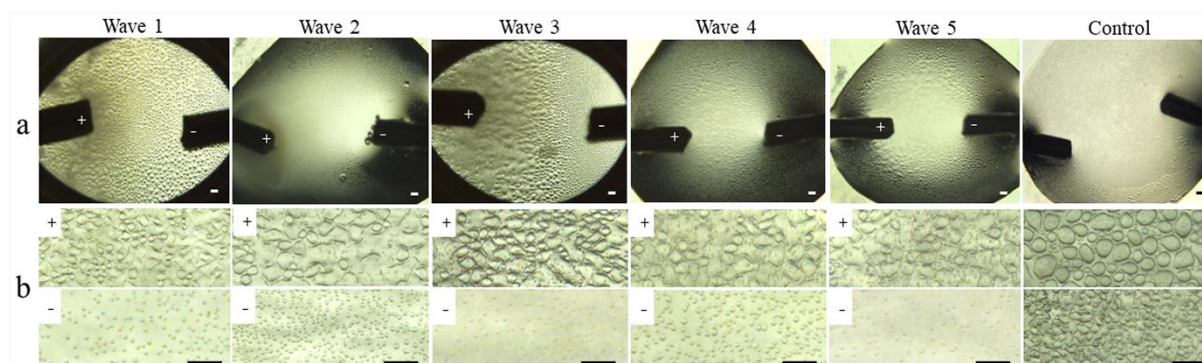




**Figure 5** LDCs of  $\beta$ -lactoglobulin formed with (a) the Pt EF setup and (b) the PCG EF setup. No apparent morphology differences between LDCs induced by different EF waveforms were observed. The dimensions of LDCs nearby the anode were larger than those formed nearby the cathode, due to the overall negative net charged  $\beta$ -lactoglobulin. The size and shape of LDCs nearby the cathode were uniform. The scale bars are all 200  $\mu\text{m}$ .

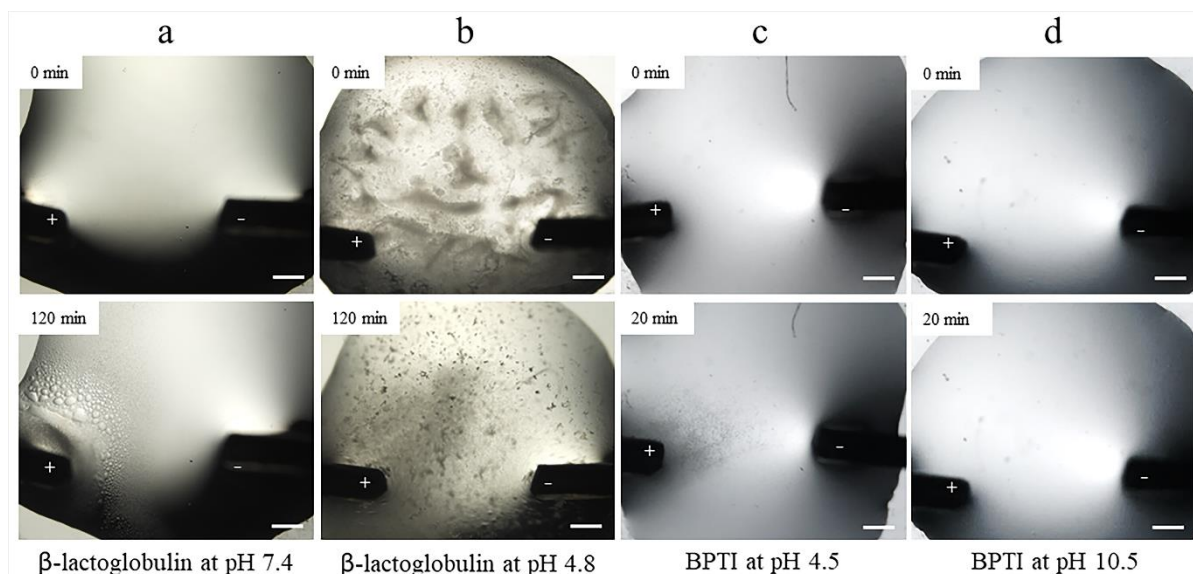


**Figure 6** Images show protein migration and phase separation of (a)  $\beta$ -lactoglobulin at pH 7.4, (b)  $\beta$ -lactoglobulin at pH 4.8, (c) BPTI at pH 4.5, and (d) BPTI at pH 10.5 in a Pt EF of waveform 3 ( $V_{\text{max-500}\Omega}=20\text{ V}$ ). Scale bars correspond all to 300  $\mu\text{m}$ . In images b and d,  $\beta$ -lactoglobulin ( $\text{pI}=4.76$ ) and BPTI ( $\text{pI}=10.5$ ) solutions were at their isoelectric point, respectively. Thereby, due to an overall net charge close to zero no protein migration was observed. Solutions of  $\beta$ -lactoglobulin and BPTI in images a and c were adjusted to a negative overall net charge and positive overall net charge, respectively, for which protein migration and LDCs were observed in the presence of EFs. More LDCs of positively charged BPTI appeared near the anode in image c. This unexpected result was also observed and explained by Hammadi et al. when investigating protein crystallization induced by a local electric potential.<sup>4</sup> It was elucidated that decamers and monomers coexist in an acidic BPTI solution and the decamers have lower speed of electrophoretic motion than the monomers, 0.32 and 0.36, respectively. Therefore, the BPTI decamer to monomer ratio increased towards the anode, which locally increased the supersaturation near the anode. Consequently, more BPTI LDCs formed in close proximity of the anode.<sup>5</sup> Time intervals indicated in the pictures are showing the application time of the EFs.

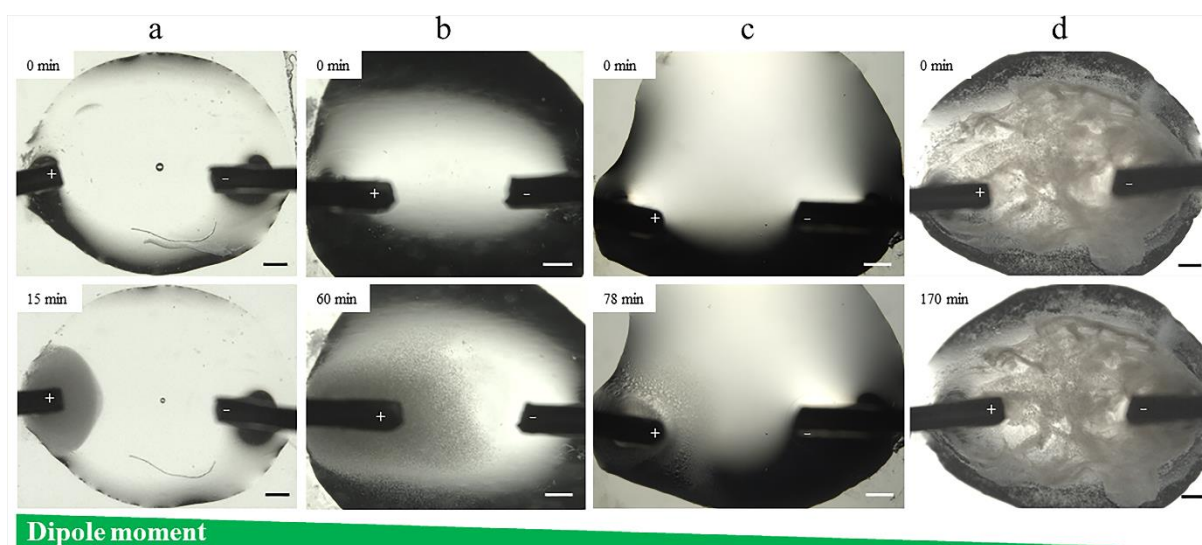


**Figure 7** Protein migration and phase separation of (a) GI (dipole moment = 1082 D), (b) BPTI (dipole moment = 941 D), (c)  $\beta$ -lactoglobulin (dipole moment = 594 D), and (d) hemoglobin (dipole moment = 201 D) under a Pt EF with waveform 3 ( $V_{\max-500\Omega}=20$  V). Scale bars correspond all to 300  $\mu\text{m}$ . Time intervals indicated in pictures are showing the application time of the EFs. The sample droplet conditions for each protein are summarized in SI Table 1. It can be concluded that the migration rate of proteins to either electrode sequentially increased with the increase of the characteristic dipole moment. GI, with the highest dipole moment among the four proteins, showed the highest migration rate. A dense phase within the GI solution surrounded the anode after 15 min of EF application. Hemoglobin clusters, with the lowest molecule dipole moment of 201 D, did not undergo any migration in the droplet, despite exposure to an EF for a rather long time of 170 min.

## References

- 1 C. E. Felder, J. Prilusky, I. Silman and J. L. Sussman, *Nucleic Acids Research*, 2007, **35**, 512–521.
- 2 R. Schubert, *Thesis*, 2016, 157.
- 3 S. Grouazel, J. Perez, J. P. Astier, F. Bonneté and S. Veessler, *Acta Crystallographica Section D: Biological Crystallography*, 2002, **58**, 1560–1563.
- 4 Z. Hammadi, J. P. Astier, R. Morin and S. Veessler, *Crystal Growth and Design*, 2007, **7**, 1472–1475.
- 5 C. Hamiaux, J. Pérez, T. Prangé, S. Veessler, M. Riès-Kautt and P. Vachette, *Journal of Molecular Biology*, 2000, **297**, 697–712.

## **8.6 Supplementary Information-Formation kinetics and physicochemical properties of mesoscopic $\alpha$ -synuclein (ASN) assemblies modulated by sodium chloride and a distinct pulsed electric field**

# Supporting Information for:

## Formation Kinetics and physicochemical Properties of mesoscopic Alpha-Synuclein Assemblies modulated by Sodium Chloride and a distinct pulsed electric Field

Mengying Wang,<sup>a</sup> Roland Thuenauer,<sup>b,c,d</sup> Robin Schubert,<sup>e</sup> Susanna Gevorgyan,<sup>a</sup> Kristina Lorenzen,<sup>e</sup> Hévila Brognaro,<sup>a</sup> Christian Betzel<sup>a,f</sup>

<sup>a</sup> University of Hamburg, Laboratory for Structural Biology of Infection and Inflammation, Institute of Biochemistry and Molecular Biology, Notkestrasse 85, c/o DESY, Building 22a, 22607 Hamburg, Germany.

<sup>b</sup> Technology Platform Light Microscopy, University of Hamburg, Mittelweg 177, 20148 Hamburg, Germany

<sup>c</sup> Center for Structural Systems Biology (CSSB), Notkestrasse 85, c/o DESY, Building 15, 22607 Hamburg, Germany

<sup>d</sup> Technology Platform Microscopy and Image Analysis (TP MIA), Leibniz Institute of Virology (LIV), Martinistrasse 52, 20251 Hamburg, Germany

<sup>e</sup> European XFEL GmbH, Holzkoppel 4, 22869 Schenefeld, Germany.

<sup>f</sup> Correspondence: christian.betzel@uni-hamburg.de

### Experimental materials and methods

#### Expression and purification of recombinant $\alpha$ -synuclein protein.

A single colony of *E. coli* BL21(DE3) was cultured in 100 mL LB medium (150 mg/L ampicillin) at 37 °C up to OD<sub>600</sub> between 0.7–1.5. Obtained cultures were induced by adding 1 mM IPTG and the following protein expression was performed up to 3 hours. Afterwards the cells were pelletized and resuspended in 0.75 mL of buffer (50 mM Tris pH 8.0, 10 mM EDTA, 150 mM NaCl). Resuspended cells were boiled for 10 min and then pelletized at 21130 x g for 5 min. The supernatant was transferred to a new tube and spined for 2 min after adding streptomycin sulfate (136  $\mu$ L of a 10% solution/mL of supernatant) and glacial acetic acid (228  $\mu$ L/mL of supernatant), followed by one step of precipitation with saturated ammonium sulfate at 4 °C.



Precipitated protein was again pelletized and one time washed with 1 mL of ammonium sulfate solution (1:1 (v/v) saturated ammonium sulfate (4 °C) and ddH<sub>2</sub>O). The washed pellet was resuspended in 900 µL of 100 mM ammonium acetate and precipitated by adding 900 µL of ethanol at 20 °C. This step was repeated twice and followed by a resuspension in 20 mM Tris pH 7.4, 250 mM NaCl and 1 mM DTT. The resuspended solution of ASN tagged with 6x histidine amino acids was incubated with TEV protease overnight at 4 °C to the His-tag hydrolysis and ASN was purified by Ni-NTA column. Finally, monomeric ASN was obtained by performing the size exclusion chromatography utilizing a HiLoad 16/60 Superdex 75 pg column (Sigma, Neustadt, Germany) equilibrated with 20 mM Tris buffer pH 7.4, 250 mM NaCl and 1 mM DTT. The purity and dispersed homogeneity of obtained protein material was analyzed by a 12% SDS-PAGE and DLS (**Supplementary Figure 1**), which demonstrated the molecular weight to be 18 kD<sup>1</sup> and showed a hydrodynamic radius of  $3.65 \pm 0.51$  nm (PDI: 15%) of monomeric ASN.

#### **Polarized and depolarized dynamic light scattering (DLS/DDLS).**

The in-house built DDLS instrument used for the experiments has been described previously.<sup>2</sup> Briefly, a laser beam with a wavelength of 532 nm and output power of 100 mW is polarized by a vertical polarizer before passing a sample solution. The vertical component and horizontal component of the scattered light were collected simultaneously by an objective (Plan APO ELWD 20 × 0.42 WD = 20) directly at 90° and by a polarizing beam splitter (Qioptic Photonics, Göttingen, Germany), respectively, to generate the DLS and DDLS signals. A transparent quartz cuvette (101.015-QS, Hellma Analytics, Munich, Germany) with inner dimensions of 3 mm × 3 mm × 21 mm was used and immersed into an index matching water bath (1 mm thickness). For applying the pulsed electric fields (EFs) during DLS/DDLS measurement, two platinum (Pt) wires with 0.3 mm diameter, 25 mm length and a resistance (R) of approx. 37.5 mΩ at 20 °C (Sigma, Neustadt, Germany) were inserted at two opposite corners of the cuvette. The up-and-down waveform of the applied pulsed EF was shown in previous publications,<sup>3,4</sup> having a pulse width of  $0.6 \pm 0.15$  ms with a maximum output pulse amplitude of 30 V and no more than 1 V of minimum amplitude on 500 Ω load.

For DLS/DDLS measurements a 40 µL ASN solution was pipetted into the cuvette and sealed with a cover slide. Each data point was collected with an acquisition time of 20 s, followed by a delay time of 20 s. The

hydrodynamic radii ( $R_h$ ) of the proteins were calculated based on the Stokes-Einstein equation (equation 1)<sup>5</sup> and Stokes-Einstein-Debye equation (equation 2)<sup>6</sup>:

$$D_t = \frac{K_B T}{6\pi\eta R_h} \quad (1)$$

$$D_r = \frac{K_B T}{8\pi\eta R_h^3} \quad (2)$$

where  $D_t$  and  $D_r$  represent the translational and rotational diffusion coefficients, respectively, obtained from the corresponding autocorrelation function applying the CONTIN algorithm.<sup>7</sup>  $K_B$  is the Boltzmann coefficient;  $T$  is the absolute temperature and  $\eta$  is the viscosity value of the solution.

An appropriate viscosity value of each sample solution was considered for the  $R_h$  calculations. ASN solutions were prepared in 20 mM Tris buffer pH 7.4 and a gradient of NaCl (0, 50, 150, 250 mM). To monitor the radii and structural evolution of ASN clusters 15% PEG8000 was introduced into 50  $\mu$ M ASN solutions. All sample conditions were used for experiments without and with exposing sample solutions with EFs for 2 hours.

### **Imaging via optical brightfield microscope and transmission electron microscopy (TEM).**

The phase diagram of ASN was investigated at 20 °C in a protein concentration range of 5-500  $\mu$ M, applying PEG8000 as crowding agent from 0 up to 20% (w/v) 20 mM Tris buffer pH 7.4, 150 mM NaCl. Images of droplets were recorded applying a cold-light source Leica M205C microscope after 1, 24, 48, and 72 hours.

For TEM imaging the same sample conditions were applied as for the DDLS experiment. After 3 days incubation at 20 °C, a 4  $\mu$ L of ASN solution was pipetted onto a quantifoil holey carbon coated copper grid (quantifoil 1.2/1.3, 400 mesh, Science Services, Germany), which was glow-discharged for 30 s at 25 mV (GloQube Plus, Quorum) before using. Samples were blotted with a Whatman paper after 30 s incubation, following by two times of grid washing with 10  $\mu$ L ultrapure water. Afterwards, the grid was placed on the droplet of 10  $\mu$ L of 2% (w/v) uranyl acetate for negative staining. After 30 s, the grid was removed from the uranyl acetate droplet, blotted and dried on the Whatman paper. TEM images were recorded using a JEM 2100-Plus with 200 kV acceleration voltage.<sup>8</sup>

### **Congo red staining and Thioflavin T (ThT) fluorescence assays.**

0.1% (w/v) Congo red solution and 1 mM Thioflavin T (ThT) solution were prepared in 20 mM Tris buffer pH 7.4 and filtered through a 0.2  $\mu$ m filter (SARSTEDT, Germany). For Congo red staining, 0.3  $\mu$ L of 0.1%

(w/v) Congo red solutions were added to 3  $\mu\text{L}$  of ASN droplets. After 5-minute incubation at 20  $^{\circ}\text{C}$ , the droplets were observed applying a Leica M205C microscope.

For ThT assays 1  $\mu\text{L}$  of ThT solution was added to 50  $\mu\text{L}$  ASN sample using a Corning 384 flat bottom black polystyrene plate (Sigma, Neustadt, Germany). The fluorescence intensity was recorded from the top at 20 $^{\circ}\text{C}$  using a TECAN plate reader (Infinite 200 PRO, Tecan Trading AG, Switzerland) at an excitation wavelength of 440 nm and recording an emission wavelength of 480 nm. Assays were performed in triplicates.

### **Determining the diffusion interaction parameter ( $K_D$ ) and analyzing the thermostability of $\alpha$ -synuclein via DLS.**

A Wyatt Mobius instrument (Wyatt Technology, Santa Barbara, CA, USA) with a sample temperature controller (4-70  $^{\circ}\text{C}$ ) and laser wavelength of 532 nm was used to analyze the thermostability and determine  $K_D$  of ASN. The translational diffusion coefficient  $D_t$  determined by DLS is a function of concentration  $c$  <sup>9</sup>:

$$D_t = D_0(1 + K_D c) \quad (3)$$

where  $D_0$  is the diffusion coefficient at infinite dilution, and  $c$  is the concentration of the protein in mg/mL,  $K_D$  is the first-order diffusion interaction parameter.

For the determination of ASN  $K_D$  values in different NaCl solutions, six concentrations of ASN ranging from 1 to 11 mg/mL were applied. Each sample, centrifuged for 1 hour at 21130 x g and 4  $^{\circ}\text{C}$  prior to DLS measurements, triplicates with a recording time of 5 s and an interval time of 1 s were measured. The corresponding  $K_D$  value of ASN under each NaCl condition was calculated and analyzed applying the software DYNAMICS, applying equation 3.

For the thermostability measurements, the  $R_h$  of monomeric ASN at 100  $\mu\text{M}$  in 20 mM Tris buffer pH 7.4 and at different NaCl concentrations (0, 50, 150, and 250 mM) was measured firstly applying a ramp-up temperature (20  $^{\circ}\text{C}$  up to 70  $^{\circ}\text{C}$ ) followed by a ramp-down temperature gradient (70  $^{\circ}\text{C}$  to 20  $^{\circ}\text{C}$ ).  $R_h$  values of ASN assemblies induced by 15% PEG8000 in the presence and absence of EFs in solutions with 20 mM Tris buffer pH 7.4 and a series of NaCl (0, 50, 150, and 250 mM) were measured with identical temperature gradients, increasing up to 70  $^{\circ}\text{C}$  firstly and then cooling down to 20  $^{\circ}\text{C}$ , in a ramp speed of 1  $^{\circ}\text{C}/\text{min}$ . The DLS

data were recorded with a temperature step of 1 °C and each data point generated is the average of triplicate acquisitions applying an acquisition time of 5 s in intervals of 1 s.

Wyatt DYNAMICS uses two types of fits for autocorrelation functions, cumulants and regularization fits. The cumulants fit assumes one population of particles with a single average diffusion coefficient and a single standard deviation about the average, while the regularizations fit assumes the presence of any number of populations of particles and each with its own polydispersity. Following the DYNAMICS user guide, the cumulant radii derived from the cumulants fit were used to calculate the  $K_D$  values and were used for the temperature-dependence analysis.<sup>10</sup>

### **Characterizing the autofluorescence of assembled $\alpha$ -synuclein applying confocal laser scanning microscopy (CLSM).**

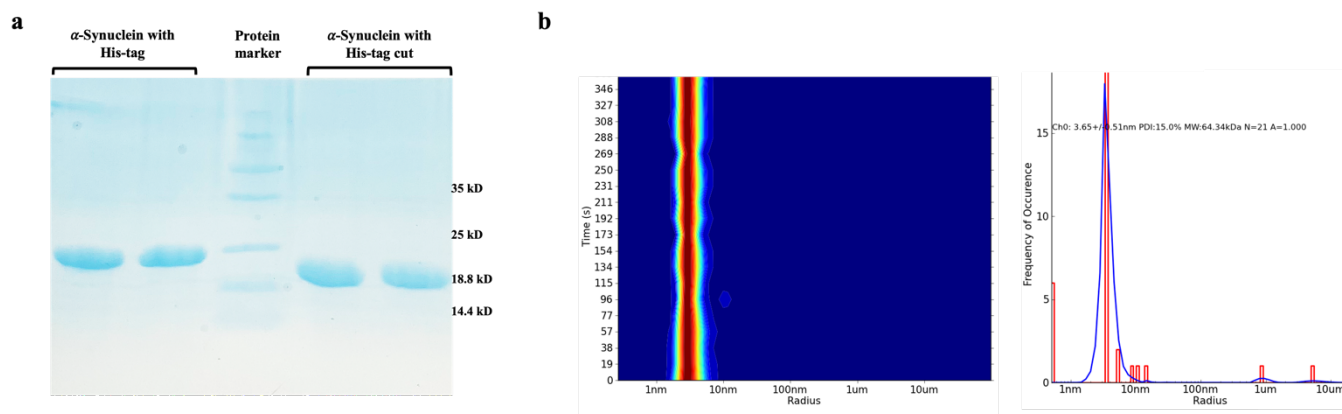
A confocal laser scanning microscope (SP8, Leica) equipped with a 405 nm laser excitation source, spectral detector, and a 63x oil immersion objective with a numerical aperture (N.A.) of 1.4 was used for imaging and fluorescence detection. 150  $\mu$ L of samples were loaded into the wells of an 8-well chambered coverslip with 300  $\mu$ L/well capacity and a glass bottom of 170  $\mu$ m  $\pm$  5  $\mu$ m thickness ( $\mu$ -Slide 8 Well<sup>high</sup> Glass Bottom, Ibidi GmbH, Gräfelfing, Germany). To measure fluorescence spectra an excitation at 405 nm was used and the fluorescence intensities were detected in the wavelength range of 420-780 nm with a detection bandwidth of 20 nm and a step size of 3 nm. The fluorescence spectra of manually chosen background regions were subtracted from the spectra of ASN assemblies. Data analysis was performed applying GraphPad Prism software (Version 9.2.0, San Diego, US) and the normalized spectra were plotted and fitted with a polynomial function of six orders.

### **Measuring the secondary structure of monomeric $\alpha$ -synuclein applying circular dichroism.**

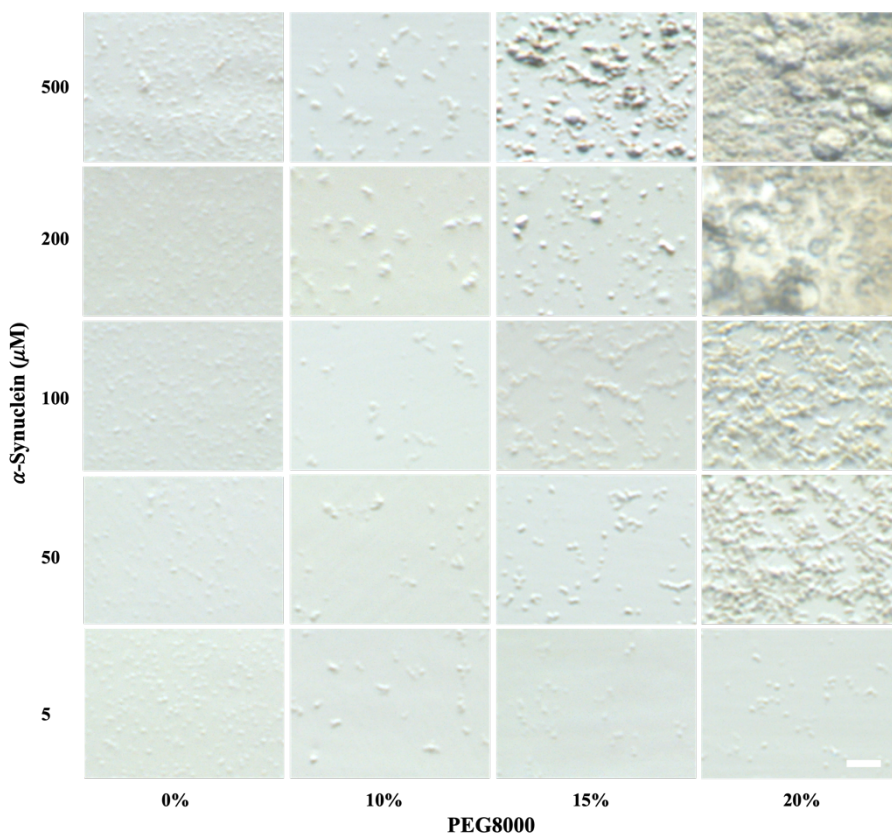
ASN at 1 mg/mL in 20 mM Tris buffer pH 7.4 was prepared with four different concentrations of NaF (0, 50, 150, 250 mM) and centrifuged at 16000 x g, 4 °C for 1 h. For investigating the effect of EFs on the secondary structure of ASN, a 50  $\mu$ L ASN solution was exposed to EFs for 1 hour, followed by 5-minutes centrifugation at 21130 x g and 20 °C to remove aggregates. All samples not exposed or exposed to EFs were diluted by the corresponding buffer to a final concentration of 0.2 mg/mL ASN. Finally, all diluted samples were transferred to a quartz cuvette with 1 mm path length (Hellma- Analytics, Germany) and were measured applying a

JASCO-815 spectropolarimeter (JASCO, Japan). In each measurement 10 individual spectra were averaged, recorded within a wavelength range of 260-190 nm, with a scanning speed of 100 nm/min and a bandwidth of 1 nm. The spectra were evaluated by the Software Spectra Manager from JASCO.

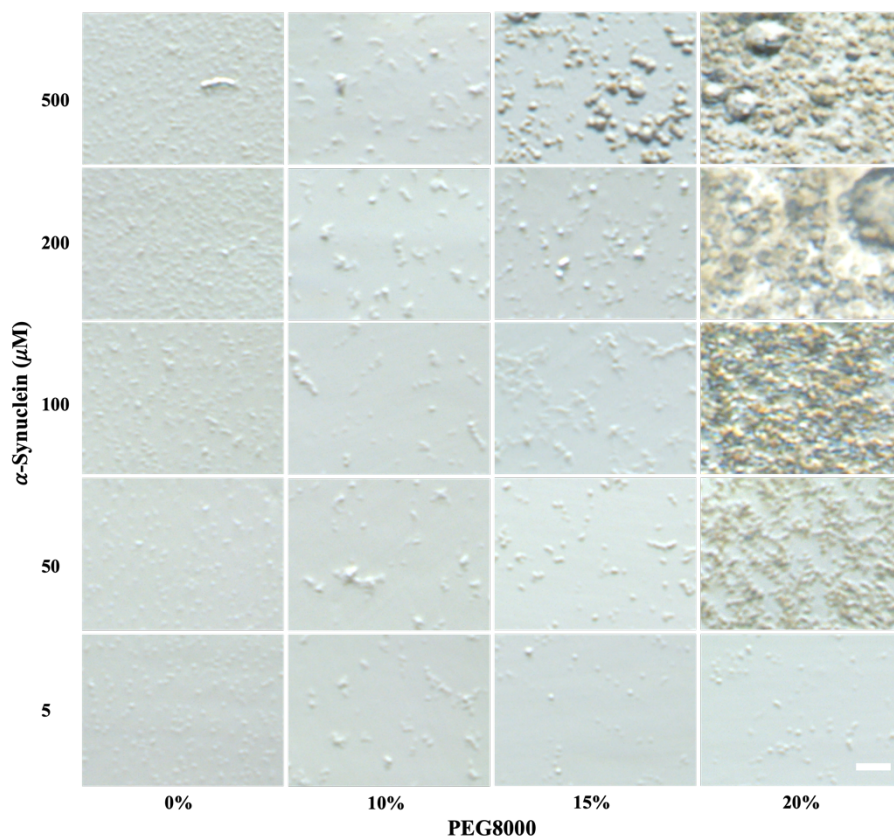
## Supplementary figures



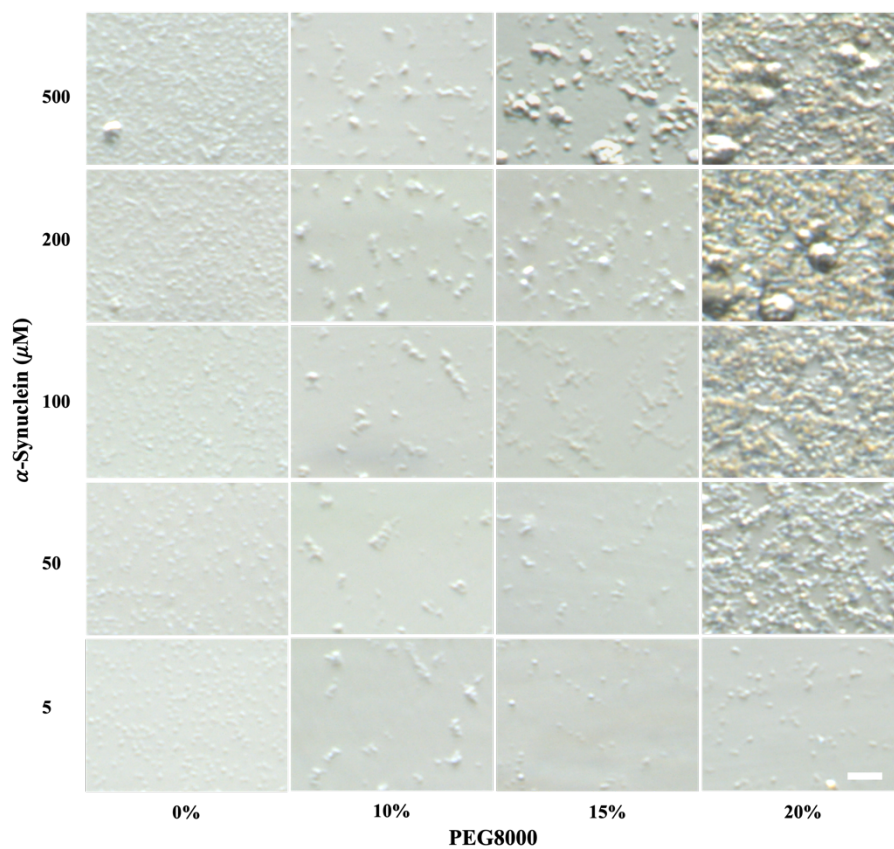
Supplementary Figure 1. Quality control of purified  $\alpha$ -synuclein applying (a) 12% SDS-PAGE and (b) DLS.



Supplementary Figure 2. Phase diagram of  $\alpha$ -synuclein obtained after 24-hour incubation at 20 °C in solutions of 20 mM Tris pH 7.4, 150 mM NaCl, and PEG8000. The scale bar corresponds to 10  $\mu$ m.

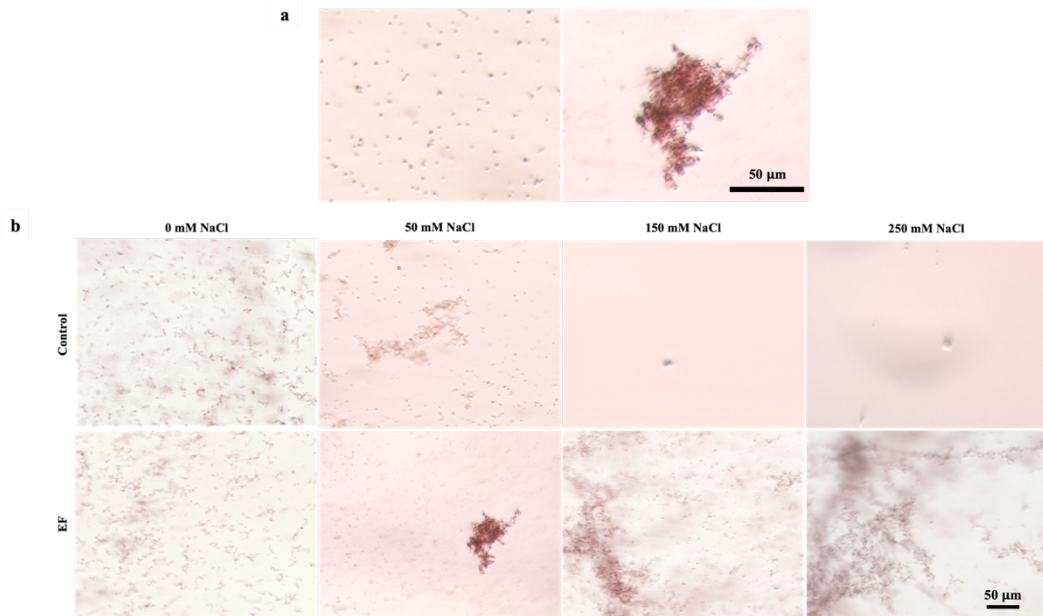


Supplementary Figure 3. Phase diagram of  $\alpha$ -synuclein observed after 48-hour incubation at 20 °C in solutions of 20 mM Tris pH 7.4, 150 mM NaCl, and PEG8000. The scale bar corresponds to 10  $\mu\text{m}$ .

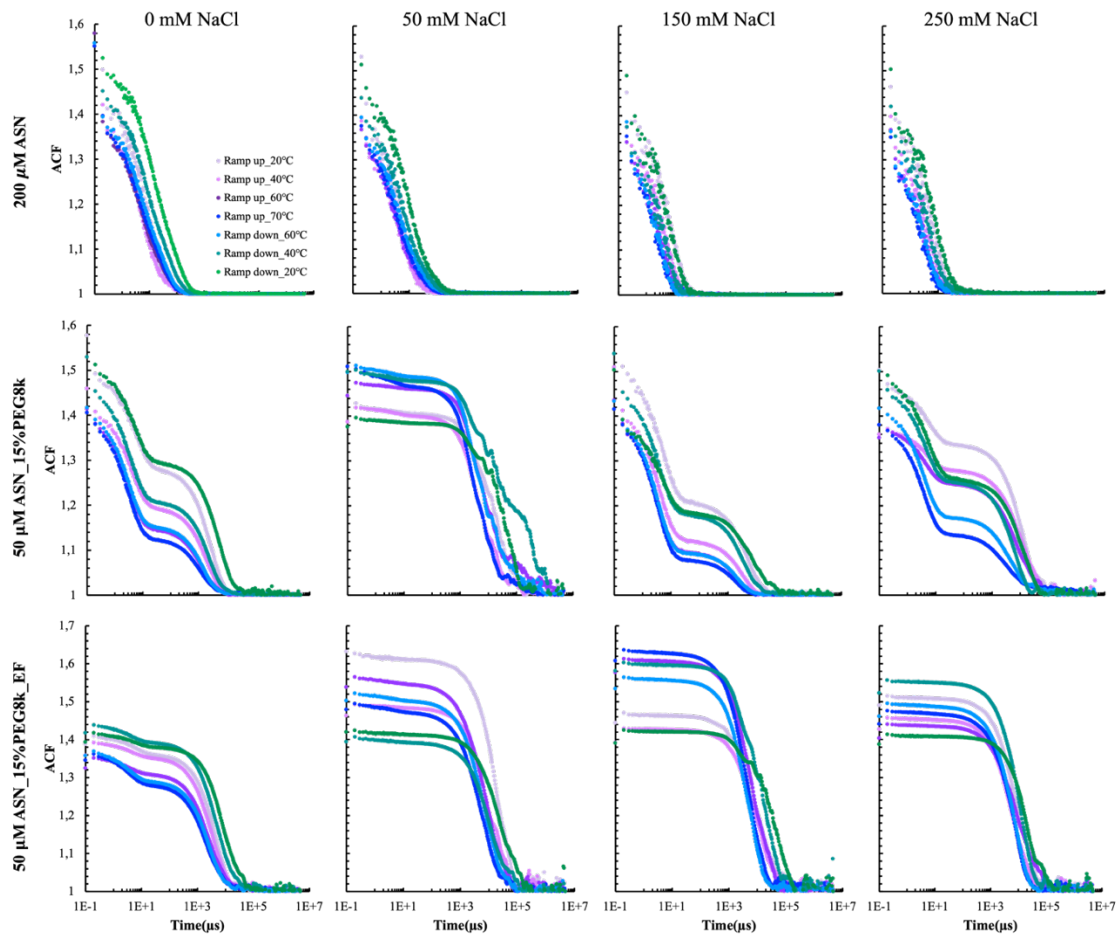


Supplementary Figure 4. Phase diagram of  $\alpha$ -synuclein collected after a 72-hour incubation at 20 °C in solutions of 20 mM Tris pH 7.4, 150 mM NaCl, and PEG8000. The scale bar corresponds to 10  $\mu\text{m}$ .



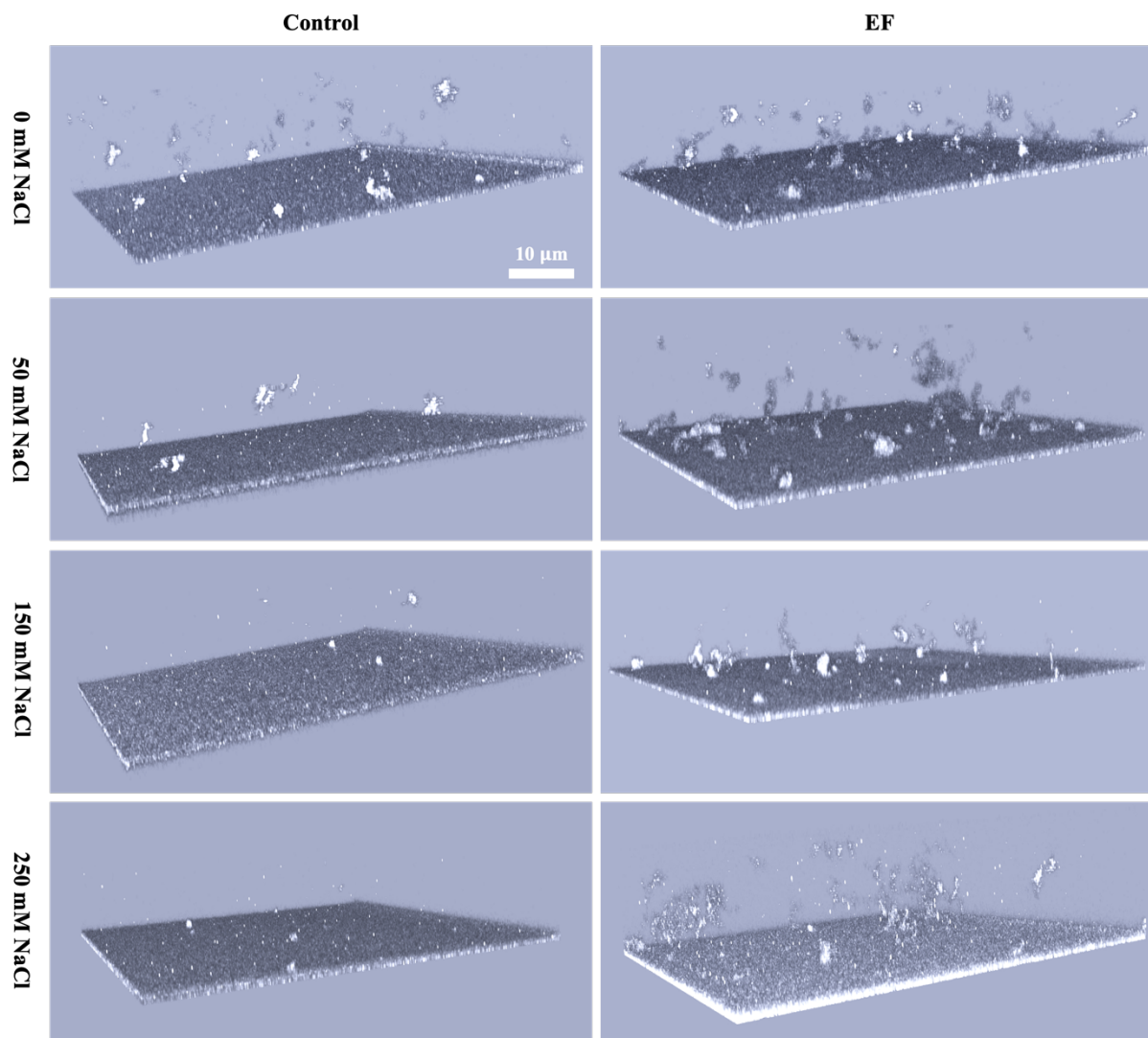


Supplementary Figure 5. (a) Examples of monodispersed and stacked globular assemblies of ASN stained by 0.01% (w/v) Congo red. (b) The Congo red staining results for ASN assemblies formed after 3 days in solutions of 50  $\mu\text{M}$  ASN, 15% PEG8000, and a NaCl gradient without (control) or with the application of a pulsed electric field (EF) at 20  $^{\circ}\text{C}$ .



Supplementary Figure 6. Regularization autocorrelation function (ACF) curves of DLS measurements for  $\alpha$ -synuclein with the increase (20  $^{\circ}\text{C}$   $\rightarrow$  70  $^{\circ}\text{C}$ ) and decrease (70  $^{\circ}\text{C}$   $\rightarrow$  20  $^{\circ}\text{C}$ ) of the temperature in different solutions.





Supplementary Figure 7. Representative three-dimensional images of  $\alpha$ -synuclein solutions scanned in-situ by confocal laser scanning microscopy (CLSM), after 2-hour incubation at 20 °C without (control) or with the treatment of a pulsed EF.

## References

- 1 M. A. Saraiva, *Int. J. Biol. Macromol.*, 2021, **177**, 392–400.
- 2 R. Schubert, A. Meyer, K. Dierks, S. Kapis, R. Reimer, H. Einspahr, M. Perbandt and C. Betzel, *J. Appl. Crystallogr.*, 2015, **48**, 1476–1484.
- 3 M. Wang, S. Falke, R. Schubert, K. Lorenzen, Q. Di Cheng, C. Exner, H. Brognaro, C. N. Mudogo and C. Betzel, *Soft Matter*, 2020, **16**, 8547–8553.
- 4 M. Wang, A. L. C. Barra, H. Brognaro and C. Betzel, *Crystals*, 2022, **12**, 437.

- 5 A. Einstein, *Ann. der Phys.*, 1905, **17**, 549.
- 6 P. Debye, *Polar Molecules*, 1929.
- 7 S. W. Provencher, *Comput. Phys. Commun.*, 1982, **27**, 213–227.
- 8 H. Han, E. Round, R. Schubert, Y. Gul, J. Makroczyova, D. Meza, P. Heuser, M. Aepfelbacher, I. Barak, C. Betzel, P. Fromme, I. Kursula, P. Nissen, E. Tereschenko, J. Schulz, C. Uetrecht, J. U. M. Wilmanns, J. Hajdu, V. S. Lamzi and K. Lorenzen, *J. Appl. Crystallogr.*, 2021, **54**, 7–21.
- 9 S. Kenrick and D. Some, *Appl. Note Wyatt Technol. Corp.*, 2014, 1–6.
- 10 Wyatt Technology Corporation, *Tech. Note TN2005*, 2017, **1**, 1–8.



## 9 Acknowledgement

First of all, I would like to thank my PhD supervisor, Professor Christian Betzel, providing me this valuable opportunity and advanced platform to study and research the interesting project of protein phase separation. He is the one open me a new door to science and world. As my supervisor, he did his best encouraging me to join international conferences, workshops, and trainings to open my mind and improve my scientific skills. I am grateful that he provided me the necessary guidance for science and freedom to explore and carry on my project. I am also grateful that he offered me financial support to make me able to focus on my study and research work. For this important opportunity changing my life, I must appreciate that Professor Dachuan Yin, my master supervisor, led me to the front of this door. He always helped me getting through the tough time and gave me the necessary assistance to go on.

Without the love and support of my family, I would not be able to focus on my study and work in Hamburg. I am thankful that they always try to understand and respect my every decision. Especially, I want to thank my boyfriend Chuang Wang, who has been understanding me and giving me courage to face problems and break through myself. I also would like to thank Dr. Qingdi Cheng who helped me adapt soon to the study and life in Germany, my friends Dr. Jiexi Zhang, Huan Zhao, and Xinyue Wang who made my life easy and happy in Hamburg.

On the way of science, I would like to show my respect and appreciations to dear Dr. Hévila Brognaro who made me learn to be rigorous, patient, and tenacious to the hard scientific problems; to my lovely colleague & friend Susanna Gevorgyan who is smart and always kind and responsible to everyone and our team; to dear Angélica Barra who inspired and thrived my work of protein nucleation; to Bruno Alves Franca who always recommended me useful techniques to improve my research; to Dr. Najeeb Ullah who is always nice and taught me how to process SAXS data; to Dr. Hina Andaleeb who gave me a warm company during the difficult PhD study; to Dr. Robin Schubert who supported me a lot for TEM imaging; to Dr. Vasundara Srinivasan who helped me fishing crystals and gave me suggestions; to Dr. Prince Prabhu who always communicated scientific ideas with me; to Martin Schwinzer who supported me with CD measurement; to Max Sommer who is always willing to offer a hand to me; to Sven Falke and other colleagues who helped me to overcome problems during this project. This work would not be done without all of your help.



## 10 Declaration on oath

*„I hereby declare on oath, that I have written the present dissertation by my own and have not used other than the acknowledged resources and aids. The submitted written version corresponds to the version on the electronic storage medium. I hereby declare that I have not previously applied or pursued for a doctorate (Ph.D. studies). “*

22.02.2023 

**Date, signature**

